2018

Analysis of the Shock Response Spectrum and Resonant Plate Testing Methods

William Larsen
Michigan Technological University, wslarsen@mtu.edu

ANALYSIS OF THE SHOCK RESPONSE SPECTRUM AND RESONANT PLATE TESTING METHODS

By

William S. Larsen

A THESIS

Submitted in partial fulfillment of the requirements for the degree of

MASTER OF SCIENCE

In Mechanical Engineering

MICHIGAN TECHNOLOGICAL UNIVERSITY

2018

This thesis has been approved in partial fulfillment of the requirements for the Degree of MASTER OF SCIENCE in Mechanical Engineering.

Department of Mechanical Engineering-Engineering Mechanics

Thesis Advisor:	*Jason R. Blough*
Committee Member:	*James P. DeClerck*
Committee Member:	*Charles D. Van Karsen*
Department Chair:	*William Predebon*

Table of Contents

List of figures

List of tables

Preface

This research was conducted at Michigan Technological University. This project was a continuation of a senior design project from 2016. Many of the methods and results presented were included in conference papers presented at 2017 SAVE in Jacksonville, FL and 2018 IMAC in Orlando, FL. [1] [2] [3] This work was funded by Honeywell Federal Manufacturing & Technologies under Contract No. DE-NA0002839 with the U.S. Department of Energy.

Acknowledgements

I would like to thank David Soine and Richard Jones at Honeywell Federal Manufacturing and Technologies for providing the opportunity and means for this research. I would also like to thank my advisor Dr. Jason Blough for his guidance and support, as well as professor Charles Van Karsen and Dr. James DeClerck, all for their endless insight. I would like to thank Dr. William Shapton for encouraging me to take on this challenge. I of course could not have done any of this without the unwavering support of my family and my fiancée Rebecca.

Abstract

Intricacies of the shock response spectrum were discovered and investigated by testing a circular plate structure with integral damping. Effects on the SRS from physical alterations to the nonlinear structure were monitored from low and high shock impulses. A method was developed and validated to estimate high amplitude shock inputs from low amplitude frequency response functions. Finite element models explored variable thickness plate designs.

1 Introduction

Designing for mechanical shock is difficult, but the intricacies of testing for it can be even harder. Shock testing is utilized in (but certainly not limited to) spacecraft and avionics engineering, earthquake engineering, transportation and shipping and the computer industry. [4] There are a multitude of ways of accomplishing this goal from drop towers and shakers to Split Hopkinson Bars. [5] The area of focus of this research was on resonant plate testing.

1.1 Background

Resonant plate testing is a method currently accepted and commonly used for shock testing. A plate is designed that produces a particular desired frequency response. A test component is mounted (usually with a fixture) in the center on one side of the plate. The plate is impacted in the center on the opposite side. A type of damping material can be placed on the impact location to control the impulse duration and amplitude. A simple overview of a test setup can be found in Figure 1.

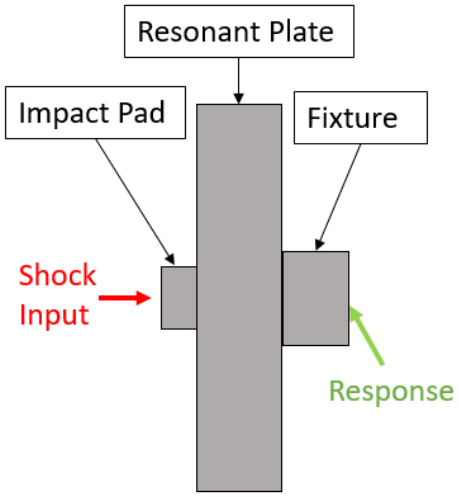

Figure 1. Overview of Resonant Plate Testing

Damping material can also be placed within the structure to create a constrained layer damping effect to increase the overall damping of the structure itself. A diagram of the inclusion of this damping material can be found in Figure 2.

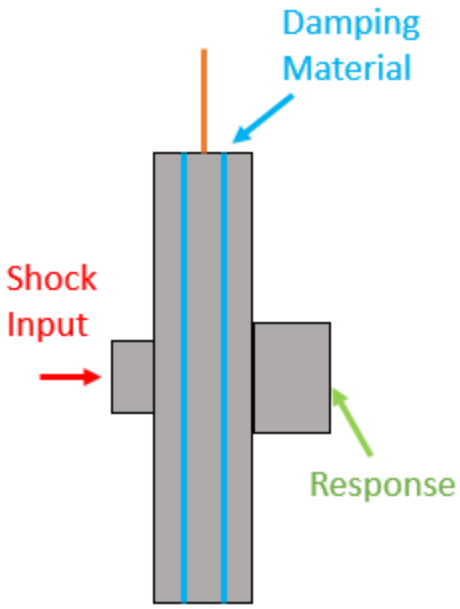

Figure 2. Diagram of Resonant Plate Testing with Integral Damping

A uniaxial accelerometer is typically placed on the test component to measure the acceleration on one axis that is in line with the impact direction. A shock response spectrum is calculated from that time trace. This is assumed to capture the response that the test component would be exposed to in a shock environment. The shock response spectrum (SRS) is a metric that is typically used to quantify the severity of this impulse. This calculation uses a peak hold type measurement to quantify how the test component would respond if the component was a single degree of freedom at each natural frequency. This results in a base excitation at each natural frequency, as shown in Figure 3.

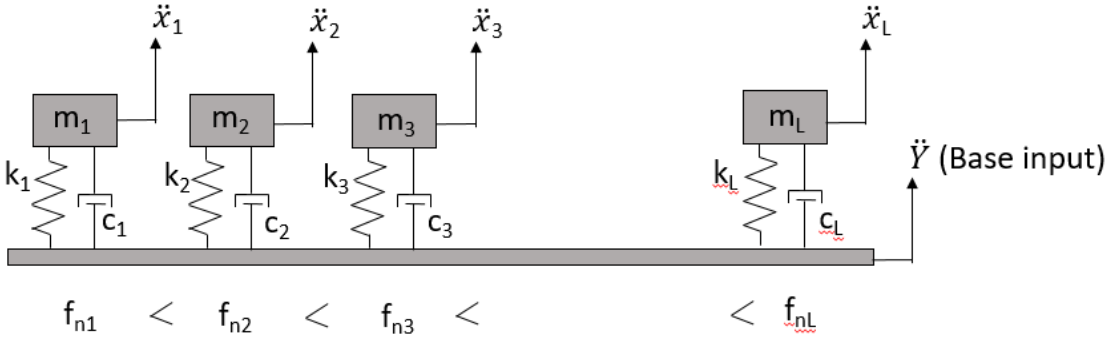

Figure 3. SRS Calculation Concept

The SRS shape is selected by measuring an experimental response and calculating a SRS. This SRS (with designated allowable margins for error) then becomes the standard test specification.

Rectangular plates have historically been used for resonant plate testing, but because there are many frequencies that contribute to the response, the plates cannot always be designed to produce desired shock response curves. [5] Previous analytical research has shown that the symmetry of circular plates can limit the number of contributing modes in the structure. [6] Resonant plate testing is considered a mid-field pyroshock test method as this mechanical test method typically produces responses that are between 1,000 and 10,000 g (acceleration due to gravity) in peak acceleration. [7] The test method is ideal for meeting specifications because it can produce a double sided pulse. [7]

1.2 Goals

The goals of this research were to analyze the SRS by modelling and performing experimental testing to gain a better understanding of how physical changes in the test relate to changes in the SRS. Using this knowledge, a structure could be designed to meet specific SRS test criteria. This was a very loosely structured goal with little to no clearly defined metrics to quantify success. A linear finite element model that could track alterations in design was created to guide the resonant plate design. Analytical simulations were used to gain insight into the variables and issues associated with testing. Experimental testing was conducted and analyzed to fine tune the understanding of the SRS. It is expected that any successful shock testing program will use these tools and procedures to achieve the desired results in an efficient manner.

2 Methods

2.1 Modelling

A FEA model and a numerical model were created and used to assist in the design and analysis of a resonant plate system. The basic geometric shape of the FEA model was validated with an analytical equation.

2.1.1 FEA Model

Previous research has investigated and proven that circular plates provide symmetry to minimize the number of contributing modes when impacted directly at the center. [6] A finite element model of an aluminum plate with a thickness of 1.125 inches and 17 inch diameter was created in Hypermesh to simulate this hypothesis. First order 0.2 inch tetrahedral elements were used. The boundary conditions of the plate were modeled as free-free, attached by four soft (1000 N/m) springs to ground at locations around the edge of the plate. An eigenvalue solution was used to solve for all modes of the plate up to 10,000 Hz. The modes with anti-nodes at the center of the plate are shown in Figure 4.

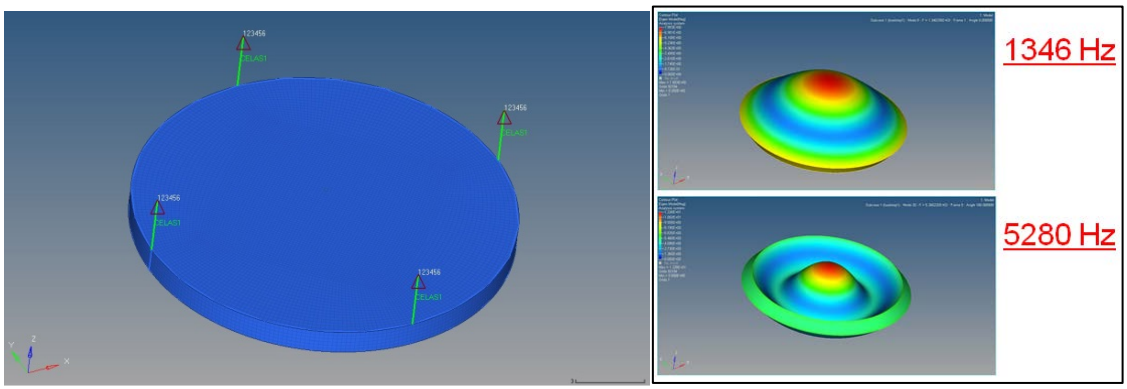

Figure 4. Hypermesh Model of Plate (Left) and Contributing Mode Shapes (Right)

To prove the validity of the model, all the modes were compared with analytical solutions. The following Equation 1 is the analytical representation of free-free circular plates. [8] The variables are described below in Equation 1.

$$f_{ij} = \frac{\lambda_{ij}^2}{2\pi a^2}\sqrt{\frac{Eh^2}{12\rho(1-\nu^2)}} \quad (1)$$

f = natural frequency
λ = natural frequency parameter
a = radius
E = modulus of elasticity
H = thickness
ρ = density
ν = Poisson's ratio

The values of λ_{ij} were analytically developed by Itao. [9] Table 1 includes the values of λ_{ij}^2 used in the calculation where i represents the number of nodal diameters and j represents the number of nodal circles. [8]

Table 1. Values of λ_{ij}^2 for Equation 1

		i (Nodal Diameters)				
		0	1	2	3	4
j (Nodal circles)	0	0	0	5.262	12.24	21.6
	1	9.063	20.51	35.24	52.92	
	2	38.51	59.86	84.37	111.2	
	3	87.81	119	153.3	190.7	

All other variables and selected values of parameters of the plate can be found in Table 2. The material properties are of 6061 aluminum.

Table 2. Structure Parameters for Equation 1

Name	Variable	Value	Units
Radius	a	8.5	in
Elastic Modulus	E	$1*(10)^7$	psi
Thickness	h	1.125	in
Density	ρ	0.000254	$(lb*s^2)/in^4$
Poisson's Ratio	ν	0.33	-

Using the values from Table 1 and Table 2 in Equation 1, the analytical natural frequencies of the plate can be calculated and are displayed in Table 3. The only contributing natural frequencies occur when there are zero nodal diameters (i=0). Only the 10 to 10,000 Hz frequency range is of interest.

Table 3. Natural Frequencies (Hz) of Free-Free Circular Plate from Equation 1

		i (Nodal Diameters)				
		0	1	2	3	4
j (Nodal circles)	0	0.0	0.0	791.3	1840.5	3248.0
	1	1362.8	3084.1	5299.1	7957.6	
	2	5790.8	9001.2	12686.8	16721.3	
	3	13204.1	17894.1	23051.9	28675.8	

A comparison of the finite element results and analytical results in Table 4 show errors below 10% for all critical natural frequencies of interest. The first six modes are rigid body modes of the plate.

Table 4. Simulated and Analytical Natural Frequencies of Free-Free Circular Plate

Mode Shape Natural Frequencies (Hz)					
Mode #	Nodal Diameters	Nodal Circles	Simulation	Analytical	Error (%)
7	2	0	789	791.3	-0.29
8	2	0	790	791.3	-0.16
9	0	1	1346	1362.8	-1.23
10	3	0	1793	1840.5	-2.58
11	3	0	1793	1840.5	-2.58
12	1	1	2938	3084.1	-4.74
13	1	1	2938	3084.1	-4.74
14	4	0	3065	3248.0	-5.63
15	4	0	3066	3248.0	-5.60
18	2	1	4846	5299.1	-8.55
19	2	1	4848	5299.1	-8.51
20	0	2	5282	5790.8	-8.79
27	3	1	6971	7957.6	-12.40
28	3	1	6972	7957.6	-12.39
29	1	2	7819	9001.2	-13.13
30	1	2	7821	9001.2	-13.11

After this initial check to aid in the design of the plate, the model was further expanded to include a fixture and impact pad that would more accurately simulate a typical experimental test.

2.1.2 Numerical Model

An analytical model of a constrained system was developed in MATLAB. The single degree of freedom model was selected to have a natural frequency of 1300 Hz and a mass of 14 kg for the physical parameters, which are both similar to the properties of the physical system. The stiffness to ground is dictated by the mass and selected natural frequency of

the mode, so in this system the stiffness is $9.34(10)^8$ N/m. A sample frequency of 100,000 Hz was used with a block size of 10,000 Hz to create a time history of the response. A haversine, which is the square of a sine wave, was selected as the excitation impulse shape. This is the general shape of an experimental impact impulse. The time duration of the pulse and damping were varied to monitor the effects on the SRS.

2.2 Testing

Structures were fabricated and experimental testing was performed to investigate the SRS by altering variables. An input estimation method was developed, validated, and performed on the experimental data and a modal analysis was executed.

2.2.1 Input Levels

To test this design, two different plate configurations were manufactured. Three 3/8 inch thick, 17 inch diameter plates were bolted together using 8 bolts in an equally spaced 11.5 inch diameter circular pattern. This system was designed to have a first bending mode frequency near 1300 Hz. A 5 inch square, 3 inch thick mock fixture was bolted through all of the 6061 T6 aluminum plates. This block of aluminum is intended to represent a test fixture and part. Two bolts at the top of the plates provided a mounting location to suspend the system.

One of the plate configurations had 0.125 inch of C2003 EAR damping material adhered between the plates (referred to as damped). The other set of plates had no damping material (referred to as undamped). The damped plate configuration can be seen in Figure 5.

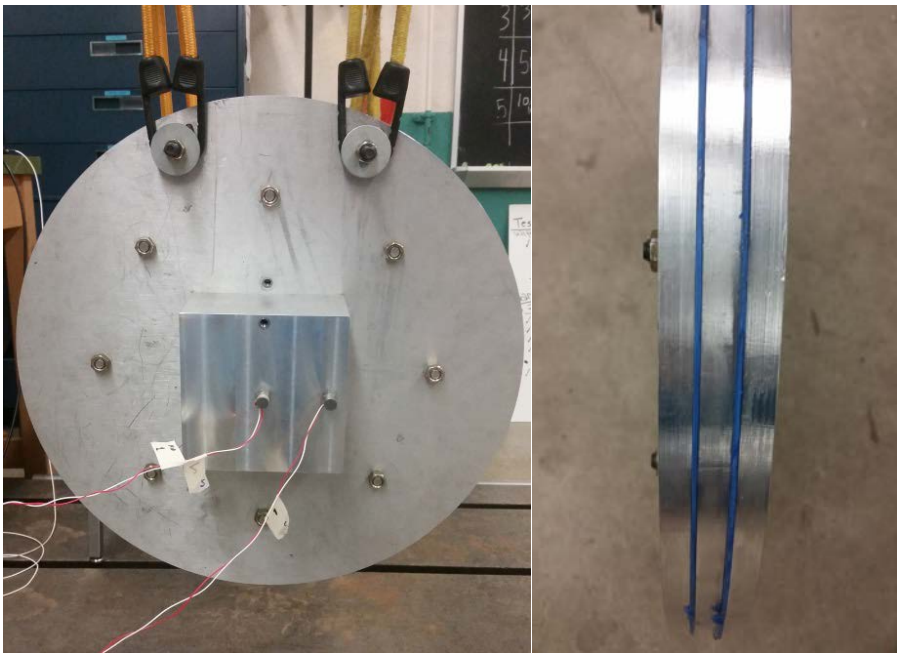

Figure 5. Resonant Plate with Fixture (Left), Damped Plate Cross Section (Right)

Low amplitude testing was performed using a PCB 086D20 handsledge impact hammer. This impact hammer has a resonant frequency greater than 12kHz and can measure up to 5000 lbf peak. The shock response at the fixture location was acquired using a PCB 350D02 shock accelerometer, which is +/- 1 dB from 4 Hz to 10,000 Hz and has a measurement range up to 50,000 g peak. Although the resonant frequency of this accelerometer is at least 100,000 Hz, there is an electrical filter applied at 17,000 Hz and a mechanical filter applied at 35,000 Hz. The response can be controlled by the plate geometry and material, impact projectile mass, impact projectile speed, impact duration, impact location, test item location, and clamps or suspension mechanisms. [7] The tested variables of interest for low amplitude testing were the effects of the damping material, bolt torque, and input force level. High amplitude testing investigated the effects of damping material, projectile mass, projectile speed, and programmer to alter impact duration.

2.2.2 Input Estimation

As previously stated, resonant plate shock testing is conducted by rigidly attaching a test fixture and part to one side of a resonant plate and impacting the opposite side with a projectile. This testing produces high amplitude impulse input events which are too high for standard sensors to measure and capture the input characteristics, requiring the use of expensive shock specific instrumentation. A typical load cell would not withstand the subjected high amplitude impulses, so the mass and speed of the projectile are used to experimentally design the correct response using trial and error. A programmer of a softer material such as felt or rubber can be placed on the test fixture at the impact location for further input control. [10] This trial and error method of setting up a test requires much experience and many trials to meet the desired specifications when only monitoring the output. Non-linear simulations can be made of the entire system, but if a linear model was used in calculating input characteristics, the input could be monitored during experimental testing.

A low amplitude frequency response function can be measured using the typical impact testing method. On the same system, a high amplitude response can be measured using the typical shock testing method. A frequency response function (FRF) is the output divided by the input by definition, therefore multiplying the inverse of the FRF by a second different amplitude output should result in the correct estimate of the second different amplitude input.

An overview of this method can be seen below in Figure 6. The low amplitude measurements and calculations are seen in green and the high amplitude measurements and calculations are seen in red. Only A, B, and C are measured. D, E, and F are the fast Fourier transforms of A, B, and C, respectively. G is the FRF of E divided by D. H, which is the shock input estimation, was calculated from F divided by G.

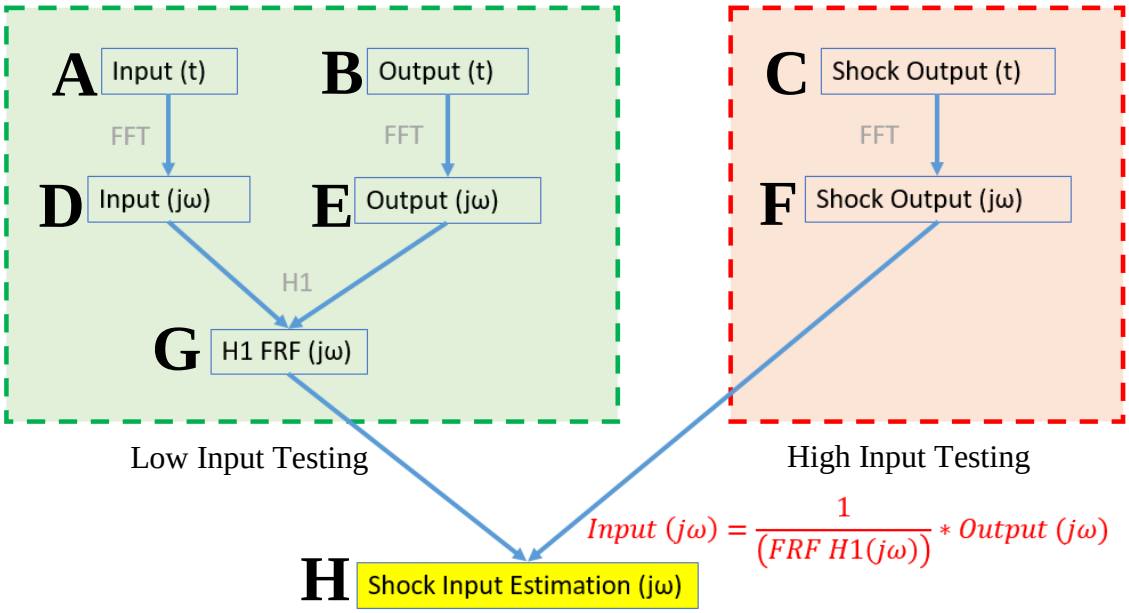

Figure 6. Input Estimation Method Overview

The process with experimental data is shown below in Figure 8. The low amplitude measurement is a light impact on the structure from an impact hammer. The same system is then impacted by a high amplitude shock, of which the input is unknown. Initially, 0.4 seconds of time was recorded for the low amplitude measurements, but was reduced to 0.1 seconds. This time duration of 0.1 seconds was selected to eliminate any potential for accidental inputs into the system after the initial impact. The sampling frequency was 20,480 Hz. The shock input was measured over 1.0 seconds, but was reduced to 0.1 seconds as well. The initial shock measurement sampling rate of 1,250,000 Hz was decimated to match the low amplitude sample rate of 20,480 Hz. This was done so computations could be performed without the ill effects of differing sampling frequencies and lengths of test data.

An elliptical lowpass IIR filter seen in Figure 7 was designed in MATLAB to apply to the shock data before downsampling. To achieve the cutoff frequency of 10,240 Hz, the passband frequency was 10,240 Hz and stopband frequency was 10,250 Hz. 40 dB of stopband attenuation was selected, twice what is absolutely necessary with a 0.01 passband ripple. At that low of an amplitude, filter ripple should have a minimal effect. The data was zero phase filtered, meaning that it was passed through the filter once forward and once backward, thus eliminating the effects of phase.

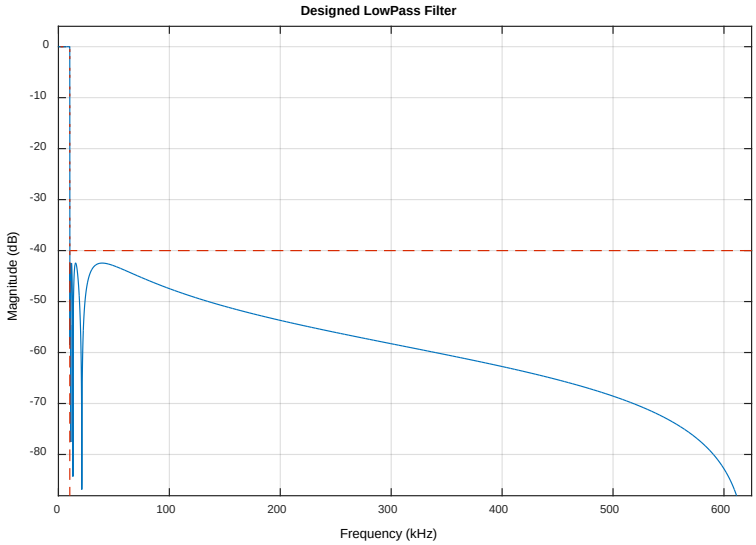

Figure 7. Low Pass IIR Filter

The filter is used before decimating the shock data to avoid aliasing.

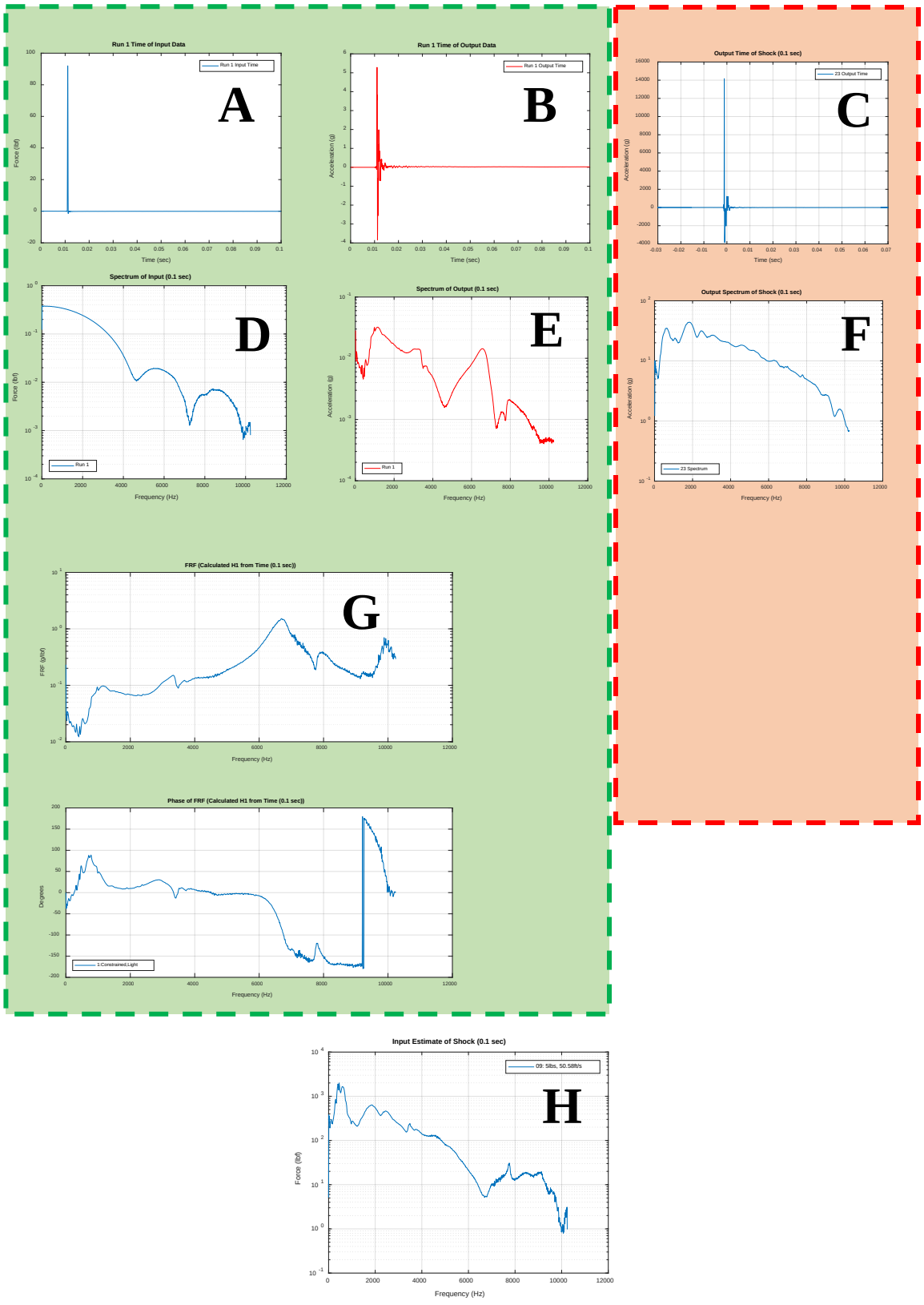

Figure 8. Input Estimation Method Overview with Example Experimental Data

This estimated shock input can be calculated, but there is no definite way to verify that this process is correct because the input spectrum was not measured. To validate that the process is correct, it must be performed with low amplitudes where the input is known.

An inverse fast Fourier transform of the shock input estimate will result in the estimated time domain of the high amplitude shock event. This was validated and performed on the shock events and trends were monitored.

2.2.3 Modal Analysis

Whether there is significant relative motion created on one of the other axes (specifically the torsional vibration) between the plate that is impacted and the plate of the response is unknown. This could mean that there is more energy in the system that the test component experiences, but this energy is not included in the uniaxial accelerometer measurement. If this is true, the test data becomes less meaningful and doesn't represent what the part under test is actually experiencing. This would mean that the part under test is being over tested.

A full modal analysis of the damped plates with a fixture and impact pad using 3 PCB 356A33 and 5 PCB T356A31 triaxial accelerometers was performed with the intent to understand which modes actually do significantly contribute to the response of the part. These accelerometers have a range of 2 to 10,000 Hz in the y and z direction and 2 to 7,000 in the x direction. A Modal Shop K2007E01 SmartShaker was used with a steel stinger and PCB 208A02 force transducer, with a range up to 36,000 Hz. The input location was 0.5 inches from the edge of the plate on the side with the impact pad. The shaker was mounted on a cinder block and hot glued to the base to limit motion. The full test setup can be seen in Figure 9.

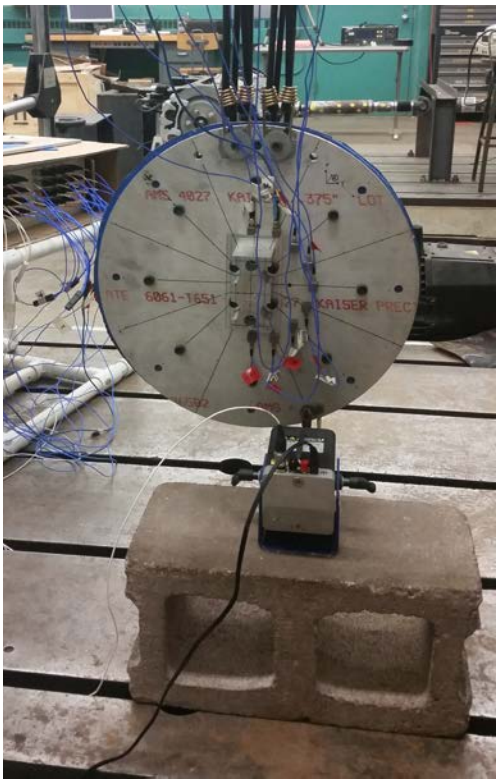

Figure 9. Modal Analysis Test Setup

The accelerometers were mounted using Loctite 454 to reduce the potential of a mounting resonance and increase the maximum valid frequency of the data. Using the roving accelerometer method, 154 output locations were measured and used in the modal analysis.

Using a sampling frequency of 20,480 Hz, a sine chirp of the entire bandwidth was produced. An excitation time of 75 percent of the acquisition time was set to allow enough time for the energy input to decay to the noise floor so the transient is totally observed, thus eliminating leakage. The output voltage was 0.5 volts with the intent to limit the nonlinearities of the system while still inputting enough energy to excite the structure. 50 averages were taken for each test run.

Because this test was largely unsuccessful in producing a consistent set of modal data, three other modal tests were performed. A new single plate of 1.125 inch thickness and 17 inch diameter was manufactured. For all three of these MIMO shaker tests, ten PCB 356A13 traxial accelerometers were used in the configuration shown in Figure 10 (response locations circled). These accelerometers have a range of 2 to 8,000 Hz in the y and z direction and 2 to 5,000 in the x direction. Two Modal Shop K2007E01 SmartShakers were used with PCB 208C02 force transducers. The stingers were changed to nylon (length of 7 inches). The input locations were 0.5 inch from the edge of the plate and 120 degrees away from each other, as seen in Figure 10. Another notable change from the previous single test was the difference in support. The plate was suspended using fishing line with the intent of increasing repeatable between tests.

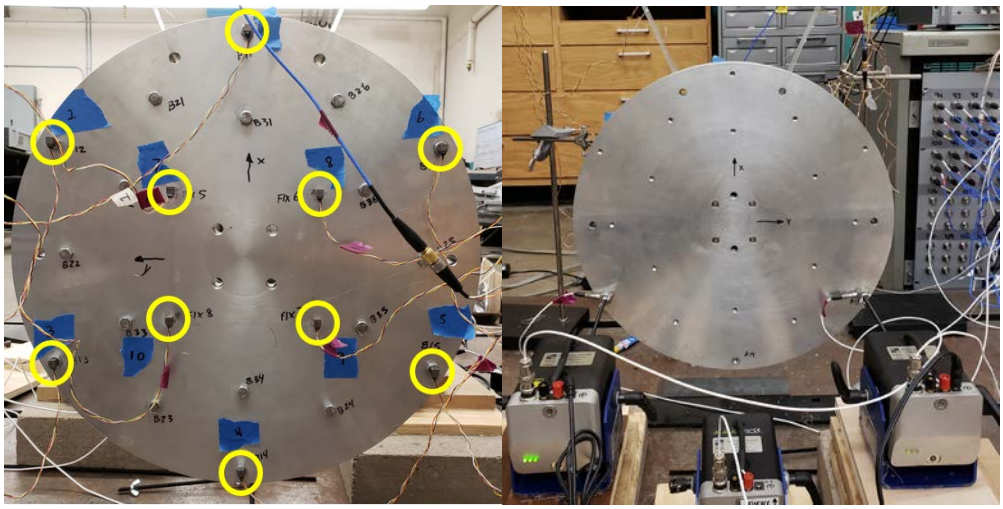

Figure 10. Back (Left) and Front (Right) of Modal Setup of Test 1 (Only Plate)

The accelerometers were again mounted with Loctite 454, but were not removed during the duration of these three tests, meaning only 10 response locations were included in the results.

A bandwidth of only 4096 Hz and burst random excitation from 800 to 4000 Hz was used. The burst time was 70 percent of the excitation duration. The output voltage was increased to 0.7 volts to input more energy into the system. The structure should give a linear response, so increasing the input should not have ill effects. 50 averages were again taken.

A setup of test 2 (plate and fixture) can be seen in Figure 11. The four bolts mounting the fixture were torqued to 30 ft lbs.

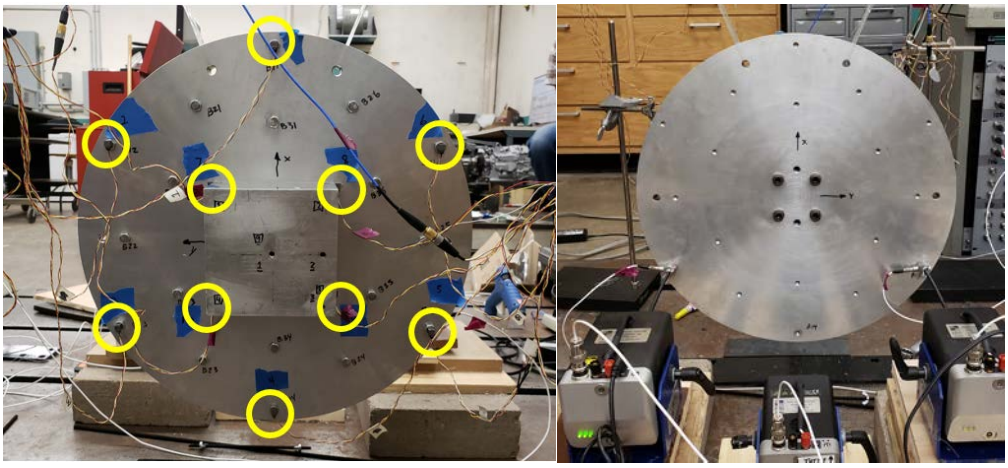

Figure 11. Back (Left) and Front (Right) of Modal Setup of Test 2 (Plate and Fixture)

Test 3 (plate, fixture, and impact pad) is in Figure 12. The two bolts mounting the impact pad were torqued to 20 ft lbs.

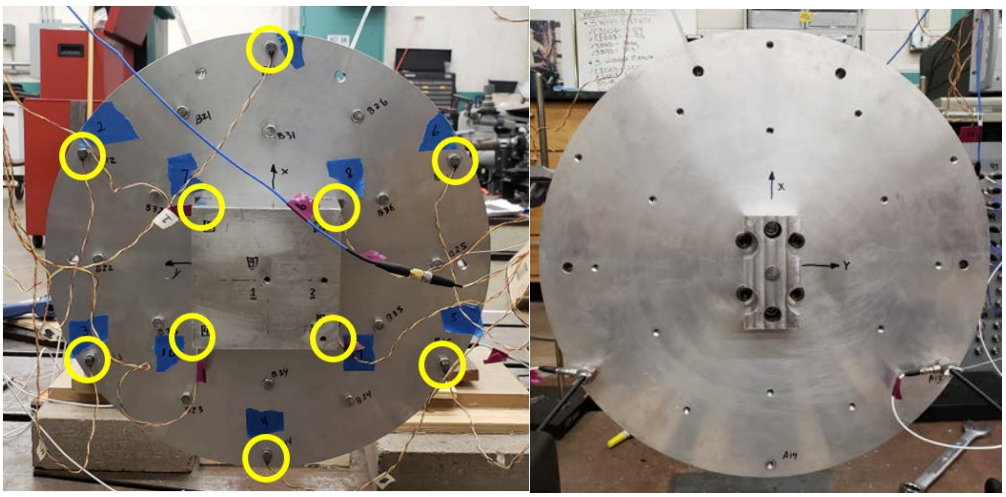

Figure 12. Back (Left) and Front (Right) of Modal Setup of Test 3 (Plate, Fixture, Impact Pad)

All three of these tests can be compared to the numerical and FEA models.

3 Results

3.1 Variable Thickness Plates

A test fixture must be included in the design to model a more realistic test. In practice, this test fixture would contain a part mounted as it would be in the field. For this research, a 3 inch thick, 5 inch square aluminum test fixture was rigidly attached to the center of the plate. This matches the experimental test system. A finite element model of the system can be seen in the following Figure 13. The addition of a fixture increases all of the natural frequencies of the modes because there is more apparent stiffness in the structure. All of the mode shapes and frequencies can be seen below in Figure 13. The drumhead modes of the plate still appear to be the only modes that significantly contribute to the response at the part's center.

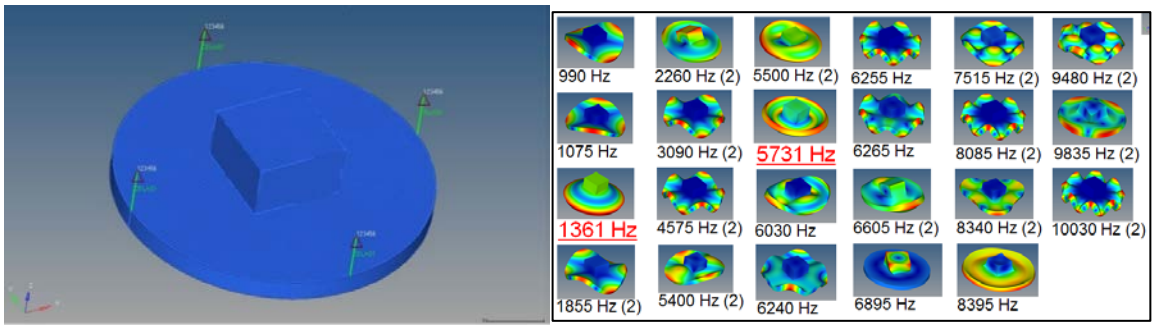

Figure 13. FE Model of Plate with Test Fixture (Left), All Mode Shapes (Right)

A 2 inch by 4 inch aluminum impact pad was added to the model, attached rigidly to the opposite side than the fixture, also at the center of the plate. The pad is 1.75 inches thick. There are four 1 inch diameter holes in a 2 inch by 2 inch pattern. These allow bolts to attach the fixture to the opposite side of the plate. The impact pad has two 0.625 inch holes for bolts to attach the impact pad to the plate. This geometry matches the experimental system. The purpose of this impact pad is to protect the plate system from damage during high velocity impacts. The mode shapes from this model produce nearly identical modes at very similar frequencies, as seen in Figure 14.

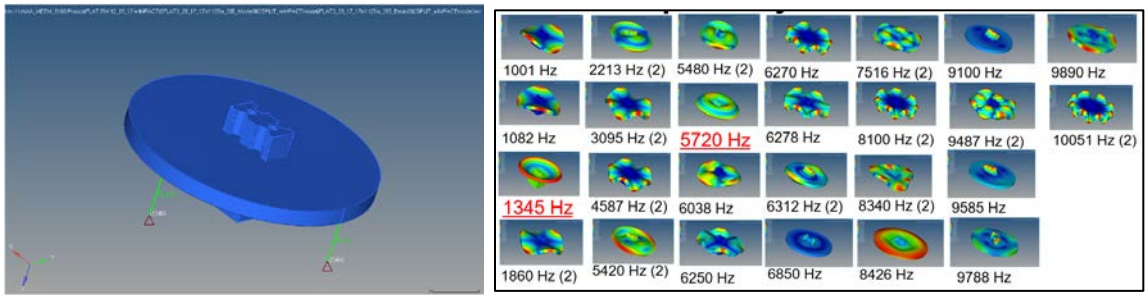

Figure 14. FE Model of Plate with Test Fixture and Impact Pad (Left), All Mode Shapes (Right)

3.1.1 FEA Shock Response Calculation Method

From this FEA model, a simulated FRF of the structure impacted by a unit impulse on the center of the impact pad and response at the center of the fixture can be obtained, as seen in Figure 15. Overall modal damping of the structure was 1 percent, as this is low enough to make the peaks in the FRF very apparent and changes in the SRS obvious. An analytically created input spectrum of a 1 millisecond, 1 N amplitude haversine can be seen in Figure 15.

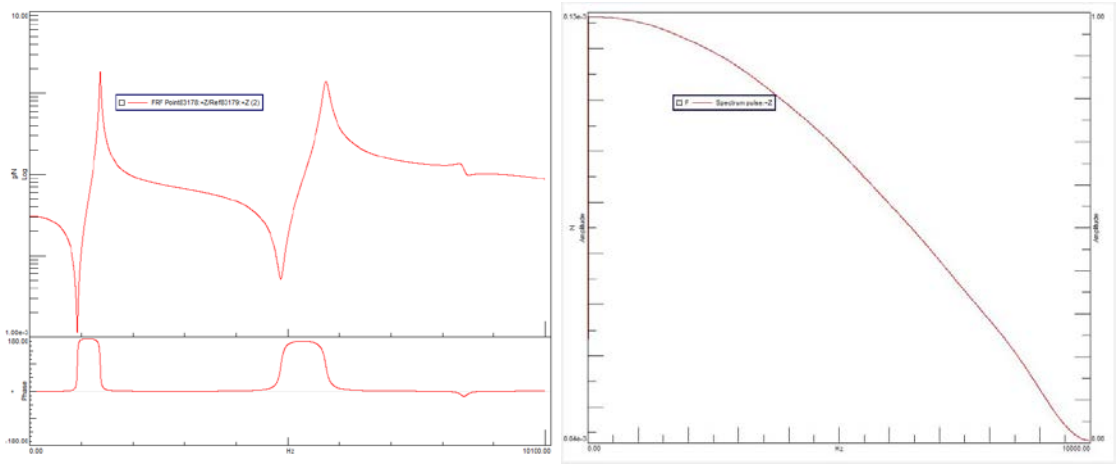

Figure 15. Simulated FRF of Structure (Left), Analytical Input Spectrum (Right)

Multiplying the structure's FRF by a chosen input spectrum results in an output response, which is found in Figure 16. An IFFT of this output response produces the time domain response, also shown in Figure 16.

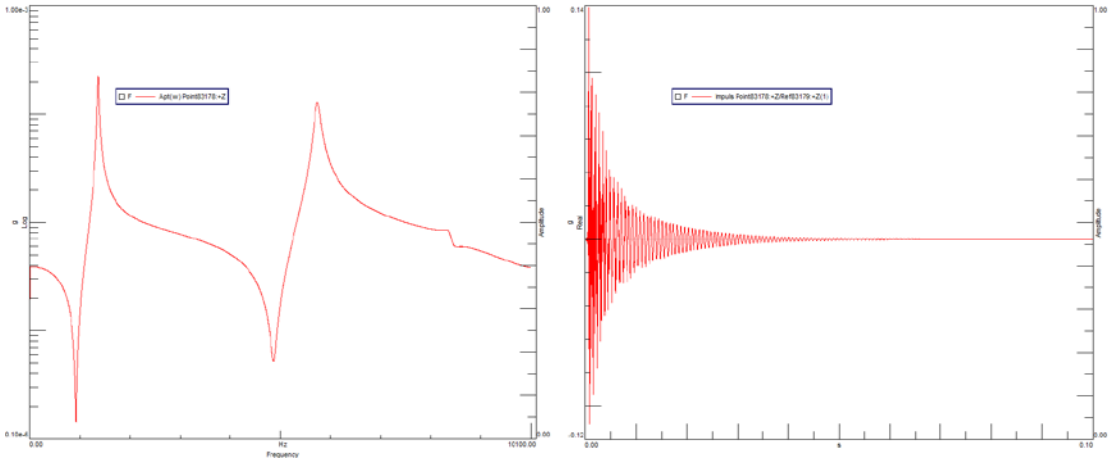

Figure 16. Response of System from Analytical Input (Left), Time Domain of Response (Right)

From the output time domain response, a shock response spectrum can then be calculated. A Q of 10 (5 percent damping ratio) is used which is a standard damping factor for

calculating the SRS. The absolute maximax acceleration SRS was calculated. This overall process was developed to be able to compare different input levels of SRS, but is also found to be the best method to analytically simulate a SRS. [11] The resultant SRS is seen in Figure 17.

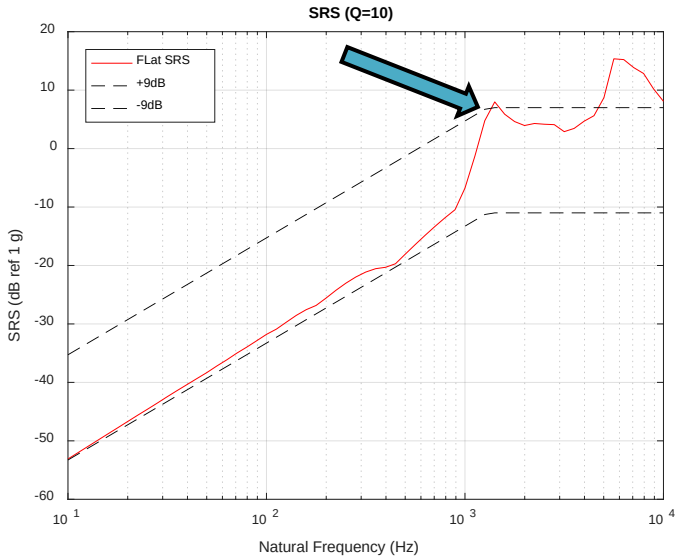

Figure 17. Shock Response Spectrum of Simulated System from Analytical Input with Sample Target Bands

The two contributing natural frequencies of the plate can obviously be seen in the shock response spectrum as the peaks. The first membrane mode is the knee frequency indicated by the arrow in Figure 17. To meet a target band of the shape seen above, the second frequency is not desired to appear in the shock response spectrum. Simulations using higher modal damping result in a more rounded knee frequency and lower relative amplitude of the second peak in the SRS, but this alteration does not produce a relative low enough amplitude of the second peak to meet this selected target band.

The shape of the SRS to match is selected by producing a SRS from experimental data taken in the field. Bounds from this curve allow controlled laboratory testing to vary from the selected curve by a selected margin. For the experimental test in this study, a curve of 12 dB/octave from 10 to 1300 Hz followed by 0 dB/octave from 1300 Hz to 10,000 Hz with bounds of +/- 6 dB is selected.

3.1.2 Flat, Concave, Convex Plate Geometry

In an attempt to increase the frequency of the higher frequency mode out of the frequency band of interest, the cross sectional geometry of the plate was modified.

The geometry and contributing mode shapes of the initial flat plate are seen in the following Figure 18.

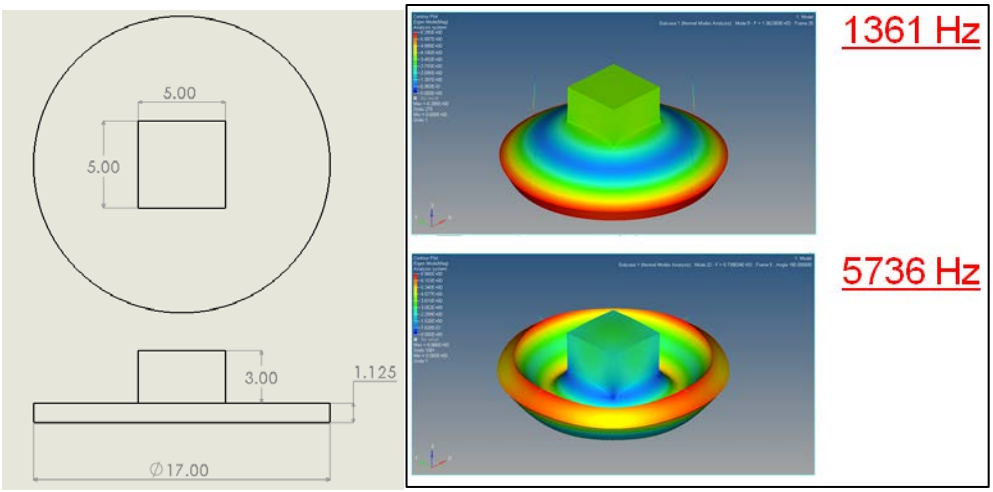

Figure 18. Geometry of Flat Plate (Left), Contributing Modes (Right)

The first bending mode, which is the knee frequency in the SRS, is computed to be 1361 Hz.

The geometry and contributing mode shapes of a plate with concave thickness are seen in Figure 19. The plate was designed with the intent of increasing the mass by 4.5 lbs. This allows the plate to remain within a weight that is realistic for a single person to work with, but more extreme weights could be used.

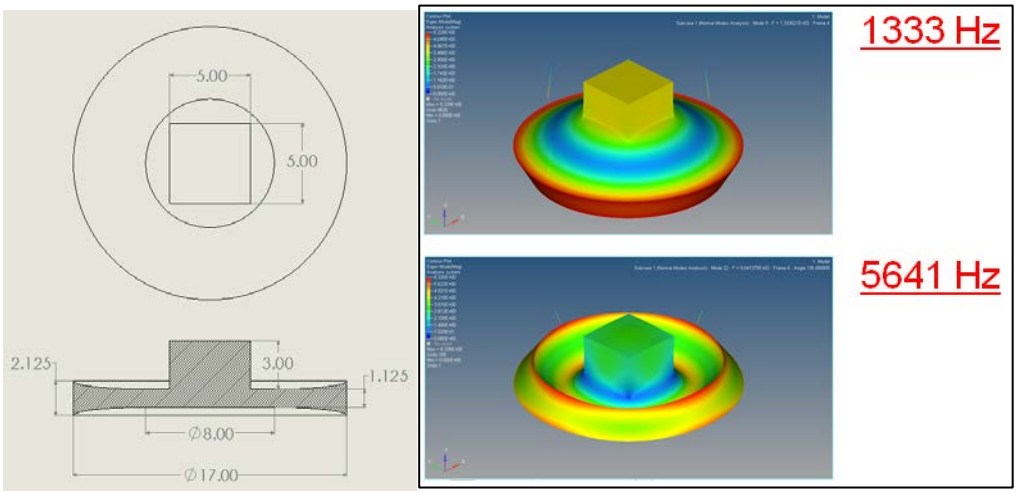

Figure 19. Geometry of Concave Plate (Left), Contributing Modes (Right)

It is obvious that both frequencies decreased. The difference between the frequencies also decreased compared to the flat plate.

The geometry and contributing mode shapes of a plate with convex thickness are shown in Figure 20. The plate was designed with the intent of decreasing the mass by 4.5 lbs, as this is the same amount the concave plate was increased.

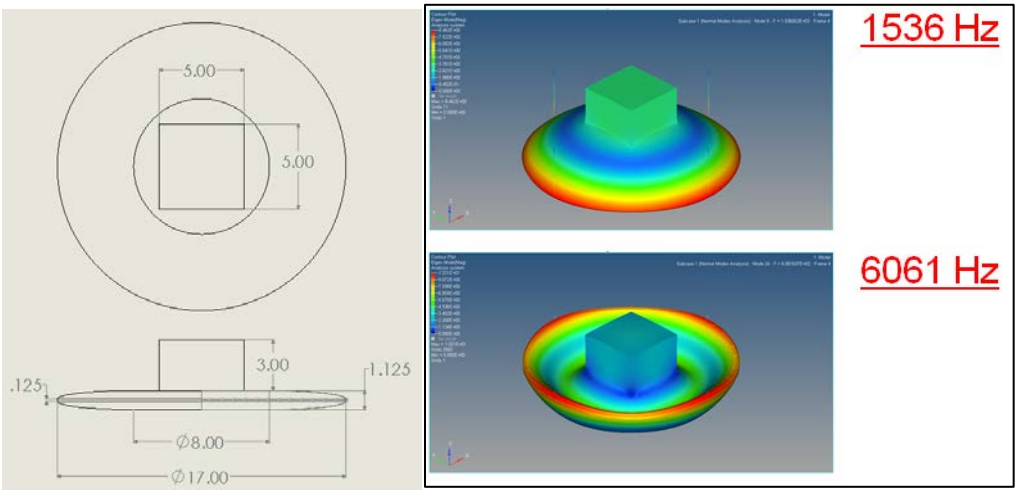

Figure 20. Geometry of Convex Plate (Left), Contributing Modes (Right)

Both frequencies of interest increased compared to the flat plate and the difference between the frequencies also increased.

Using the selected material properties, the flat plate was calculated to be 32.38 lbs, the convex plate was 27.88 lbs (-4.5 lbs than the flat plate), and the concave plate was 36.89 lbs (+4.5 lbs than the flat plate).

The unit impulse FRFs of all of the plate geometries can be seen below in Figure 21.

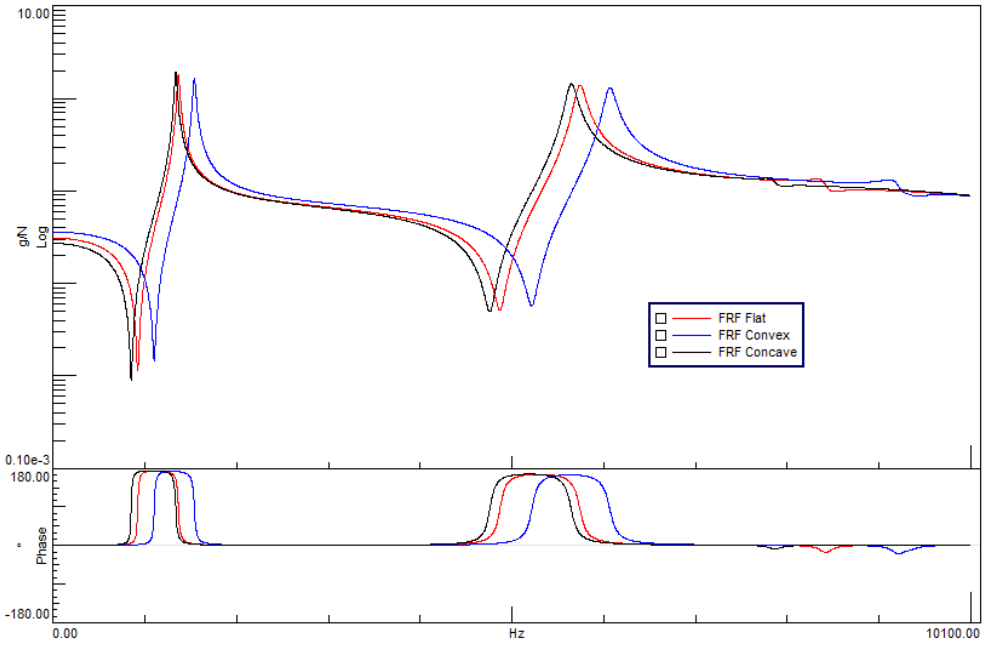

Figure 21. Frequency Response Functions of Flat, Convex, and Concave Geometries

The natural frequencies of the contributing modes taken from the frequency response functions are numerically displayed below in Table 5. The convex plate increases the separation of contributing mode 1 and contributing mode 2 significantly more than the concave plate decreases the separation of the modes.

Table 5. Contributing Natural Frequencies (Hz) of Flat, Convex, and Concave Geometries

	Contributing Mode	
	1	2
Flat	1361	5736
Convex	1536 (+175)	6061 (+325)
Concave	1333 (-28)	5641 (-95)

The natural frequency trends from the FRFs can also be seen in the shock response spectrum curves, which can be seen below in Figure 22. Due to the log scale, the separation effect appears less dramatic.

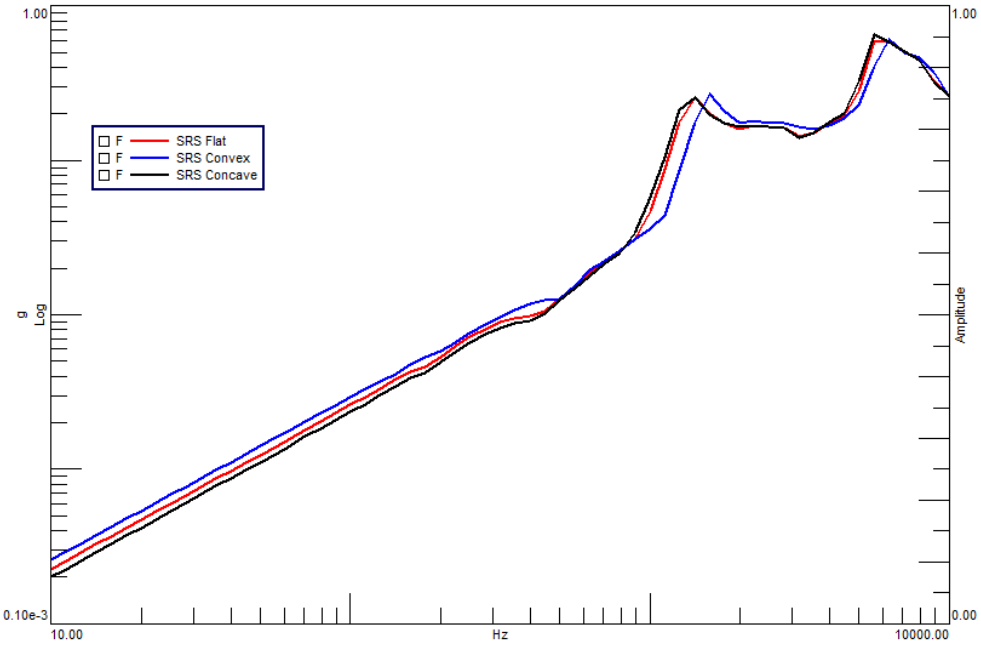

Figure 22. Shock Response Spectrums of Flat, Convex, and Concave Geometries

The convex plate geometry separated the bending modes' natural frequencies. This strategy could be used to design resonant plates more robustly and to control the contribution of the modes in the FRF. Because the SRS is directly related to the FRF, this would ultimately control the frequency of the peaks in the shock response spectrum. Simulations should be done on more extreme geometries using a larger overall thickness variation to separate the modes further, eventually pushing the second bending mode frequency above 10,000 Hz and out of the frequency range of interest.

3.2 Numerical Model

The constrained numerical MATLAB model was used to investigate the effects of impulse duration and damping. The time duration of the pulse was 0.5 ms with an amplitude of 10,000 N. The input and resulting impulse response of the system are seen below in Figure 23. The times traces were 0.1 seconds, but are shortened for viewing.

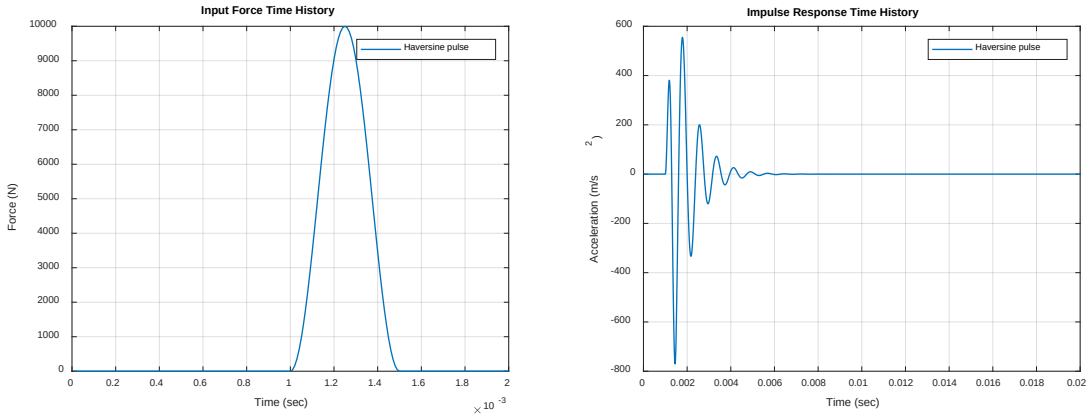

Figure 23. 0.5 ms Input Time (Left), Impulse Response of System (Right)

The input haversine has a dominant pulse frequency of 2000 Hz. The response is nearly symmetrical because the impulse time duration is near the response time of the system. Using varying values of damping, the SRS was calculated from this 0.1 second time domain response, as seen in Figure 24.

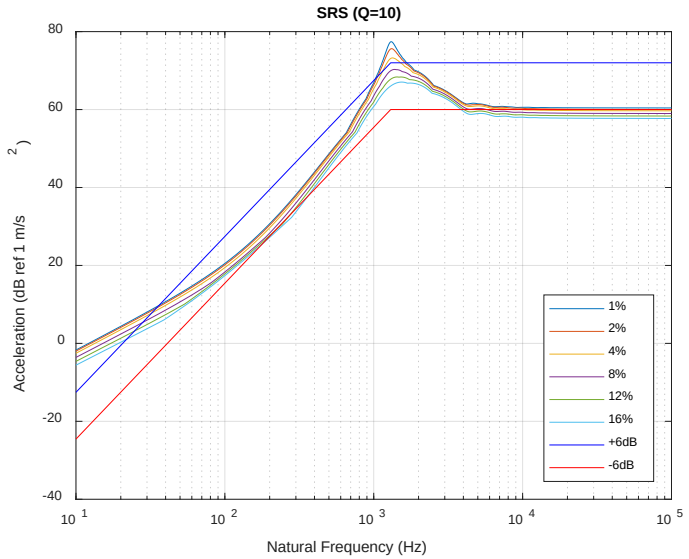

Figure 24. SRS from 0.5 ms Input Using Varying Damping Values

It can be seen that 8% damping appears to allow the knee frequency to stay within the selected test criteria bands. These specifications allow +/-6 dB on either side of the SRS.

The general shape is 12 dB/octave until 1300 Hz, followed by a horizontal response. These test specifications are created by using experimental data and retrofitting a curve to simulate real world shock events.

There is a low frequency vertical shift. This is not due to velocity or experimental issues in this case because this is entirely analytical. To prove this, the initial and corrected velocity from this acceleration response can be seen below in Figure 25.

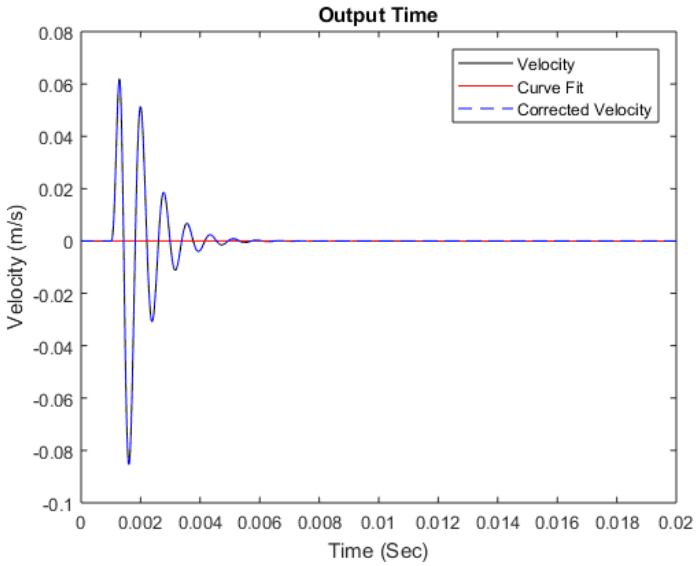

Figure 25. Velocity and Corrected Velocity of System

This low frequency slope in the SRS in Figure 24 is due to the boundary condition. The stiffness to ground creates a boundary condition that is not free-free. The constrained boundary condition will alter this low frequency content below approximately 400 Hz, but will not significantly impact the response above roughly 400 Hz.

A longer impulse time was created of 5 milliseconds, or a dominant frequency of 200 Hz. This results in a response that appears as if the structure was impacted twice, as seen in Figure 26. The system responds faster than the pulse is completed. This is very undesirable and will create a ripple effect in the input spectrum. This is not found in free-free experimental data, but with constrained boundary conditions, the effects are obvious.

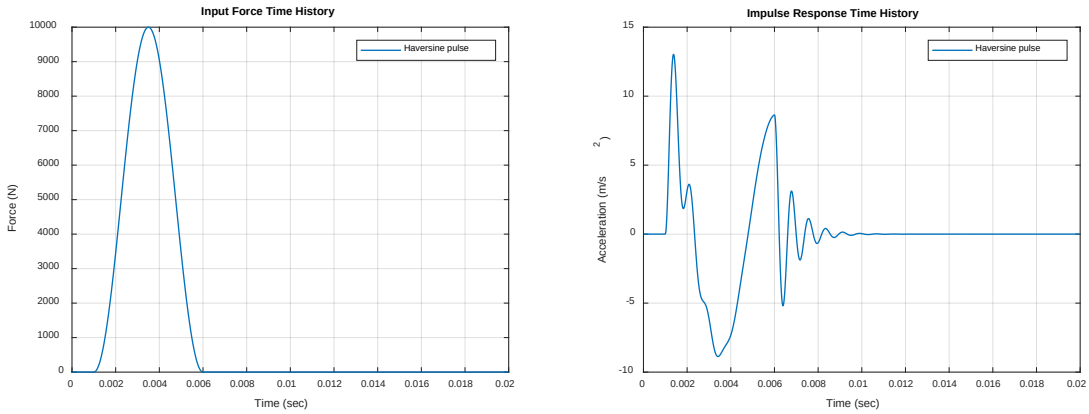

Figure 26. 5 ms Input Time (Left), Impulse Response of System (Right)

Figure 27 displays the SRS from varying system damping parameters calculated using the impulse response.

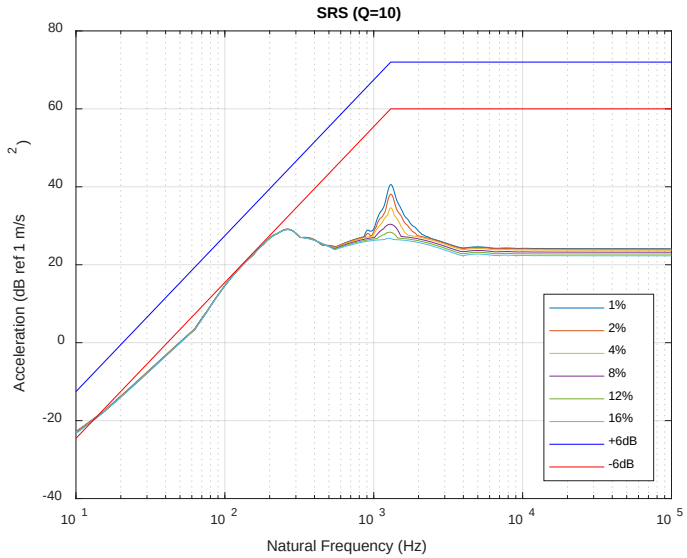

Figure 27. SRS from 5 ms Input Using Varying Damping Values

If the system is not held in a free-free state, the dominant frequency of the impact will always be present in the SRS of the system because the SRS simply estimates the peak amplitude of every natural frequency of the entire system. This must be considered when deciding the materials of the projectile and the impact surfaces, otherwise the designed knee frequency may not be the knee frequency of the resulting SRS. This was repeated for an impulse of a frequency of 20,000 Hz, which is significantly higher than the natural frequency of the system. The input time and impulse response of the system is found in Figure 28.

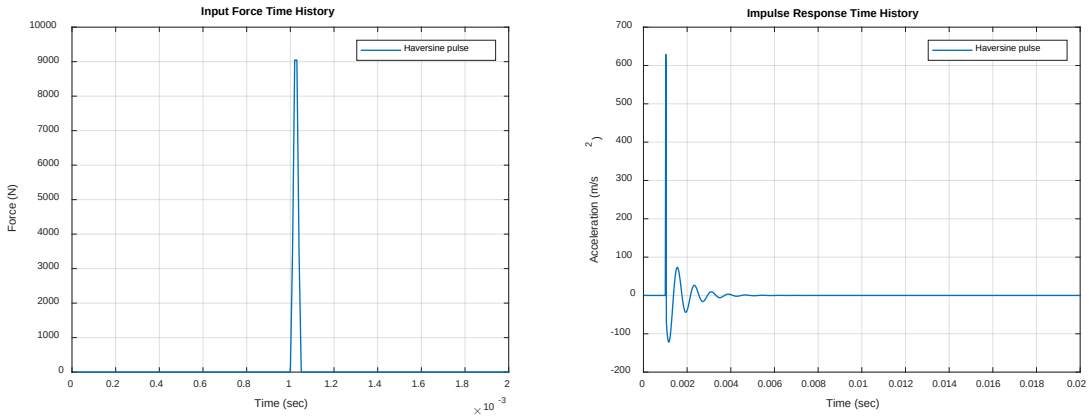

Figure 28. 0.05 ms Input Time (Left), Impulse Response of System (Right)

The system is not impacted hard enough to respond in the negative direction. The stiffness of the boundary condition results in the energy being attenuated before reflecting back. This is also not desired, as the resulting SRS will only represent the energy in a single direction with little oscillation. The SRS of the responses with varying structural damping is found in Figure 29.

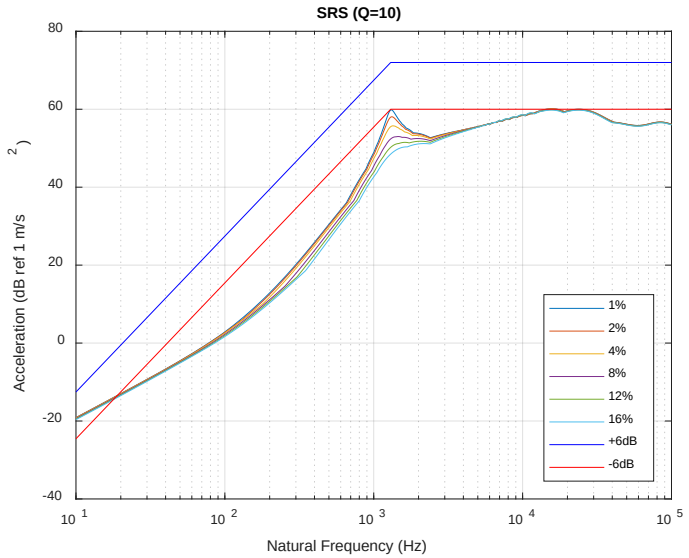

Figure 29. SRS from 0.05 ms Input Using Varying Damping Values

The SRS appears to increase past the maximum calculated natural frequency of 10,000 Hz. The SRS has a peak near 20,000 Hz, which is the dominant frequency of the impact. This is not desired to meet the test specifications. It can be concluded that if the boundary conditions of the structure are not free-free, the SRS will include the dominant frequency of the impulse.

3.3 Experimental Testing

Experimental testing was performed on a fabricated plate in free-free and constrained boundary conditions. Varying physical parameters of the free-free system were altered to monitor the effect on the resulting SRS. Low amplitude impacts were compared from the free-free and constrained boundary conditions to monitor differences between the two systems. High amplitude shock events were investigated in the constrained boundary condition. Investigation of the SRS calculation and velocity correction is performed.

3.3.1 Low Amplitude Testing Alterations

The plate was suspended vertically using bungee cords to create a free-free boundary condition. An accelerometer provided time data to calculate a SRS under different input conditions. For this testing, a peak time domain output of 100, 200, 300, and 400 g was measured. An example of time data from a 200 g impact can be seen below in Figure 30.

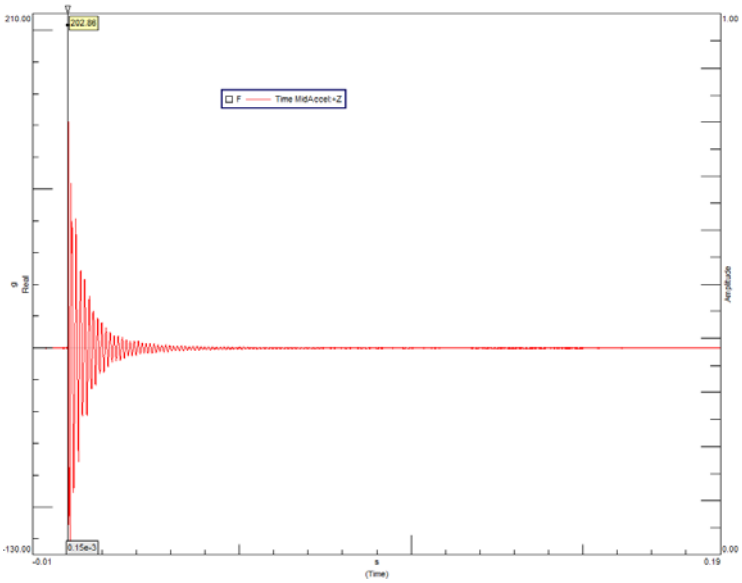

Figure 30. 200g Peak in Time Domain Response of Structure

Using the log decrement method on the time domain response of the plates with no damping material (undamped) and plates damped with EAR C2003 (damped), a damping ratio of approximately 3.6% and 24.8%, respectively, was estimated. [10]

3.3.1.1 Repeatability and Input Force Levels

For all of the SRS calculations, the damping ratio of each natural frequency was assigned a Q of 10, which is a damping ratio of 5%. This is a common value used for the SRS calculation. [12] The number of points per octave calculated was 12. Unless specified, the maximax SRS is shown. Maximax is defined as the maximum of both positive and negative primary and residual responses. The primary portion of the shock event is the maximum

response during the excitation, while the residual is the peak response after the initial excitation has completely decayed. [13] All SRS calculations used David Smallwood's MATLAB code, which is the standard used in most software, including LMS TestLab.

Five impacts show the repeatability of the measurement for 200 g on an undamped plate (left) and a plate with the damping material (right), as seen in Figure 31. The three plates that make up the plate sets were secured by eight equally spaced bolts in a 11.5 inches diameter circular pattern. For this test, these bolts were torqued to 30 ft lbs. Similar repeatability was seen for other tests.

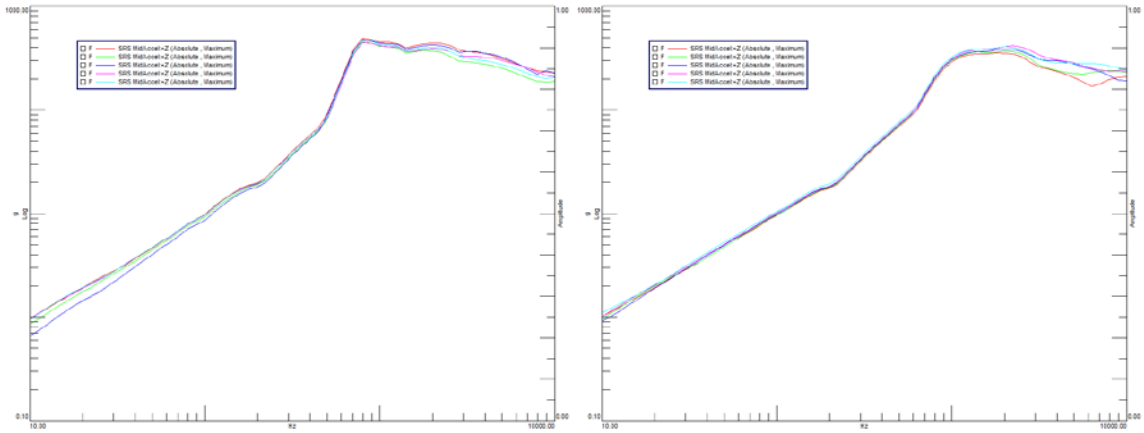

Figure 31. Five SRS of 200g Maximum Time Domain Response on Undamped (Left), and Damped Plates (Right)

This shows a typical response shape of a resonant shock test. [7] Figure 32 shows single tests of 100, 200, 300, and 400 g peak output in the time domain on an undamped plate bolted with a torque of 30 ft lbs (left) and a plate with damping material bolted with a torque of 30 ft lbs (right).

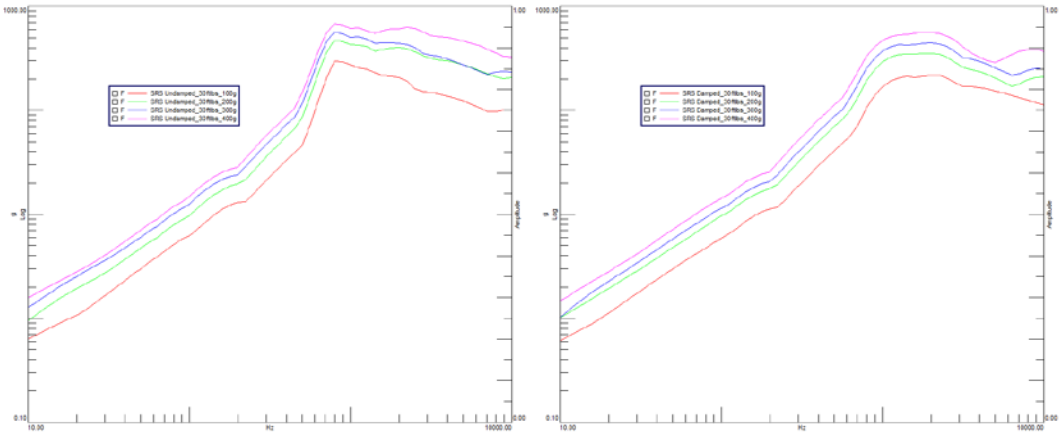

Figure 32. SRS of 100, 200, 300, and 400g Maximum Time Domain Response on Undamped (Left), and Damped Plates (Right)

For both plate sets, the SRS appears to simply shift vertically with increasing input amplitude. The SRS of the undamped plate appears to have a much more defined knee frequency, while the SRS of the damped plate is significantly more rounded.

3.3.1.2 Damping Material Effects

Figure 33 compares the damped and undamped plate sets. The red SRS show the damped plate system and the blue SRS show the undamped plate system at varying amplitude. 30 ft lbs of torque on the bolts is on the left and 15 ft lbs of torque is on the right.

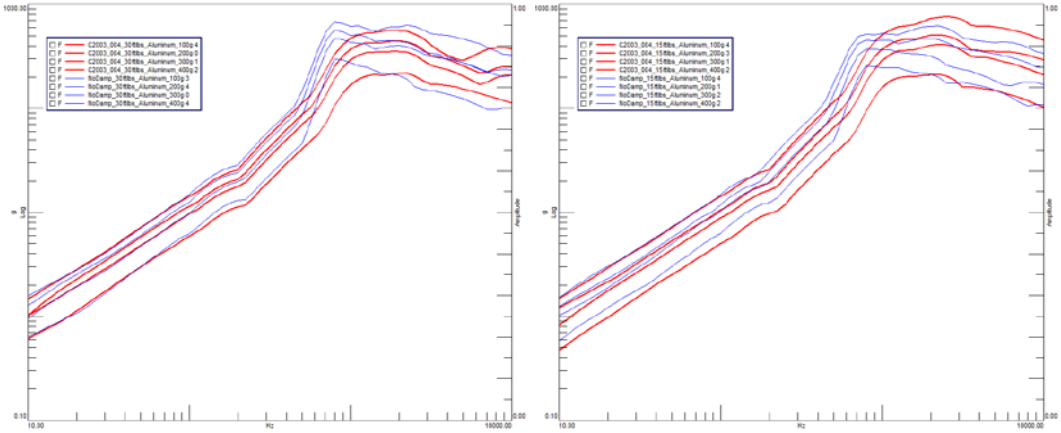

Figure 33. SRS of 100, 200, 300, and 400g Maximum Time Domain Response on Damped and Undamped Plates with 30 ft lbs Bolt Torque (Left), and 15 ft lbs Bolt Torque (Right)

The conclusion drawn from this study is using a bolt torque of 30 ft lbs, more damping produces a lower knee amplitude and a more rounded, higher knee frequency. For 15 ft lbs, there is a more rounded, higher knee frequency with an increase in damping.

3.3.1.3 Bolt Torque Effects

In Figure 34, the red SRS shows the bolts tightened to 15 ft lbs while the blue SRS shows the bolts tightened to 30 ft lbs increasing in input amplitude. The undamped plate system is on the left while the damped plate is on the right.

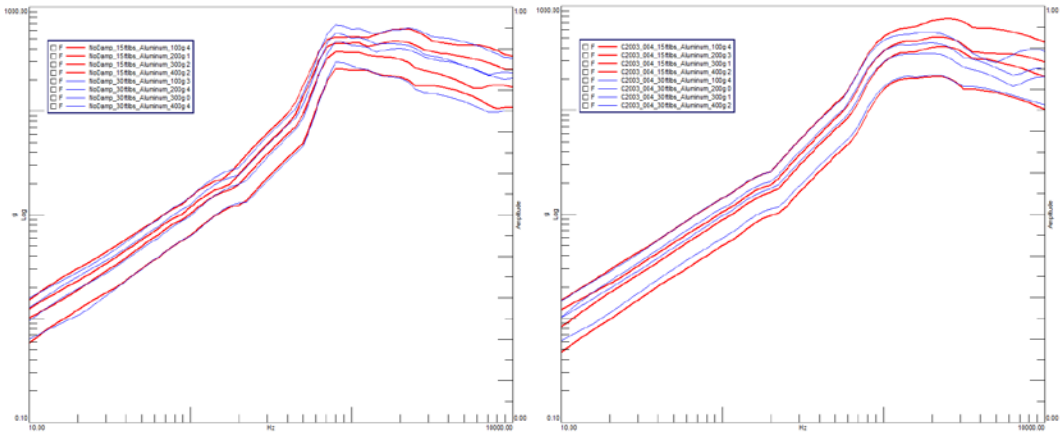

Figure 34. SRS of 100, 200, 300, and 400g Maximum Time Domain Response Using 15 and 30 ft lbs Bolt Torque on Undamped (Left) and Damped Plates (Right)

The conclusion drawn from this is that for the undamped plate, less bolt torque results in a more rounded lower knee amplitude. This effect was also described as being seen in testing done by Morse. [8] This is because the system allows the plates to shear and ultimately implements more damping between the aluminum plates' interfaces. The damped plates do not have this noticeable difference because there is already enough damping in the system.

3.3.1.4 Programmer Effects

Programmer material can greatly affect the resulting SRS. The impact hammer tip hardness was changed from aluminum to increasingly soft elastomers. The SRS and input autopower spectrum can be seen overlaid in Figure 35. The plot on the left is the undamped plate and the plot on the right is the damped plate.

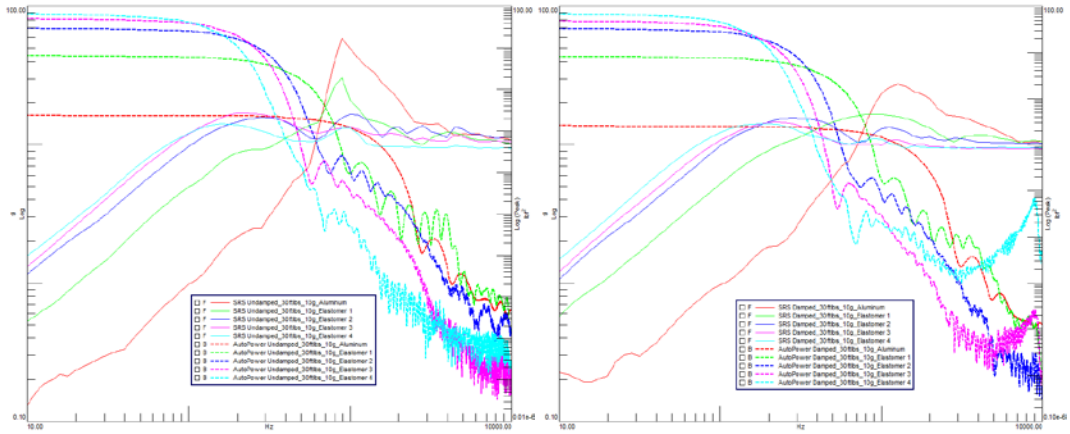

Figure 35. Varying Hammer Tip Hardness SRS overlaid on Input Autopower Spectrum of Undamped (Left) and Damped Plates (Right)

The input autopower spectrum rolls off at a lower frequency as the hammer tip becomes softer. Each of these measurements were taken to result in a 10 g peak time domain output,

so different input forces were required. The SRS also rolls off, or is not excited, which is especially noticeable around the knee frequency. [11] This results in a perceived higher amplitude and frequency of the knee frequency for harder tips.

3.3.1.5 Off Axis Response Sensitivity

The question then arises, is the precision of the output measurement location critical? Using the damped plate set and 30 ft lbs of torque on the bolts, the structure was impacted with the 4 different amplitude levels. An accelerometer was mounted at the middle of the fixture and another accelerometer mounted 2.25" off center, which was on the edge of the same face of the fixture. This accelerometer was kept at this location throughout all testing and occasionally monitored to validate the response from the accelerometer at the middle of the fixture. This off center accelerometer location response was also used to investigate off center sensitivity on the fixture. The following Figure 36 displays these differences.

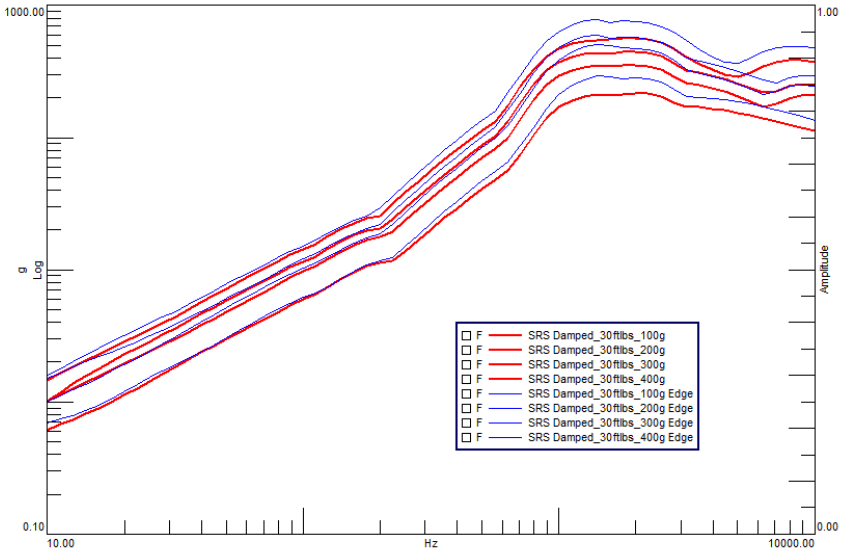

Figure 36. SRS of Damped Plate Response in Center and 2.25 Off Center (Edge) of Fixture

The accelerometer on the edge consistently experiences higher amplitudes, especially at higher frequencies (near the resonant frequency of the plate). This reinforces the idea that there are other modes participating to create motion at this off axis location. This was repeated on the undamped plate set in Figure 37.

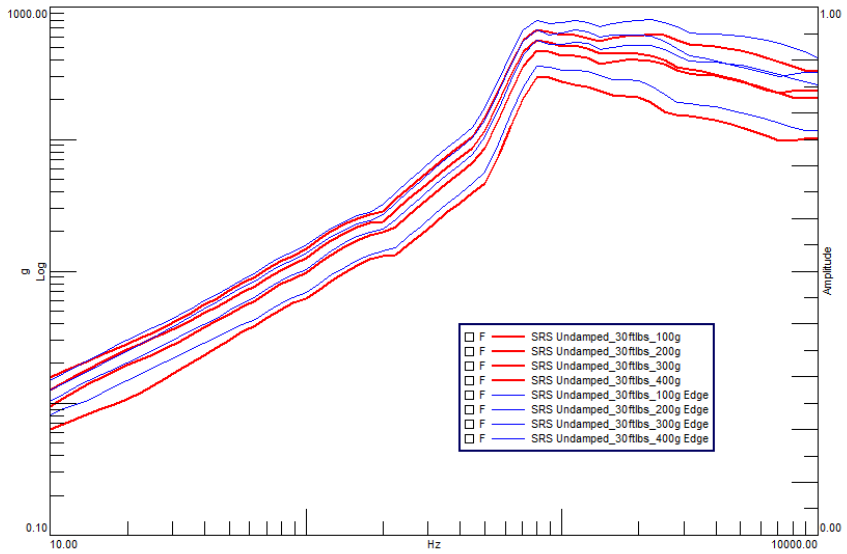

Figure 37. SRS of Undamped Plate Response in Center and 2.25 Off Center (Edge) of Fixture

The results of this are strikingly similar. There is nearly an identical increase at corresponding locations along the frequency axis.

3.3.1.6 Off Axis Input Sensitivity

Since the response location on the face of the fixture was discovered to be important, the input location should also be questioned. If the input location is not directly at the center, how much impact does this have on the resulting SRS? Two hits at the center show variance and a single hit 3.25 inches off center are shown in Figure 38. A resulting 30 g peak in the output accelerometer time trace is consistent among these hits.

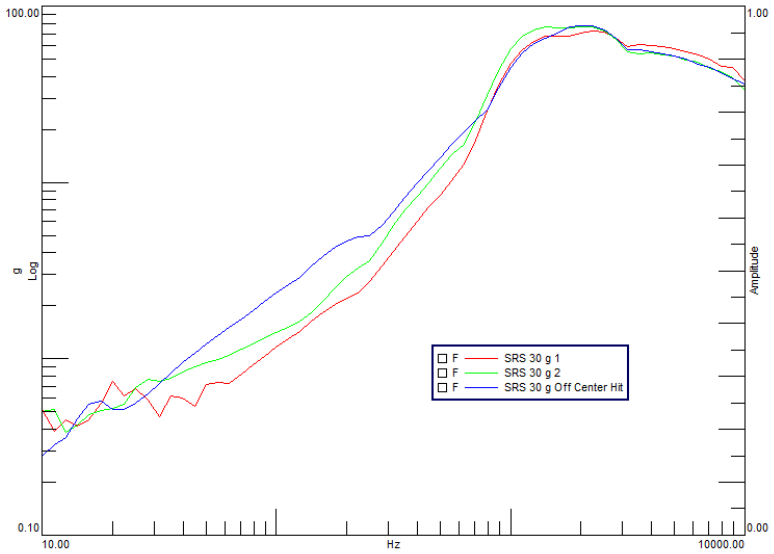

Figure 38. SRS of 30 g Impact at Center and 3.25 Inches Off Center

There is substantial noise, which effects the low natural frequencies. The two center impacts show reasonable consistency in overall shape. The off center accelerometer response is noticeably different in key areas. There is a higher amplitude at low frequencies, while still having a similar or even slightly lower amplitude at higher frequencies (even when plotted on a log scale). This was repeated for higher amplitude hits (100 g output in the time domain) which can be seen in Figure 39.

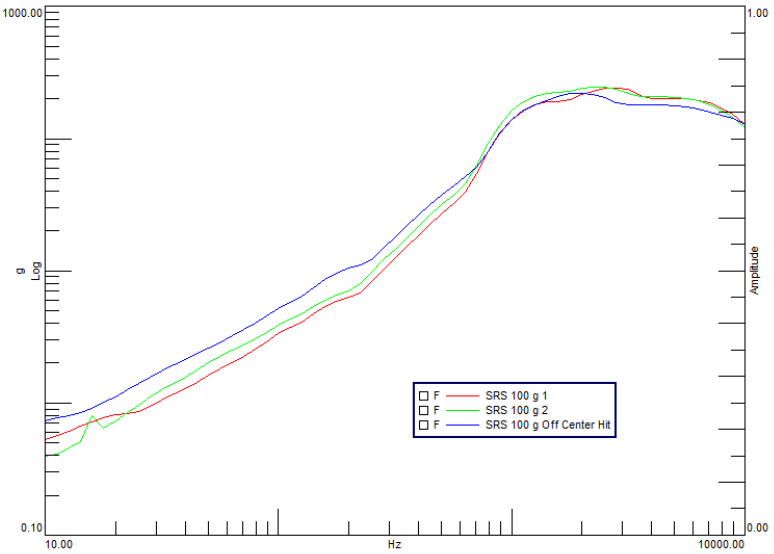

Figure 39. SRS of 100 g Impact at Center and 3.25 Inches Off Center

A difference of high amplitude at low frequency and lower amplitude at high frequency is apparent. This means that a higher velocity impact was required for the off center input to produce a similar peak time domain output. The bending mode with motion at the middle

participates more in the output if impacted at the center, as is expected. When tested at 200 g time domain peak output, these differences are amplified, as seen by the following Figure 40.

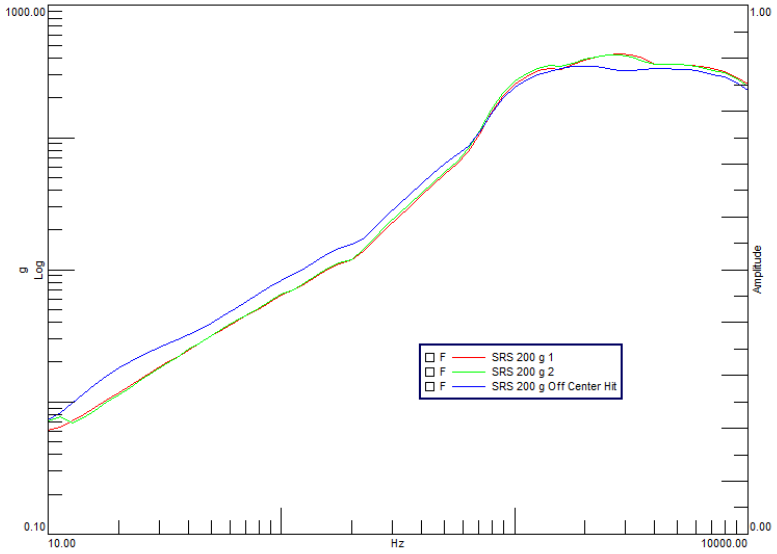

Figure 40. SRS of 200 g Impact at Center and 3.25 Inches Off Center

3.3.1.7 Fixture-Plate Relative Motion

To ensure that there is no relative motion between the plate and the fixture, accelerometers were placed on both the plate and fixture. The accelerometers are indicated in Figure 41 as channel 1 and 2, respectively. This is useful in ensuring that the boundary conditions of the fixture are rigid to the plate and do not add another degree of freedom, similar to the concept of proper mounting of the component to the fixture. [14]

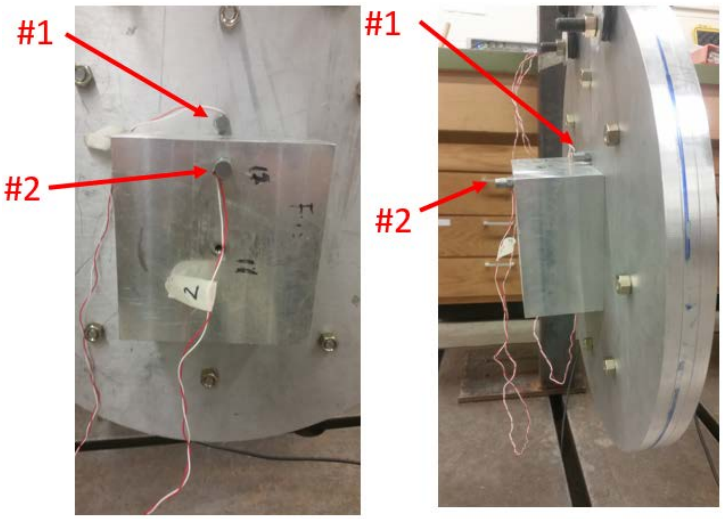

Figure 41. Accelerometer Locations to Test Relative Motion Between Fixture and Plate

The plate is impacted to produce a response of 100 g peak in the time domain. The bolts holding the fixture were tightened to 30 ft lbs and the response can be seen in Figure 42. This data was taken with a 100,000 Hz sampling frequency. This was also tested for 100 g and 300 g impacts with lower sample rates and the results were similar. This was also tested with the fixture tightened to 15 ft lbs and the results were also nearly identical.

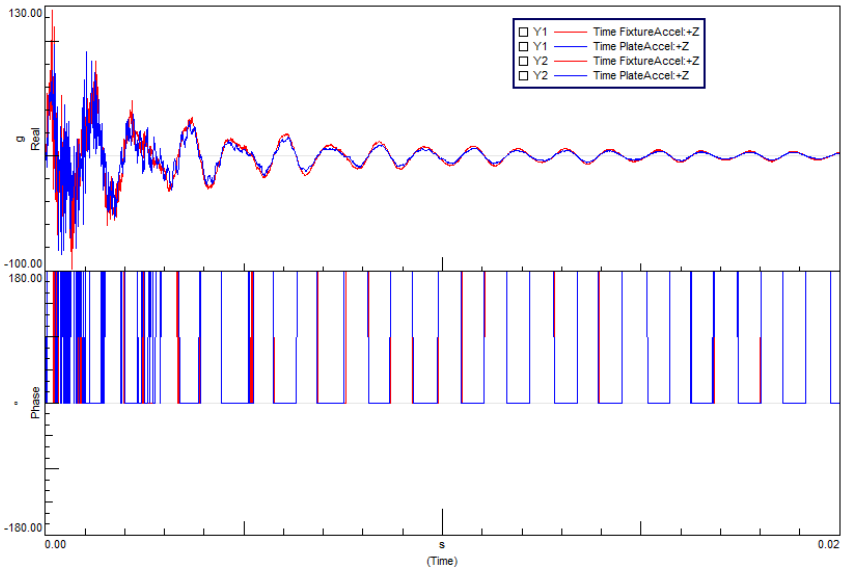

Figure 42. Time Response of 100 g Impact of Accelerometers on Fixture and Plate

There is high frequency content that makes deciding whether there is relative motion very difficult. The resonant frequency of this accelerometer is over 100 kHz, so the high frequency content isn't from the resonant frequency of the accelerometer. The phase between the two hits appears to be consistent, revealing that there is limited motion between the plate and fixture. Modes of the system will affect this, which explains the slight discrepancy, but the bolts appear to create a rigid connection. This was repeated with a sampling frequency of 20,480 Hz so the high frequency content was not captured. The phase in Figure 43 appears to track more closely.

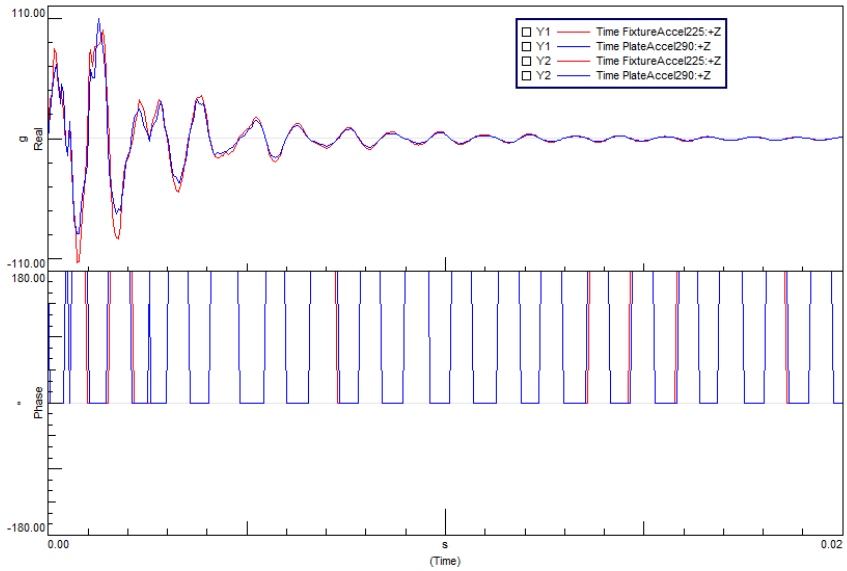

Figure 43. Time Response of 100 g Impact of Two Accelerometers with Bolts 15 ft lbs

The phase difference is hardly noticeable. The amplitude does vary slightly, which is expected because the modal participation at these locations will be different. This was repeated for bolting the impact pad on with 30 ft lbs of torque in Figure 44.

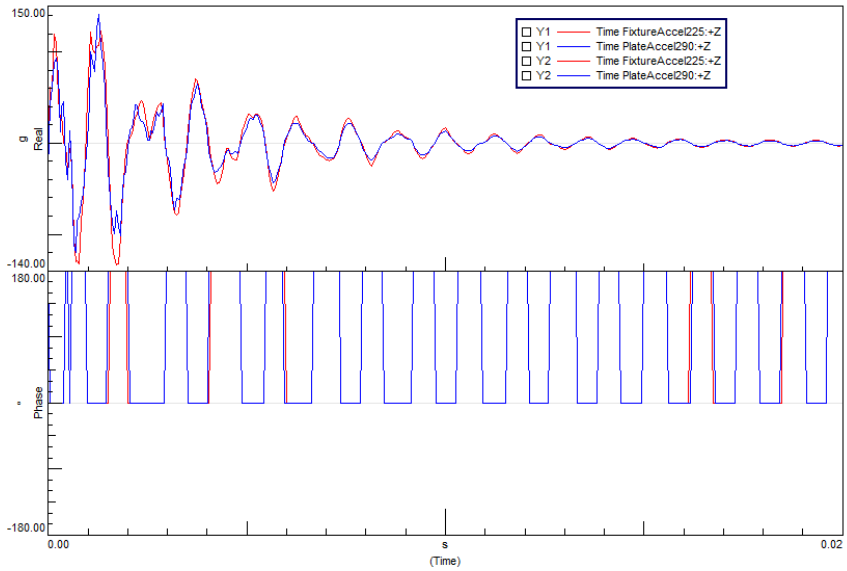

Figure 44. Time Response of 100 g Impact of Two Accelerometers with Bolts 30 ft lbs

There is no noticeable change from 15 to 30 ft lbs of bolt torque. The structure was then impacted to produce an output in the time domain of 300 g. The differences in phase increased, but not significantly, as seen in Figure 45.

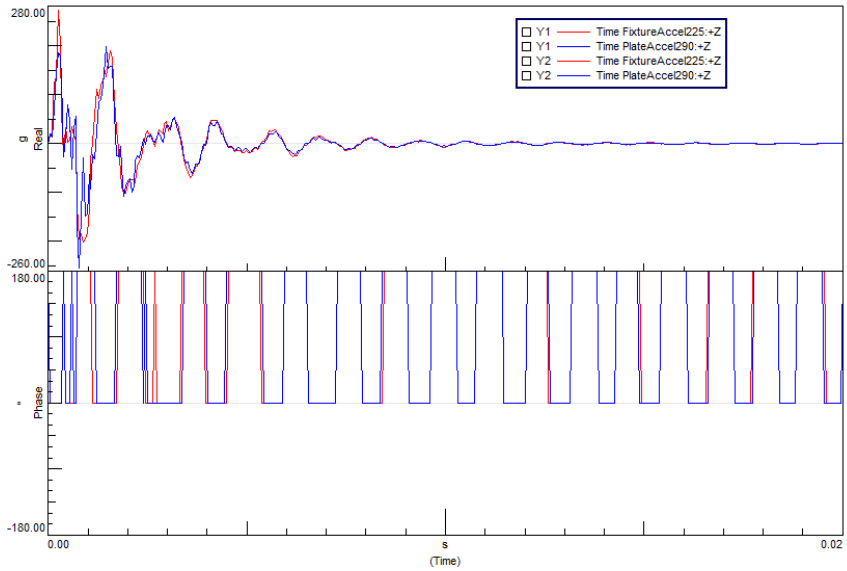

Figure 45. Time Response of 300 g Impact of Two Accelerometers with Bolts 15 ft lbs

There does not appear to be any substantial phase delay between these two points, meaning that the connection between them can be considered rigid. The modes of the system are the main, possibly only, aspect that create a difference. The eight bolts torqued to 30 ft lbs in Figure 46 also proves this.

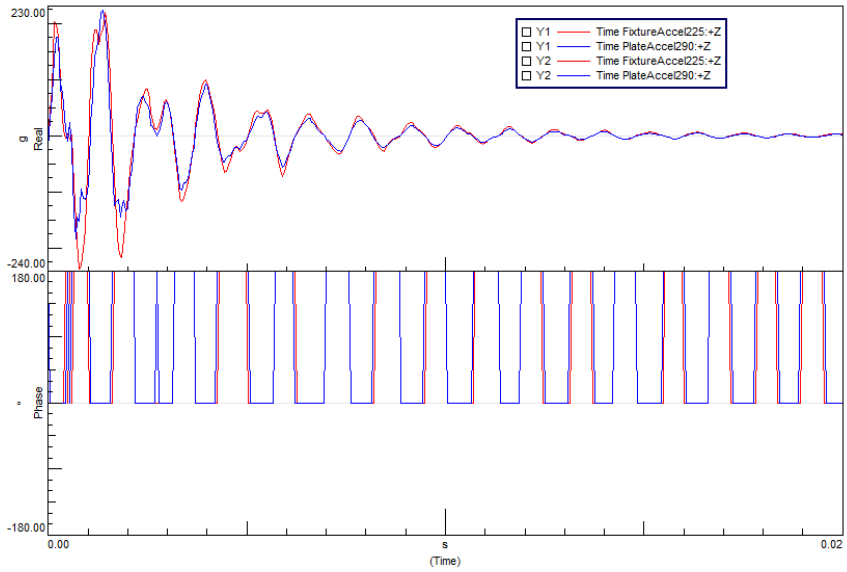

Figure 46. Time Response of 300 g Impact of Two Accelerometers with Bolts 30 ft lbs

3.3.2 Force Levels

3.3.2.1 Low Amplitude Impacts

3.3.2.1.1 Free-Free Boundary Condition

To allow for high amplitude impacts, an aluminum impact pad was included in the design of the test system. An aluminum pad of approximately 2 inches by 4 inches and 1.75 inch thick was bolted to the system. The mounted impact pad can be seen below in Figure 47.

Figure 47. Impact Pad Bolted on Resonant Plate

Although this does introduce asymmetrical geometry, the asymmetrical mass is small relative to the size of the plate set and the system SRS response remains similar.

Table 6 is a summary of the performed low amplitude tests. The plate estimated velocity is calculated by integrating the acceleration to velocity in the time domain. The value reported is the initial peak value of the velocity. [4] A force description is detailed in the table to provide a qualitative understanding of the force of the hit.

Table 6. Summary of Low Amplitude Test Runs

				Peak in Time Domain		
Boundary Conditions	**Hammer**	**Test Run**	**Force Description**	**Input (lbs)**	**Output (g)**	**Plate Estimated Velocity (ft/s)**
Free	086D20	1	Medium	1000.4	74	0.42
		2	Hard	2102.0	188	0.83
		3	Very Hard	2742.9	261	1.06
		4	Very Very Hard	5035.7	666	1.89
Constrained	086D05	5	Light	92.02	5.287	0.03
		6	Medium	465.9	27.83	0.13
		7	Hard	861.6	55.08	0.21
		8	Very Hard	1084	60.33	0.29

The response of medium, hard, very hard, and very very hard hits on the damped plates with free-free boundary conditions can be seen in the time domain on the left in Figure 48. The corresponding SRS can be seen on the right. Although only 10 to 10,000 Hz is the frequency range of interest, the SRS was calculated to 100,000 Hz for consistency and comparison with higher amplitude shock events. The sample rate of the data is only 20,480 Hz, so the curve asymptotically approaches the maximum value of the acceleration time trace. The 10,000 Hz line on the plot distinguishes the maximum frequency of the accelerometers' capabilities.

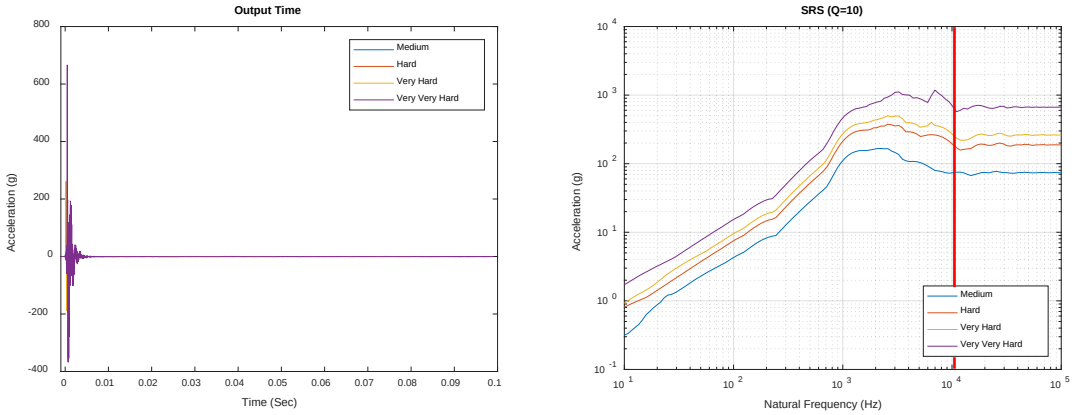

Figure 48. Varying Amplitude Inputs of Structure in Free-Free Boundary Conditions Time (Left) and SRS (Right)

The input rolloff of the aluminum tip on the force hammer and the rolloff of the low pass filter applied to the data at 10,000 Hz begins to impact the SRS near 7,000 Hz.

3.3.2.1.2 Constrained Boundary Condition

The system was then constrained by bolting a bar at the top that could pivot. The dashed lines show varying force levels taken on the constrained system and the solid lines show varying force levels on the free-free system in Figure 49. The main difference is the resonant frequency above 6000 Hz is lower in frequency while in free-free boundary conditions. This is due to the fact that there is more stiffness in a fixed condition, which drives the natural frequency up. There is also an amplitude difference because the free-free boundary condition allows the accelerometer to experience more output in acceleration for the same input force in regions where there is not a resonance present.

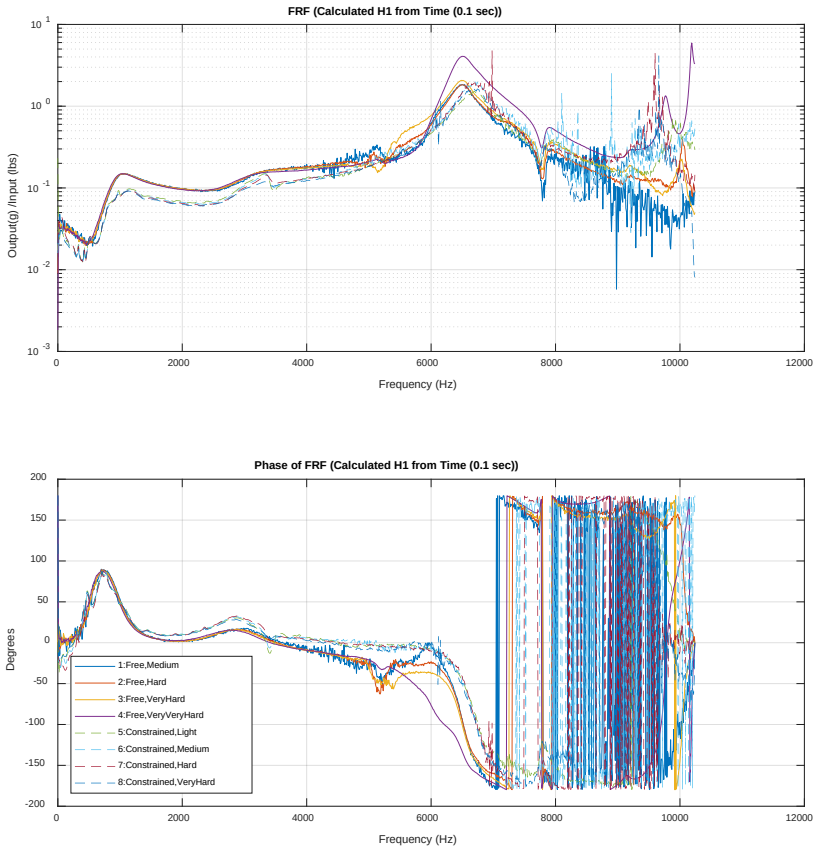

Figure 49. FRF of Varying Amplitude Inputs of Structure in Constrained (Dashed) and Free-Free (Solid)

The response of light, medium, hard, and very hard hits on the damped plates can be seen below in the time domain on the left in Figure 50. The corresponding SRS can be seen on the right. Although only 10 to 10,000 Hz is the frequency range of interest, the SRS was calculated to 100,000 Hz for consistency with higher amplitude shock events to see more of the full spectrum.

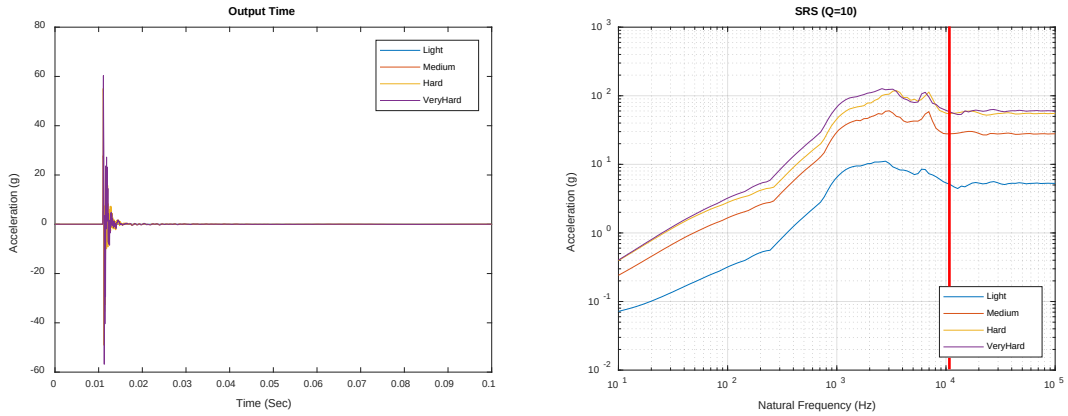

Figure 50. Varying Amplitude Inputs of Structure in Constrained Boundary Conditions Time (Left) and SRS (Right)

The input roll-off of the steel tip on the force hammer and the roll-off of the low pass filter applied to the data at 10,000 Hz begins to impact the SRS near 7,000 Hz. There is a second small peak near 6,000 Hz from the dynamics of the structure being mounted in the constrained boundary condition.

3.3.2.2 High Amplitude Shock Impacts

With the system constrained by bolting to a bar at the top that can rotate freely about an axis, the plate was impacted with high amplitude hits. The different force levels, mass, and felt programmer effects were observed. Table 7 is a summary of the high amplitude test runs included in this analysis.

Table 7. Summary of High Amplitude Shock Test Runs

Test Run	Projectile Mass	Projectile Velocity	Felt	Plate	Peak In Time Domain Output	Plate Estimated Velocity
	lbs	ft/sec	inches		g	ft/sec
1	5	19.58	0.25	C2003	5524	8.82
2	5	19.58	0.25	C2003	7296	8.88
3	10	20.69	0.25	C2003	2398	10.41
4	10	20.11	0.25	C2003	2224	9.81
5	15	20.11	0.25	C2003	2656	13.32
6	15	20.68	0.25	C2003	3723	14.31
7	20	20.68	0.25	C2003	2785	14.84
8	20	20.68	0.25	C2003	3275	15.69
9	5	50.58	0.25	C2003	20270	43.62
10	10	50.58	0.25	C2003	11260	25.55
11	10	50.57	0.25	C2003	10930	24.99
12	15	50.57	0.25	C2003	9910	22.30
13	15	50.57	0.25	C2003	8752	25.11
14	20	50.59	0.25	C2003	7249	27.10
15	20	50.57	0.25	C2003	9992	27.69
16	5	19.58	none	C2003	8567	10.21
17	5	20.11	none	C2003	8077	10.42
18	5	19.58	none	C2003	8715	10.44
19	5	19.58	none	C2003	9051	10.72
20	5	50.56	0.25	none	7944	20.44
21	5	50.57	0.25	none	7946	20.70
22	15	50.57	0.25	none	8709	24.61
23	15	50.57	0.25	none	6455	24.84

3.3.2.2.1 Variable Projectile Velocity

A projectile of 5 lbs mass at a velocity of 20 ft/s and 50 ft/s and a 0.25 inch felt programmer was used. The repeatability of each test is seen by two different tests of the same test conditions. There is an electronic filter applied at 40,000 Hz. The following Figure 51 displays the time duration of the response used to calculate the respective SRS.

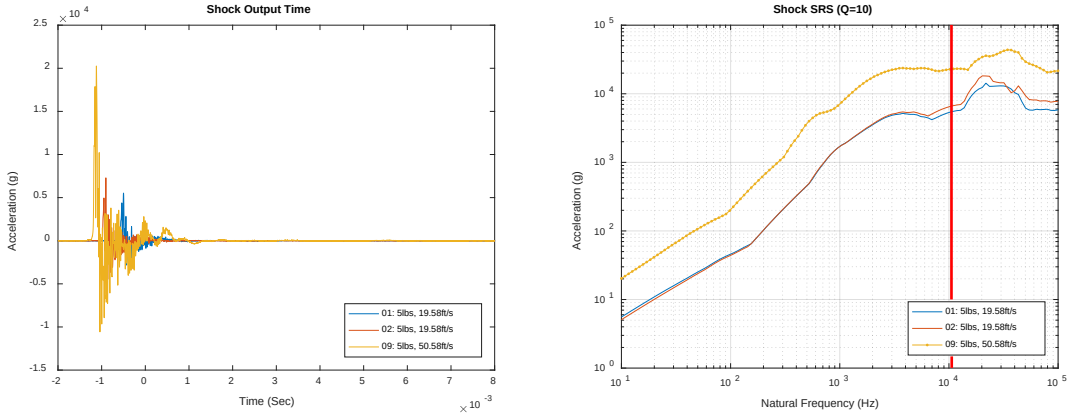

Figure 51. Time (Left) and SRS (Right) of Constant 5lbs Projectile, Variable 20 ft/s and 50 ft/s Velocity

The difference from the projectile velocity is most obvious at high frequency, which is outside the frequency range of interest, but is shown to display the complete effect of the projectile velocity. The response does appear to plateau at the peak in the time domain. The smooth initial slope indicates little to no velocity shift in the accelerometer data. [4]

A 10 lbs mass was used as a projectile at 20 ft/s and then at 50 ft/s, as seen in Figure 52. 0.25 inches of felt was used as a programmer.

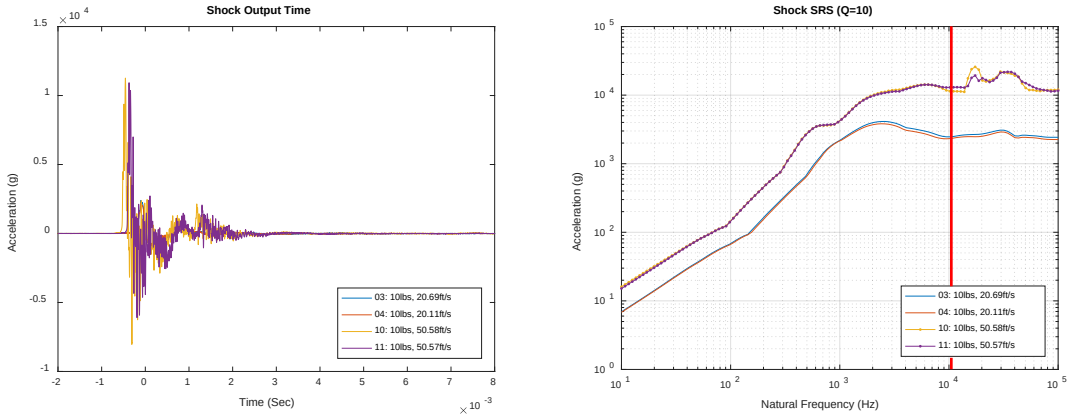

Figure 52. Time (Left) and SRS (Right) of Constant 10lbs Projectile, Variable 20 ft/s and 50 ft/s Velocity

The repeatability between the same set up conditions is acceptable. The difference from the projectile velocity is most obvious at high frequency.

A 15 lbs mass was used as a projectile at 20 ft/s and then at 50 ft/s, as seen in Figure 53. 0.25 inches of felt was used as a programmer.

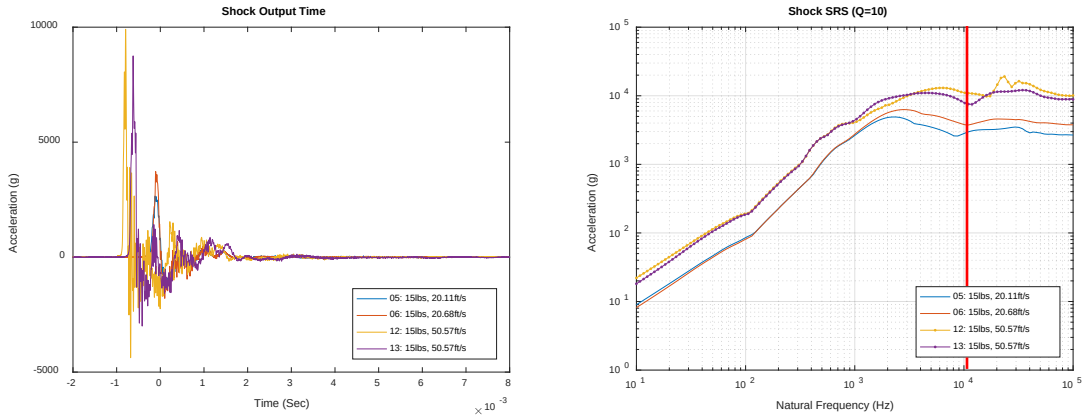

Figure 53. Time (Left) and SRS (Right) of Constant 15lbs Projectile, Variable 20 ft/s and 50 ft/s Velocity

The repeatability between the same set up conditions is reasonable. The difference from the velocity is most obvious at high frequency.

A 20 lbs mass was used as a projectile at 20 ft/s and then at 50 ft/s, as seen in Figure 54. 0.25 inches of felt was used as a programmer.

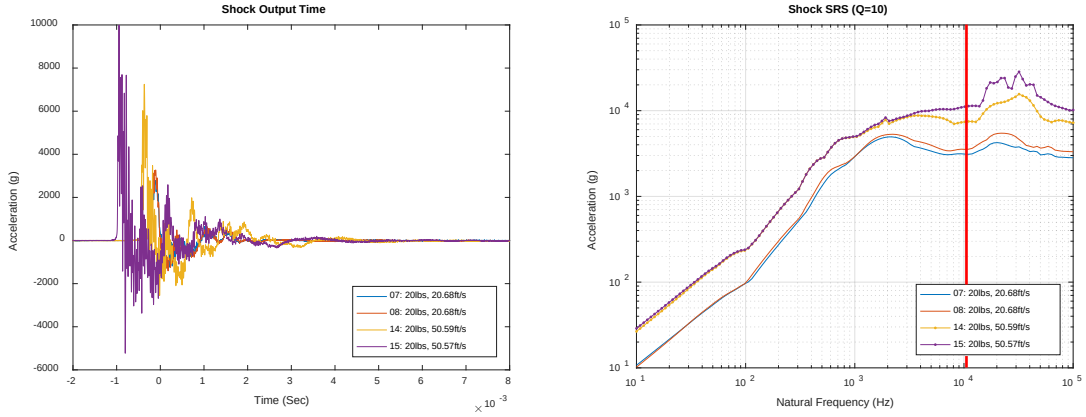

Figure 54. Time (Left) and SRS (Right) of Constant 20lbs Projectile, Variable 20 ft/s and 50 ft/s Velocity

The repeatability between the same set up conditions is also acceptable. The difference due to the velocity is most obvious at high frequency.

3.3.2.2.2 Variable Projectile Mass

Varying masses were used and compared at 20 ft/s projectile velocity in Figure 55.

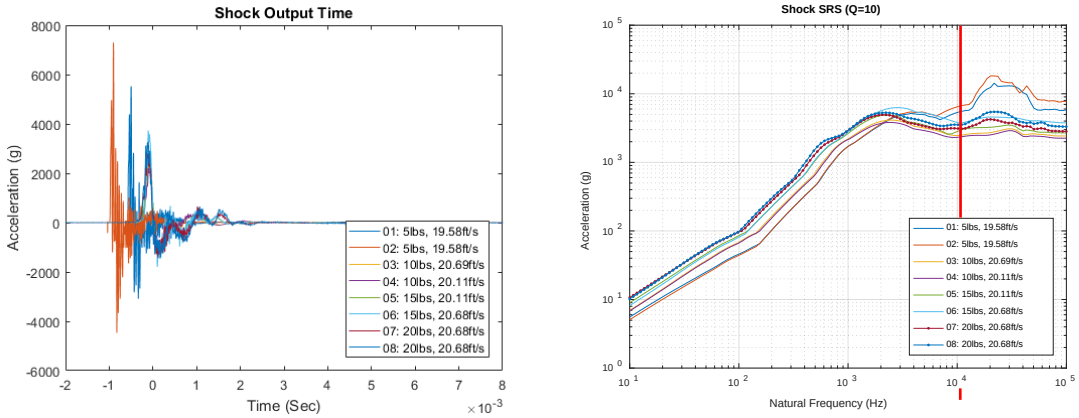

Figure 55. Time (Left) and SRS (Right) of Constant 20 ft/s Velocity, Variable 5, 10, 15, and 20 lbs Projectile

The repeatability between the same set up conditions is more difficult to decipher due to the number of traces, but is reasonable. The initial amplitude difference is obviously dependent on the kinetic energy applied to the system. As the mass increases, the SRS appears to roll off at a lower frequency.

Varying impact masses were used and compared at 50 ft/s in Figure 56.

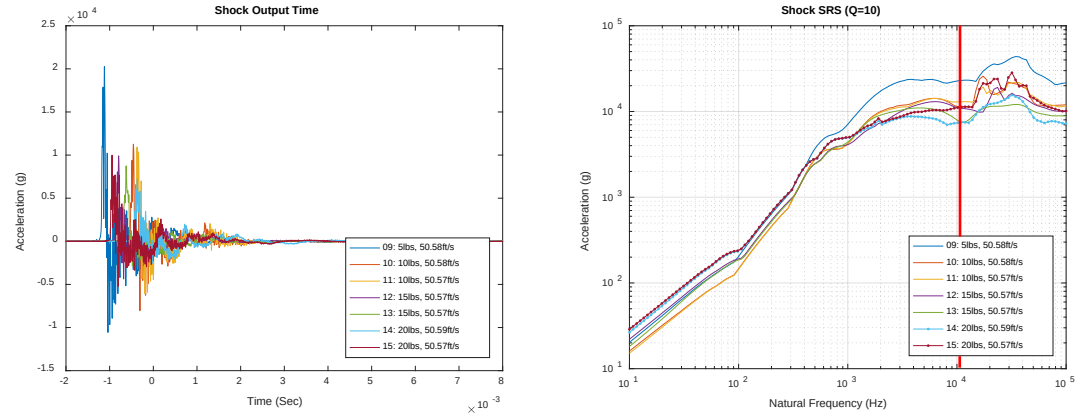

Figure 56. Time (Left) and SRS (Right) of Constant 50 ft/s Velocity, Variable 5, 10, 15, and 20 lbs Projectile

The repeatability between the same test conditions was observed. The initial amplitude difference is obviously dependent on the kinetic energy applied to the system. Test run 9 is clearly an outlier. The larger impact masses again appear to roll off at a lower frequency.

3.3.2.2.3 Variable Felt

Four test runs without felt and two test runs with felt all with a projectile mass of 5 lbs and projectile velocity of 20 ft/s were compared in Figure 57.

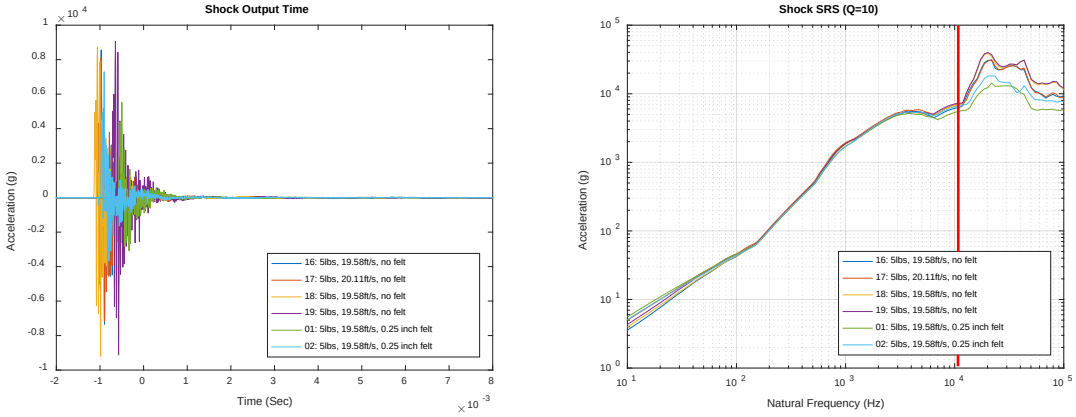

Figure 57. Time (Left) and SRS (Right) of Constant 20 ft/s Velocity and 5 lbs Projectile, Variable 0.25 Inch Felt

The test is consistently repeatable. A noticeable difference is seen above the frequency range of interest. The felt increases the duration of the force pulse, which reduces the response at frequencies above 10,000 Hz more than without felt, but has little impact elsewhere.

3.3.2.2.4 Variable Projectile Mass on Undamped Plate

5 lbs and 15 lbs masses were used and compared at 50 ft/s on the plate with no damping material in Figure 58.

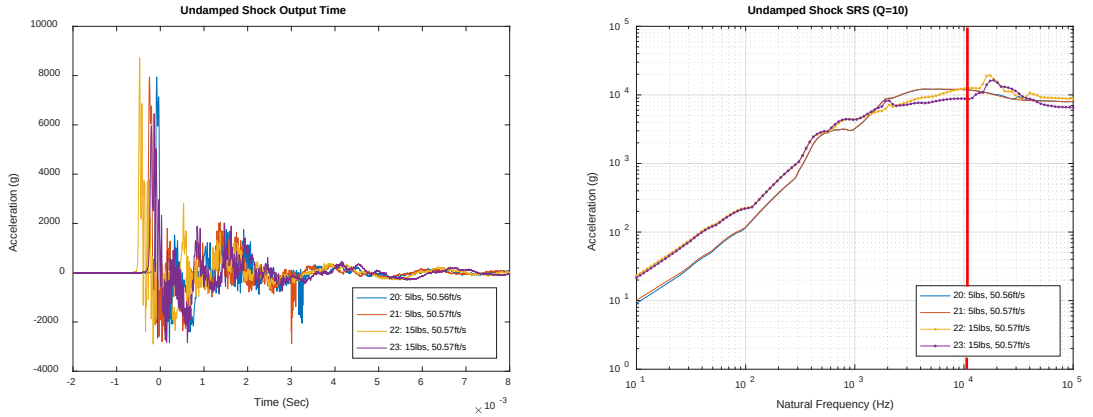

Figure 58. Time (Left) and SRS (Right) of Constant 50 ft/s Velocity, Variable 5 and 15 lbs Projectile on Undamped Plate

The knee frequency is much less distinguishable, but repeatability between test runs is still acceptable. The characteristic higher initial amplitude of the curve from the larger projectile is apparent.

3.3.3 SRS Intricacies

3.3.3.1 SRS Contributors

The SRS can be calculated many different ways. As previously discussed, maximax is typically used. The positive and negative primary and residual responses can also be calculated. As previously stated, maximax is defined as the maximum of both positive and negative primary and residual responses. The maximum positive and negative SRS and the maximax can be seen in Figure 59.

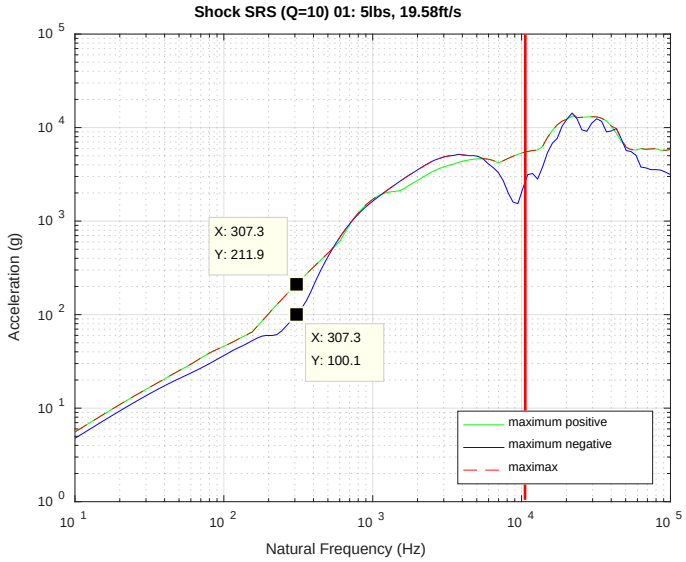

Figure 59. Maximum Positive and Negative and Maximax SRS of 20 ft/s Velocity, 5 lbs Projectile

Overall, the maximum of the positive and negative appear relatively close, which is an indication of measuring good data and minimal accelerometer saturation. [4] The positive maximum is the main contributor to the maximax. But there are some differences that can be attributed to the positive direction experiencing a plate velocity change substantially higher than the negative direction. Using the following Equation 2, the velocity can be estimated from the SRS at 300 Hz, which is a location on the SRS where this difference is large. [4]

$$velocity = \frac{acceleration}{2\pi f} \tag{2}$$

At 307.3 Hz, 211.9 g of acceleration on the positive side is calculated to be 3.53 ft/sec and 100.1 g of acceleration on the negative side is 1.67 ft/sec. These are both relatively low values, so it is difficult to say this difference is alarming.

A SRS of two test runs with the same test configuration are compared below in Figure 60. The primary response of the shock event is the maximum responses during the excitation event and the residual is the peak response after the excitation has decayed. [13]

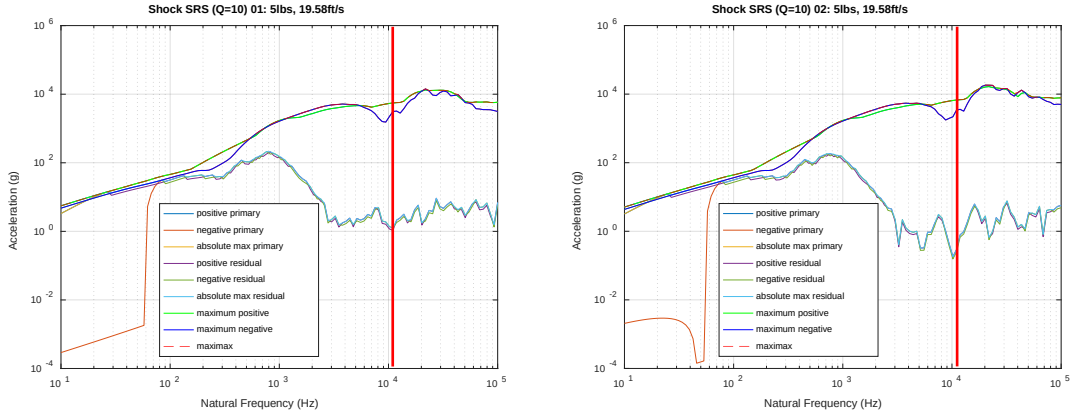

Figure 60. SRS Calculations of 20 ft/s Velocity, 5 lbs Projectile from Two Test Runs

The primary response is the main contributor. The residual never drives the maximax and is consistently low, which is also a sign of useful data because that verifies that the event fully decays.

For the same projectile mass, but higher velocity (50 ft/s), similar trends were observed in Figure 61.

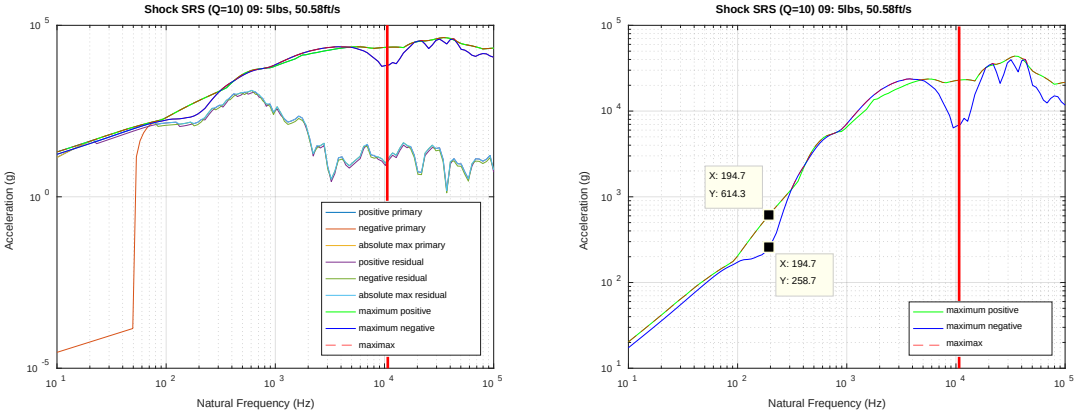

Figure 61. SRS Calculations of 50 ft/s Velocity, 5 lbs Projectile

Using the velocity estimation method at 194.7 Hz, 614.3 g of acceleration on the positive side is a calculated 16.16 ft/sec and 258.7 g of acceleration on the negative side is 6.80 ft/sec. This is a significant difference, but only over a small region of the SRS.

These methods of calculating the SRS indicate reasonably good data with minimal overstressing of elements, physical movement of sensor parts, cable noise, base strain

induced errors, inadequate low-frequency response, or overloading of the signal conditioner. [4]

3.3.3.2 Velocity Shift

Velocity present in acceleration time data can severely alter low frequency components of the SRS. [15] Blough developed a seamless method to combat this. [16] This method is further investigated. A flow chart of this method is seen below in Figure 62.

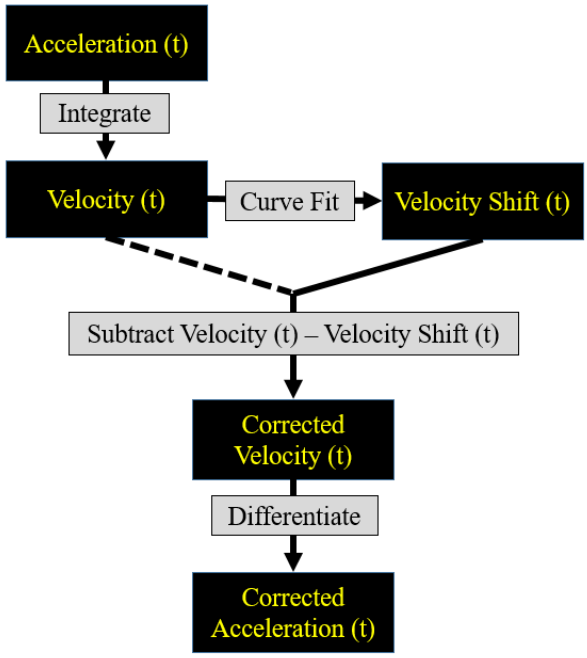

Figure 62. Overview of Velocity Correction Method

To solve this error in data, the velocity can be corrected for. An acceleration time trace and the resulting SRS can be seen in Figure 63. The g unit was converted to ft/sec^2.

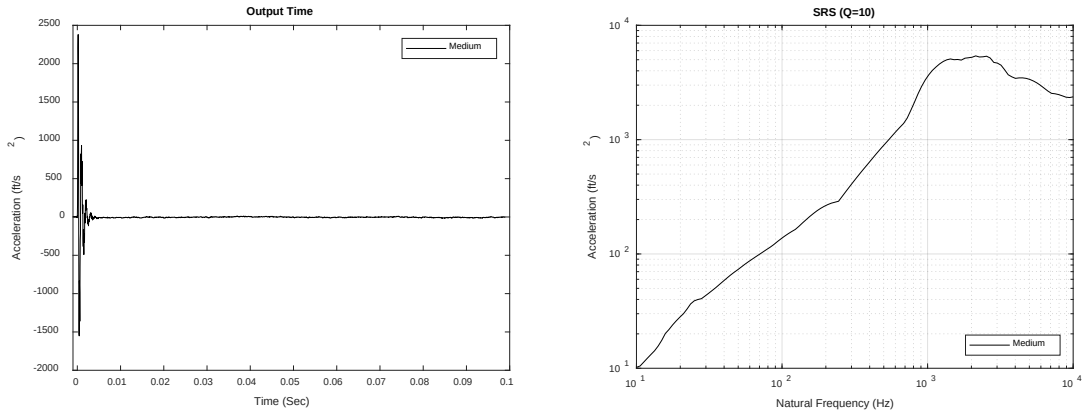

Figure 63. Medium Free-Free Time (Left) and SRS (Right)

It is clear from the SRS that the low frequency is not consistent with expectations. To eliminate this artifact, the acceleration time trace was integrated. Once integrated, this can be curve fit with a low order polynomial. In this case, a simple third degree polynomial is used. Subtracting the original velocity trace from this curve fit will "zero" the velocity trace. This process can be seen in the following Figure 64.

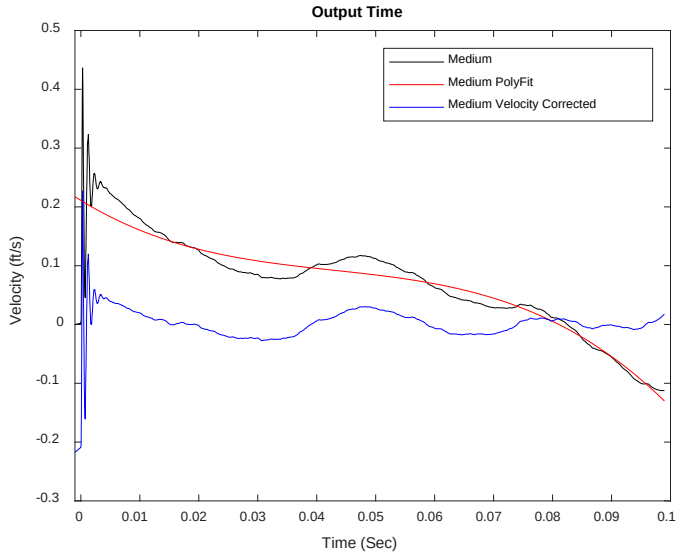

Figure 64. Medium Free-Free Velocity Correction Process

Although the time trace is not perfectly fit and doesn't completely reach zero after the impulse, the majority of the velocity is corrected for. This corrected velocity time trace can then be differentiated to find the corrected acceleration in Figure 65.

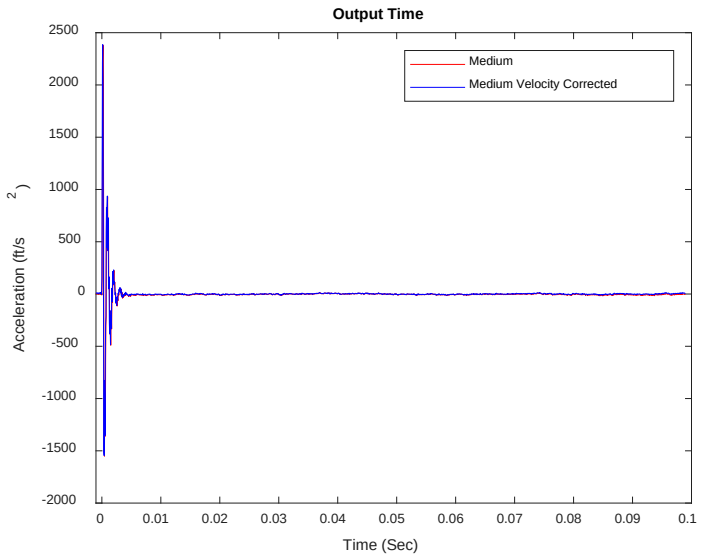

Figure 65. Medium Free-Free Original and Corrected Acceleration Time Response

This acceleration time trace can be used to calculate the SRS, as seen in Figure 66.

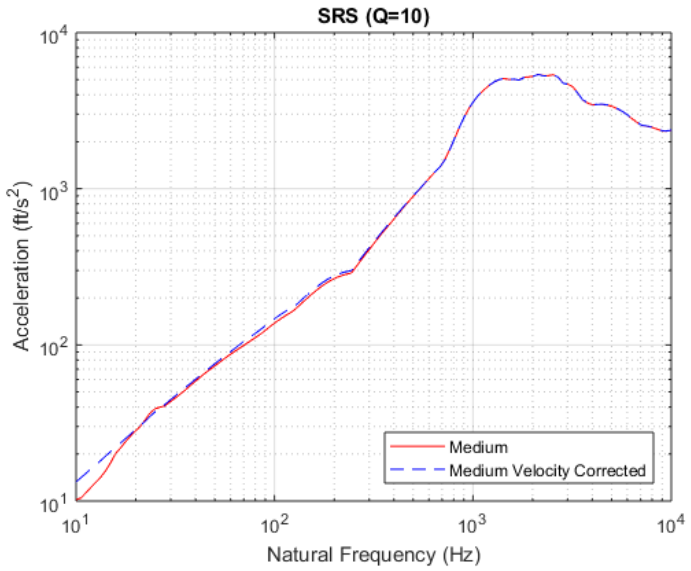

Figure 66. Medium Free-Free Original and Velocity Corrected SRS

The low frequency variation in the original data is now a smooth curve. This is much more accurate of the acceleration the part is actually experiencing. Even a coarse linear fit can solve a majority of the problem, as seen in the following Figure 67.

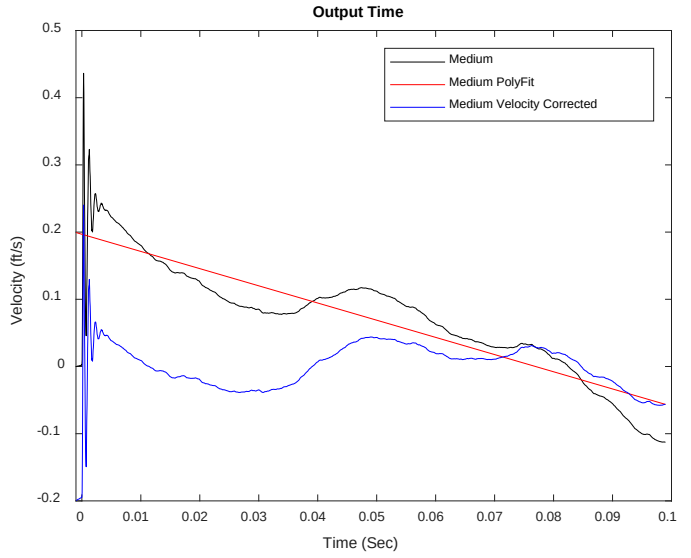

Figure 67. Medium Free-Free Velocity Correction Process and SRS

This rough linear fit still eliminates a large portion of the velocity error. The resulting SRS is seen below in Figure 68.

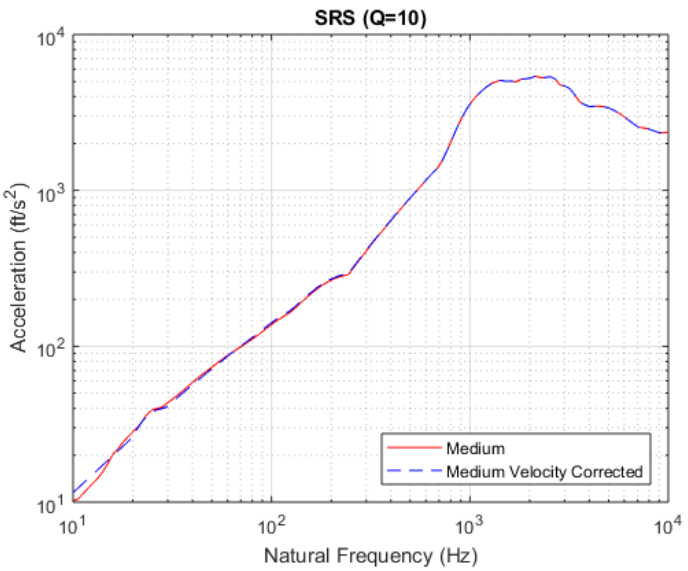

Figure 68. Medium Free-Free Original and Velocity Corrected SRS

This proves that a complex algorithm is not necessary for this correction. It is straightforward and easy to implement. This is also a testament to how sensitive the low frequencies are to velocity error.

3.4 Input Estimation

The method to use a FRF from one test run to estimate the input of another test run is performed and investigated. The method is first validated using a variety lower impact tests where the input is known. An IFFT of the input spectrum reveals a recreation of the measured input time. High amplitude shocks input spectrums are then estimated using a lower amplitude FRF. The IFFT of these spectrums provide valuable insight.

3.4.1 Validation

To find the accuracy of the method, an impact test using a modal impact hammer was done for a low amplitude hit on the test set up. A second impact test was performed at a higher amplitude. The input was known for both hits. Using the lower amplitude FRF, the higher amplitude input can be estimated and compared to the measured higher amplitude input. This low amplitude verification was done using three systems. Table 8 below describes the test runs of each system. For the first four test runs, the structure was bolted to a bar that can swing, here called the constrained boundary condition. The PCB D05 impact hammer had a steel tip. More weight was added to the hammer in test run 4 to provide a harder hit. Test runs 5-9 were done with a free-free boundary condition using bungee straps to hang the plate. A PCB 086D20 hand sledge hammer with an aluminum tip was used. Test runs 10-14 were also in the free-free environment, but a lighter PCB 086B03 hammer with a steel tip was used to impact the structure.

Table 8. Summary of Low Amplitude Testing

				Peak in Time Domain	
Boundary Conditions	**Hammer**	**Test Run**	**Force Description**	**Input (lbs)**	**Output (g)**
Constrained	086D05	1	Light	92.02	5.287
		2	Medium	465.9	27.83
		3	Hard	861.6	55.08
		4	Very Hard	1084	60.33
Free	086D20	5	Light	374.8	28
		6	Medium	1000.4	74
		7	Hard	2102.0	188
		8	Very Hard	2742.9	261
		9	Very Very Hard	5035.7	666
	086B03	10	Light	45.4	6.5
		11	Medium	157.8	28
		12	Hard	392.5	81
		13	Very Hard	552.6	136
		14	Very Very Hard	817.9	180

The constrained system tests' FRFs from test runs 1-4 in Figure 69 show reasonable repeatability between the different inputs.

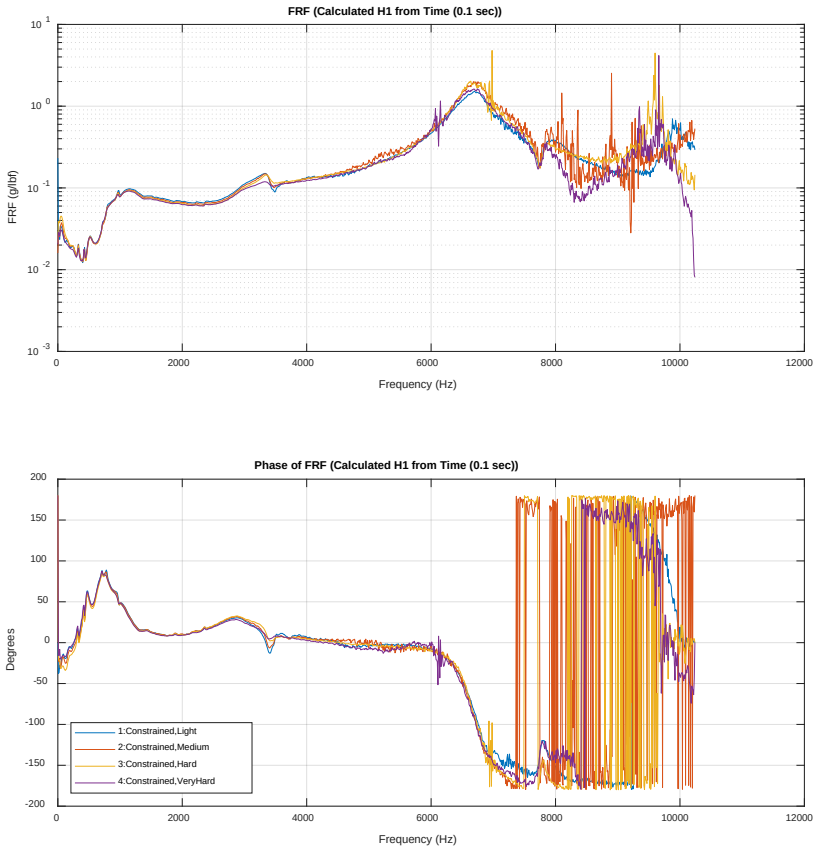

Figure 69. FRF of Constrained Test Runs

The input for each run was estimated using the lightest input force (Test Run 1) in Figure 70 because it had the least amount of noise.

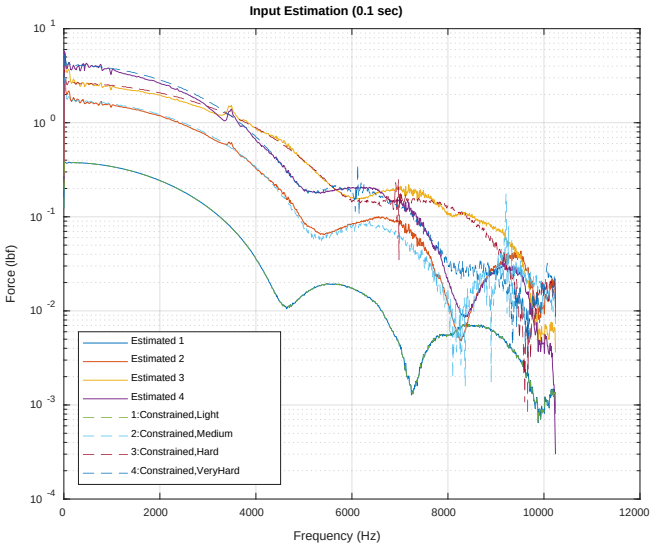

Figure 70. Measured Input Spectrums of Constrained System and Estimated Using Light FRF

The approximate shape and amplitude of the input was estimated and matches the actual measured inputs.

The FRFs of the constrained system (Tests 1-4) are seen as dashed lines and the FRFs from the free-free system with the 086D20 hammer (Tests 5-9) can be seen as solid lines in Figure 71. Nonlinearities are excited at the higher amplitude impacts.

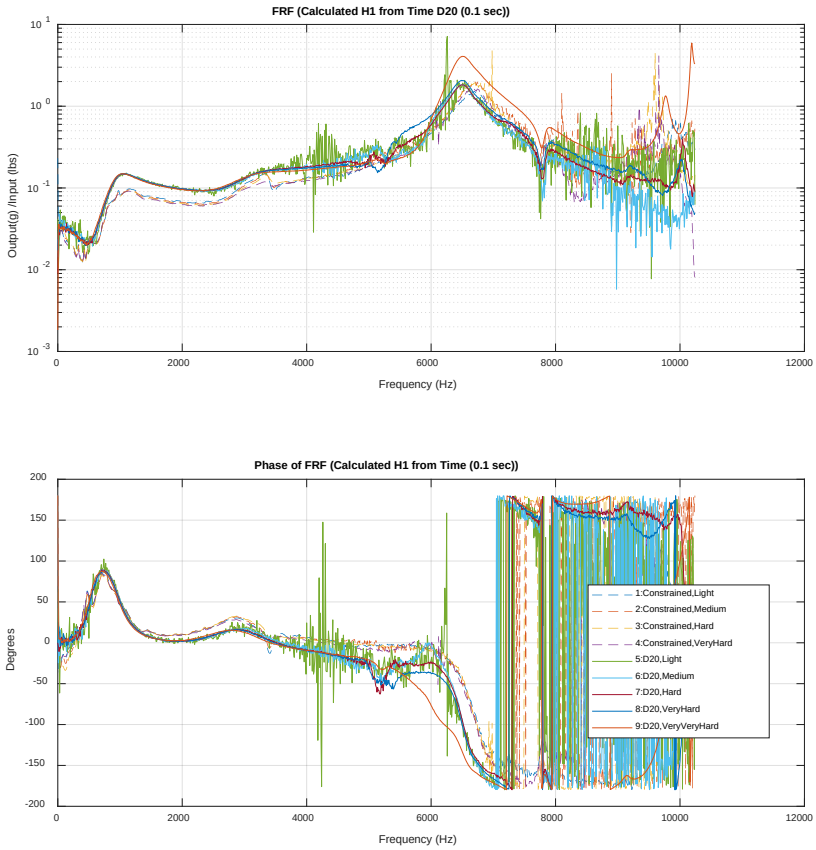

Figure 71. FRF of Constrained and Free Test Runs Using 086D20 Hammer

Because the system was rigidly attached to a bar, the effective mass in the structure was greater. This means the system has a lower output for a given input with the constrained boundary conditions.

The input for each run was estimated using the lightest input force (Test Run 5), medium input force (Test Run 6), and hard input force (Test Run 7) in Figure 72.

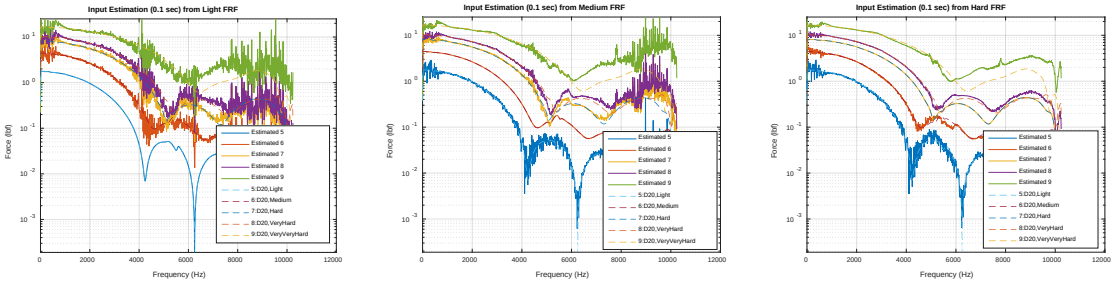

Figure 72. Measured Input Spectrums of Free 086D20 Hammer Test Runs and Estimated Input Spectrums Using Light FRF (left), Medium FRF (middle), and Hard FRF (right)

The less noise on the FRF, the closer the estimated input matches the measured input.

The FRFs of the constrained system (Tests 1-4) are seen as dashed lines and the FRFs from the free-free system with the lighter 086B03 hammer (Tests 10-14) can be seen as solid lines in Figure 73. Significant noise is apparent on the free-free low amplitude hits.

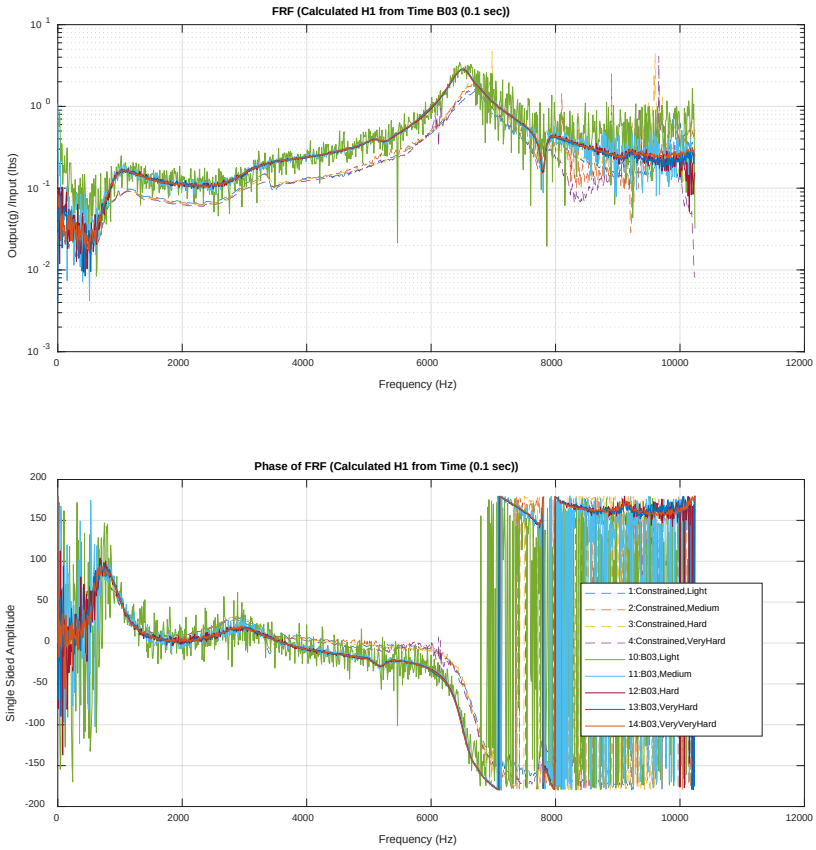

Figure 73. FRF of Constrained and Free Test Runs Using 086B03 Hammer

The input for each run was estimated using the medium input force (Test Run 11) in Figure 74.

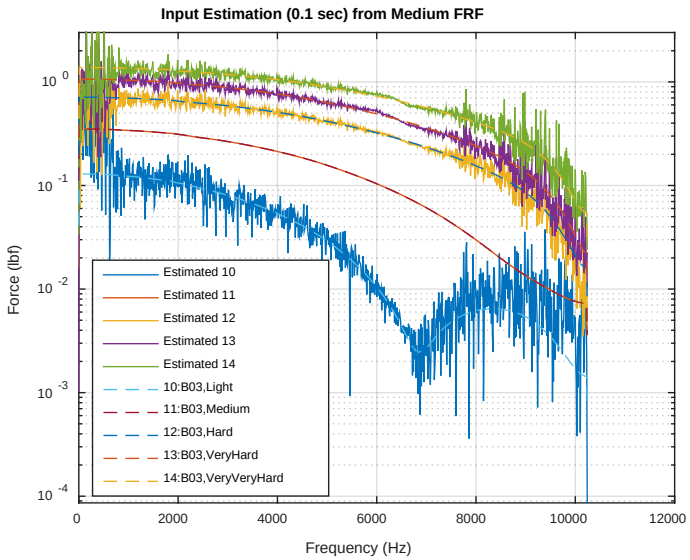

Figure 74. Measured Input Spectrums of Free-Free System and Estimated Using Medium FRF

The estimated input extended farther in the frequency range. This is expected because the hammer is lighter and a harder hammer tip was used. Using spectral averaged FRF's, the system was tested for a variety of input levels and hammer tips. This minimizes the noise on the resulting estimated inputs, resulting in a more accurate representation of the input curve.

To complete the process of validation, these input estimates were then scaled appropriately before taking an IFFT (inverse fast fourier transform). The IFFT of the original actual input spectrum matched the original time data perfectly, validating this process. The IFFT of the test run 7 estimated using the FRF from test run 6 is nearly identical to the IFFT of the original actual test run 7 input spectrum, as seen in the following Figure 75.

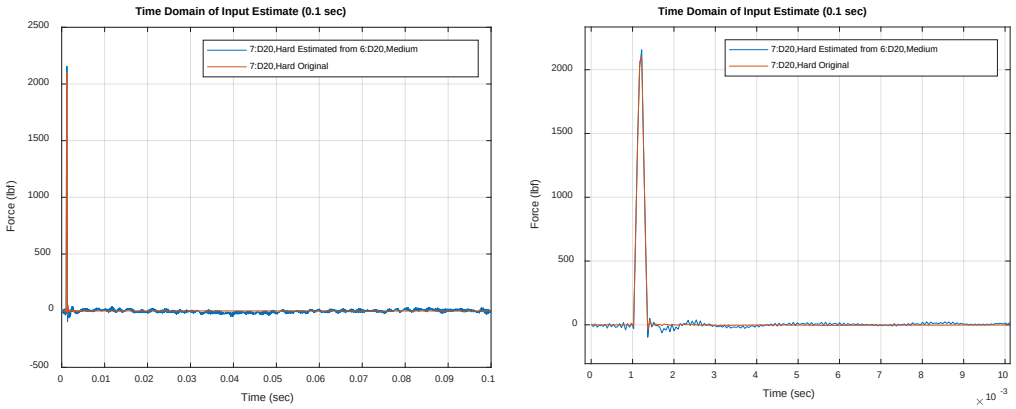

Figure 75. IFFT of Original and Estimated Low Amplitude Spectrums of Free-Free System

The same process was repeated for the constrained system. The IFFT of test run 1 estimated using test run 3 of the constrained system and the IFFT of the original input spectrum appear to be almost identical in Figure 76.

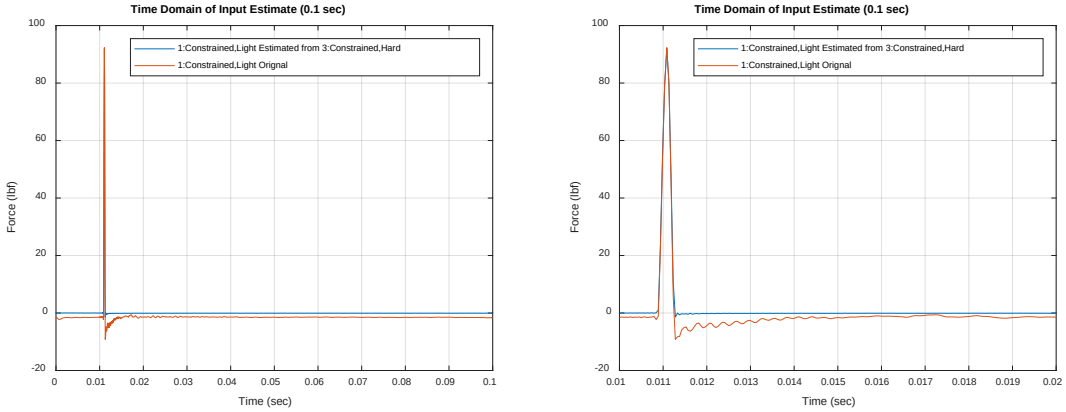

Figure 76. IFFT of Original and Estimated Low Amplitude Spectrums of Constrained System

Differences from noise are apparent, but this fully validates this process at low amplitudes.

3.4.2 Estimation of Shock Inputs

3.4.2.1 Frequency Domain Input Estimation

High impact shock inputs were then tested on the constrained system, as seen in Table 9. Although these inputs are not known, these tests can verify the method by monitoring expected trends. Three variables were changed. The projectile mass was 5, 10, 15, or 20 lbs. The velocity was 20 ft/sec or 50 ft/sec. A 0.25 inch thick felt programmer could also be placed on the impact location. Knowing the mass and velocity, the kinetic energy input into the system can be calculated for each run. A RMS value of the estimated input reveals the trends by giving a level of total estimated spectral energy. Although not directly comparable, these two values should show similar trends.

Table 9. Summary of High Amplitude Testing

Test Run	Projectile Mass	Velocity	Felt	Kinetic Energy $(1/2)*m*v^2$	Estimated Input RMS
	lbs	ft/sec	inches	lbf*ft	lbf
1	5	19.58	0.25	958	55.1
2	5	19.58	0.25	958	56.8
3	10	20.69	0.25	2140	74.5
4	10	20.11	0.25	2022	69.2
5	15	20.11	0.25	3033	105.5
6	15	20.68	0.25	3207	112.3
7	20	20.68	0.25	4277	125.5
8	20	20.68	0.25	4277	143.3
9	5	50.58	0.25	6396	364.2
10	10	50.58	0.25	12792	253.3
11	10	50.57	0.25	12787	249.8
12	15	50.57	0.25	19180	229.1
13	15	50.57	0.25	19180	235.7
14	20	50.59	0.25	25593	286.2
15	20	50.57	0.25	25573	282
16	5	19.58	none	958	57.6
17	5	20.11	none	1011	60.3
18	5	19.58	none	958	54.7
19	5	19.58	none	958	56.4
20	5	50.56	0.25	6391	57.6
21	5	50.57	0.25	6393	60.3
22	15	50.57	0.25	19180	54.7
23	15	50.57	0.25	19180	56.4

The light FRF of the constrained system is used to estimate the input of all of the shock test datasets. The effect of different force levels was monitored as velocity of the projectile (20 and 50 ft/sec). Figure 77 displays the SRS from using a 5 lbs projectile to impact the structure at 20 and 50 ft/sec.

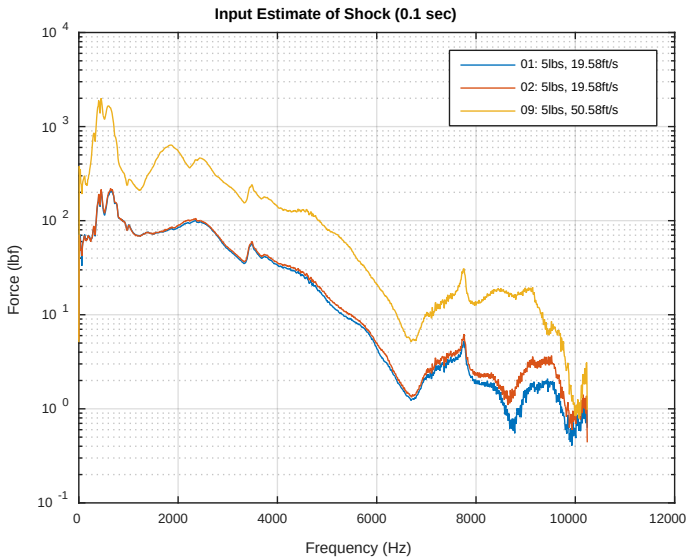

Figure 77. Estimated Input Spectrums, Constant 5lbs Projectile, Variable 20 ft/s and 50 ft/s Velocity

This is a typical shape of an input spectrum and the inputs appear to increase with higher projectile velocity. Using a 10 lbs projectile, the structure was impacted at 20 and 50 ft/sec, as seen in Figure 78.

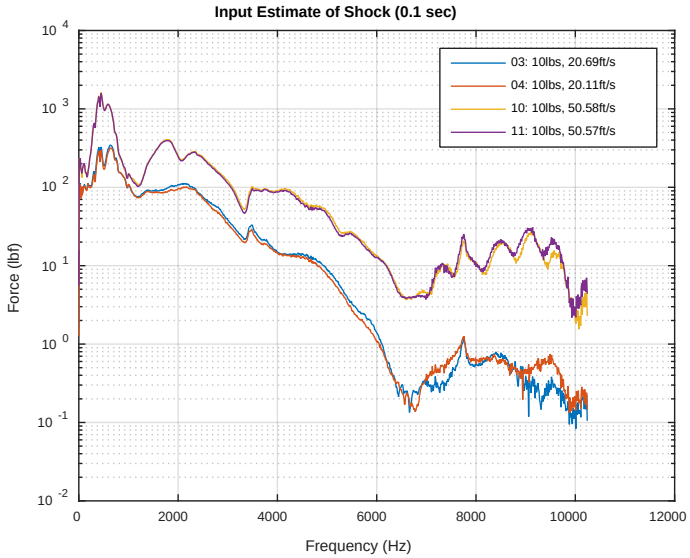

Figure 78. Estimated Input Spectrums, Constant 10lbs Projectile, Variable 20 ft/s and 50 ft/s Velocity

A similar trend of increasing amplitude for higher projectile velocity was observed. Using a 15 lbs projectile, the structure was impacted at 20 and 50 ft/sec, seen in Figure 79.

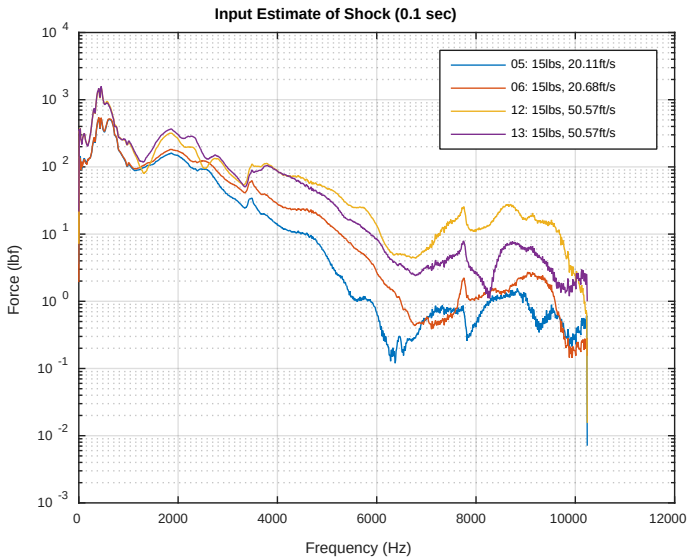

Figure 79. Estimated Input Spectrums, Constant 15lbs Projectile, Variable 20 ft/s and 50 ft/s Velocity

The inputs from a projectile mass of 15 lbs are not as repeatable, but the same increase in amplitude with increase in projectile velocity can be observed. Using a 20 lbs projectile, the structure was impacted at 20 and 50 ft/sec, as seen in Figure 80.

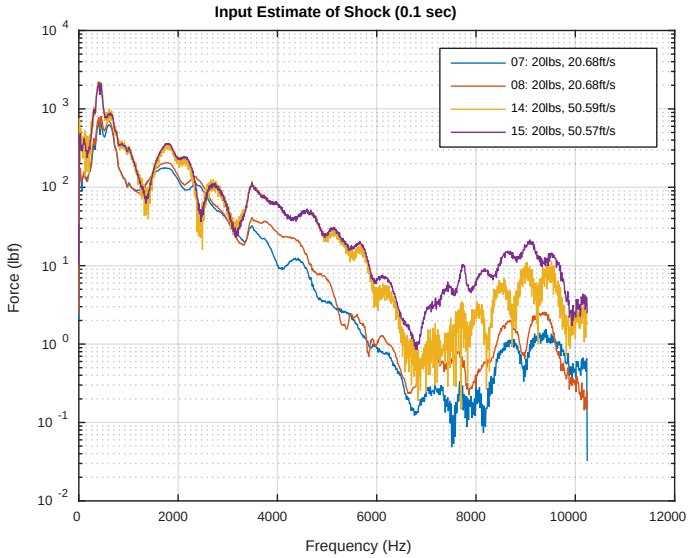

Figure 80. Estimated Input Spectrums, Constant 20lbs Projectile, Variable 20 ft/s and 50 ft/s Velocity

The high amplitude shock events begin to have a ripple in the input spectrum, especially test run 14. This is characteristic of a double hit.

The projectile velocity clearly has a large impact on the shape of the input, particularly the amplitude. The harder impacts consistently have a higher amplitude and excite further in the frequency spectrum, as expected.

The effect of projectile mass was investigated by using a constant velocity and comparing the 5, 10, 15, and 20 lbs masses. Impacting the structure at 20 ft/sec, a 5, 10, 15, and 20 lbs mass was used in Figure 81.

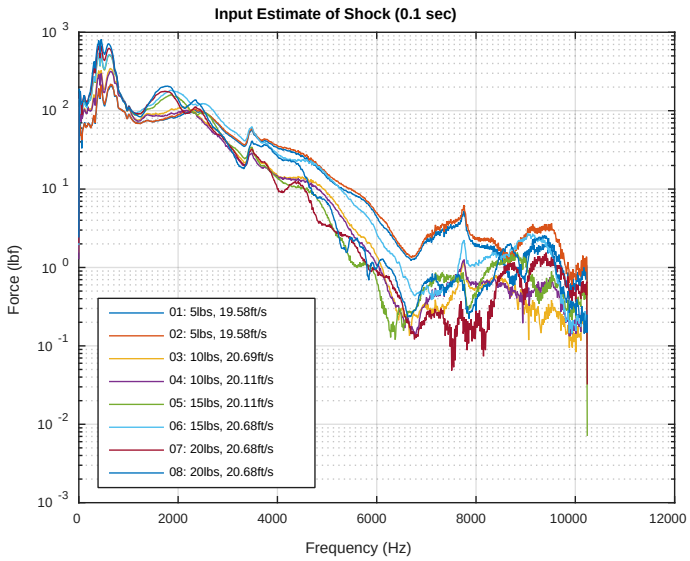

Figure 81. Estimated Input Spectrums, Constant 20 ft/s Velocity, Variable 5, 10, 15, and 20 lbs Projectile

For low velocity, the higher mass projectiles appear to have higher amplitude and excite more of the frequency spectrum. Viewing the summary Table 9 for these estimated inputs, it is apparent that the RMS value increases relatively linearly with the kinetic energy input into the system.

Impacting the structure at 50 ft/sec, a 5, 10, 15, and 20 lbs mass was used in Figure 82.

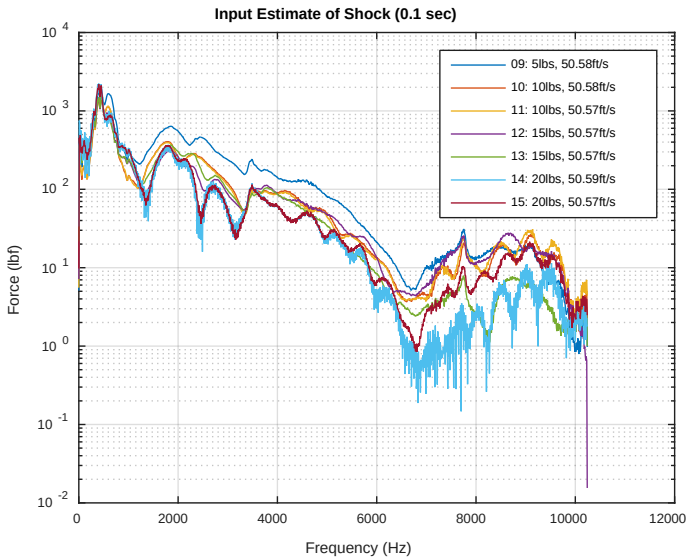

Figure 82. Estimated Input Spectrums, Constant 50 ft/s Velocity, Variable 5, 10, 15, and 20 lbs Projectile

For high velocity, more of the frequency spectrum is excited by lighter projectiles. Looking at the summary Table 9 for these estimated inputs, the RMS value does not increase linearly with an increase of the kinetic energy input into the system. The highest RMS is the 5 lbs projectile followed by 20 lbs, 10 lbs, and 15 lbs. A possible reason for this discrepancy is the higher frequencies have more energy content using the light projectile, increasing the energy present in the spectrum. The higher projectile mass should still input more energy in the system.

The difference in having a felt programmer was then tested. 0.25 inches of felt was placed on the input location to increase the impact time. In Figure 83, the first four curves do not have felt and the last two curves have 0.25 inches of felt at the impact location. A 5 lbs mass at 20 ft/sec was tested.

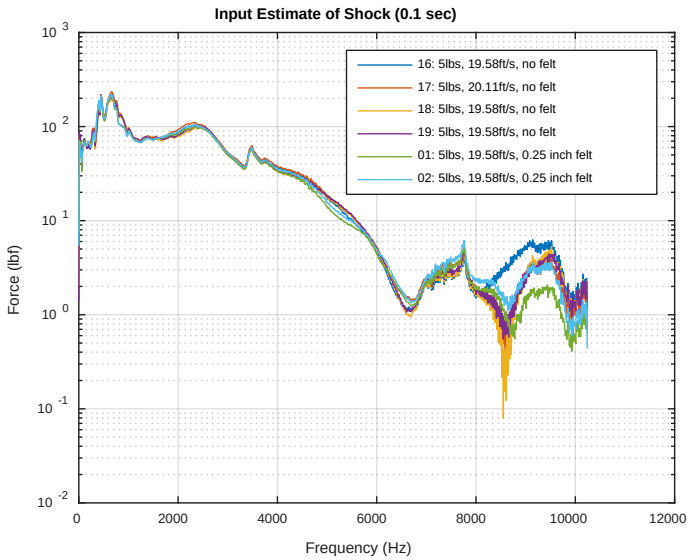

Figure 83. Estimated Input Spectrums, Constant 20 ft/s Velocity and 5 lbs Projectile, Variable 0.25 inch Felt

The difference in the felt is not noticeable. Even though this is the lightest projectile and the lowest projectile velocity, the projectile is heavy enough and the velocity high enough that the felt does not appear to have a noticeable difference on the input spectrum.

3.4.2.2 Time Domain Input Estimation

The IFFT process that was validated at lower amplitudes was performed for the shock test run 16, as seen in Figure 84.

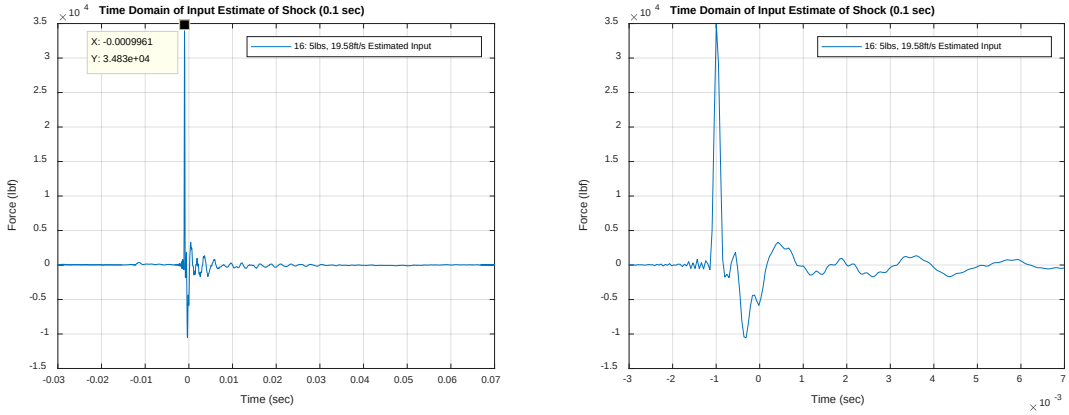

Figure 84. IFFT of Estimated Shock Input Spectrum 5 lbs, 20 ft/s

The output has a clear initial impulse. One notable artifact is a small excitation roughly 10 milliseconds before the large impact. The large impulse does appear to be on the same magnitude of what should be expected. The maximum time domain of the output is 8567 g and the maximum time domain of the input force is 34,800 lbf, a difference that is on the

same relative order as the lower amplitude differences. The input appears to decay within the measured time.

This IFFT process was performed on six other estimated inputs. The input spectrum of a 5 lbs projectile and 20 ft/sec test run can be seen below in Figure 85.

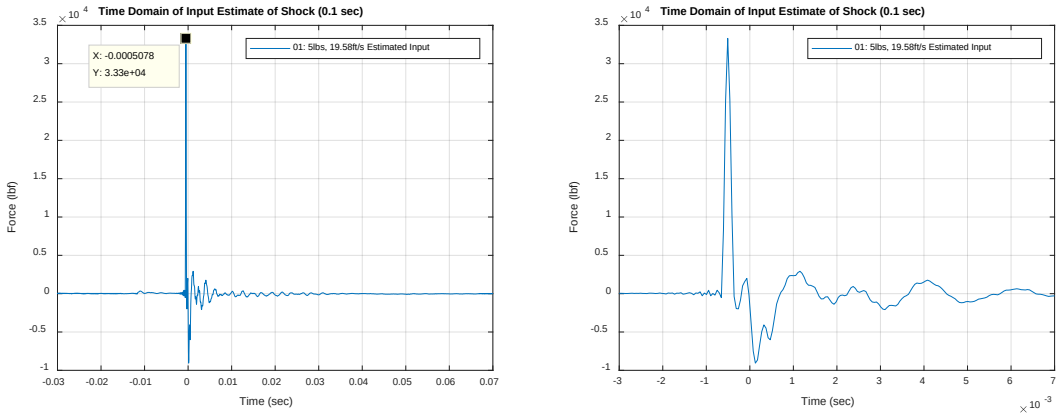

Figure 85. IFFT of Estimated Shock Input Spectrum 5 lbs, 20 ft/s

The maximum time domain of the input force is 33,300 lbf. An IFFT of test run 2 (the same test conditions as test run 1) was performed in Figure 86.

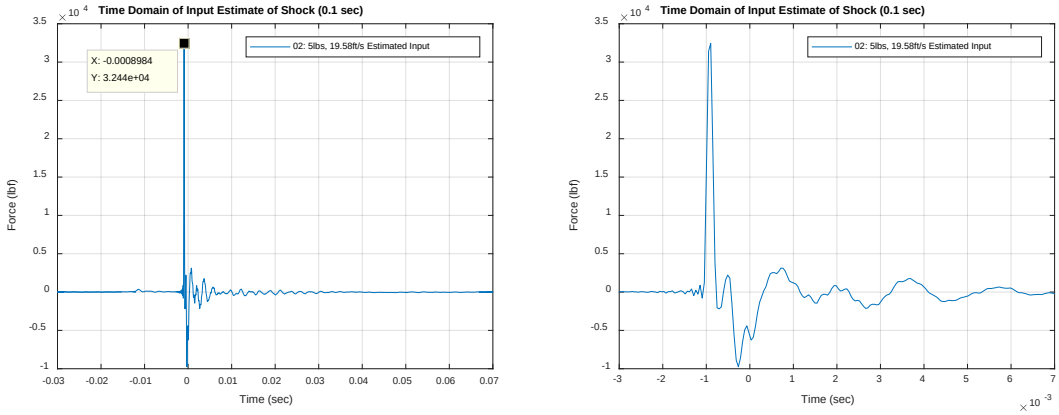

Figure 86. IFFT of Estimated Shock Input Spectrum 5 lbs, 20 ft/s

The maximum time domain of the input force is 32,440 lbf. This process was also repeated for test run 7 with a 20 lbs projectile at 20 ft/sec in Figure 87.

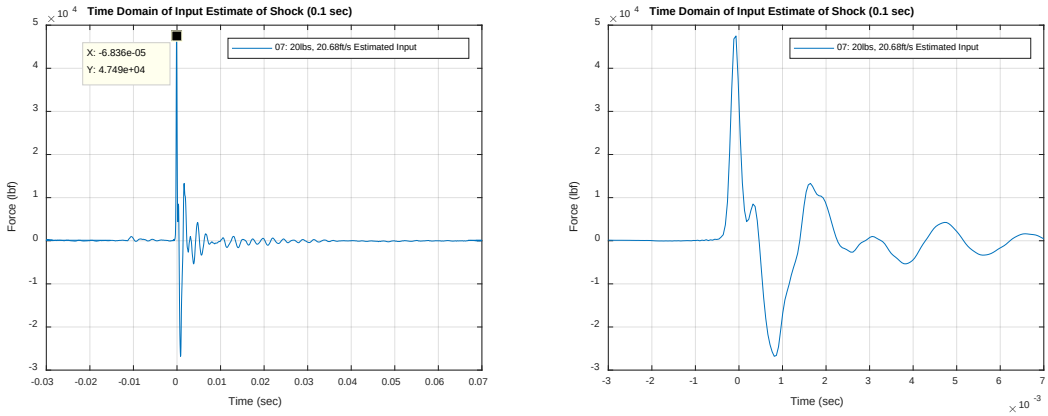

Figure 87. IFFT of Estimated Shock Input Spectrum 20 lbs, 20 ft/s

The peak force in the time domain increased to 47,490 lbf. The system does not appear to be able to complete the impulse before the system responds because it is constrained. The process was repeated for test run 8 with a 20 lbs projectile at 20 ft/sec in Figure 88.

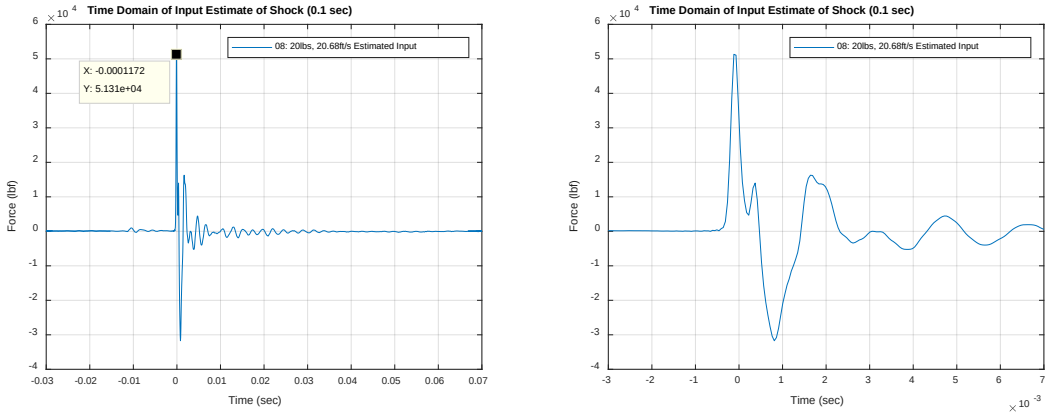

Figure 88. IFFT of Estimated Shock Input Spectrum 20 lbs, 20 ft/s

The peak force in the time domain increased to 51,310 lbf. The process was repeated for test run 14 with a 20 lbs projectile at 50 ft/sec in Figure 89.

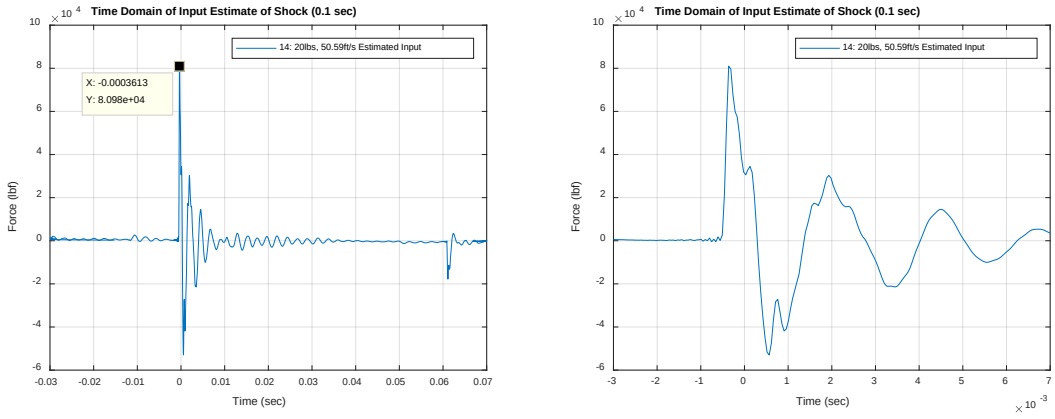

Figure 89. IFFT of Estimated Shock Input Spectrum 20 lbs, 50 ft/s

The peak force in the time domain increased to 80,980 lbf. The time duration of the main pulse is increasing. The proof in the time history of the double impact that created the ripple in the time domain is obvious after the initial impact decayed. The process was repeated for test run 15 with a 20 lbs projectile at 50 ft/sec in Figure 90.

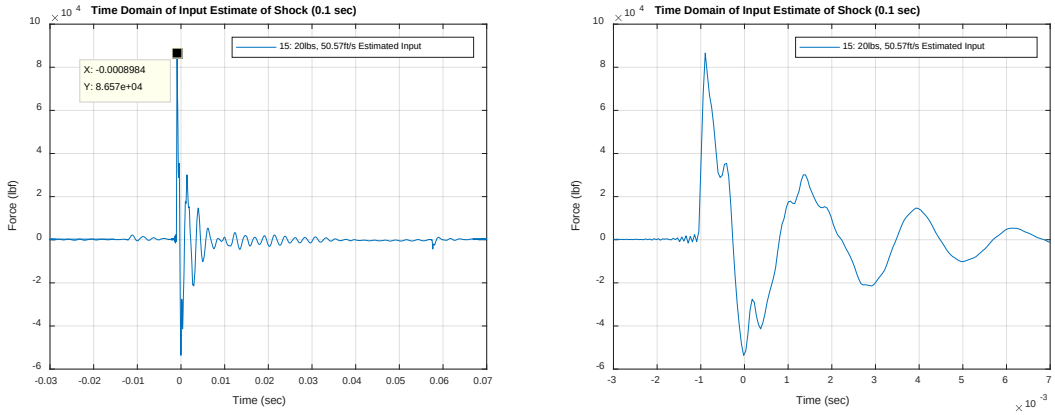

Figure 90. IFFT of Estimated Shock Input Spectrum 20 lbs, 50 ft/s

The peak force in the time domain increased to 86,570 lbf. Increasing the projectile mass or increasing the projectile velocity both result in an increase in the maximum time domain response of these estimated inputs. This is expected, further validating this method.

There is an obvious 400-1,000 lbf input to the system that appears at roughly 10 milliseconds before every impulse. This is likely due to the release of a brake system on the part.

Table 10 is a summary of the time domain results of the input estimation method. The peak in the time domain estimated input, impulse time duration, and dominant frequency of all

of the test runs are included. The impulse time duration is found from the duration of the pulse. The dominant frequency is the frequency of this impulse time duration.

Table 10. Summary of High Amplitude Testing Input Estimation Results

Test Run	Projectile Mass	Projectile Velocity	Felt	Plate	Peak In Time Domain Output	Peak In Time Domain Input	Impulse Time Duration	Dominant Frequency
	lbs	ft/sec	inches		g	lbf	ms	Hz
1	5	19.58	0.25	C2003	5524	33000	0.293	3413
2	5	19.58	0.25	C2003	7296	32440	0.293	3411
3	10	20.69	0.25	C2003	2398	36560	0.537	1862
4	10	20.11	0.25	C2003	2224	34250	0.586	1706
5	15	20.11	0.25	C2003	2656	44890	0.537	1862
6	15	20.68	0.25	C2003	3723	52610	0.488	2048
7	20	20.68	0.25	C2003	2785	47490	0.781	1280
8	20	20.68	0.25	C2003	3275	51310	0.806	1241
9	5	50.58	0.25	C2003	20270	158800	0.391	2560
10	10	50.58	0.25	C2003	11260	96430	0.440	2275
11	10	50.57	0.25	C2003	10930	93220	0.439	2276
12	15	50.57	0.25	C2003	9910	83550	0.635	1575
13	15	50.57	0.25	C2003	8752	95800	0.635	1575
14	20	50.59	0.25	C2003	7249	80980	0.709	1411
15	20	50.57	0.25	C2003	9992	86570	0.684	1462
16	5	19.58	none	C2003	8567	34830	0.293	3408
17	5	20.11	none	C2003	8077	36360	0.293	3408
18	5	19.58	none	C2003	8715	32820	0.293	3416
19	5	19.58	none	C2003	9051	33790	0.293	3413

The estimated input time domain peak followed the same trends that each output test run does, further validating this method. The estimated impulse time duration matches what is expected for altering the projectile mass. Increasing the projectile mass resulted in an increase in the impulse duration. A critical take away is that this dominant input frequency is also clearly seen in the SRS as the knee frequency of the response in Figure 91.

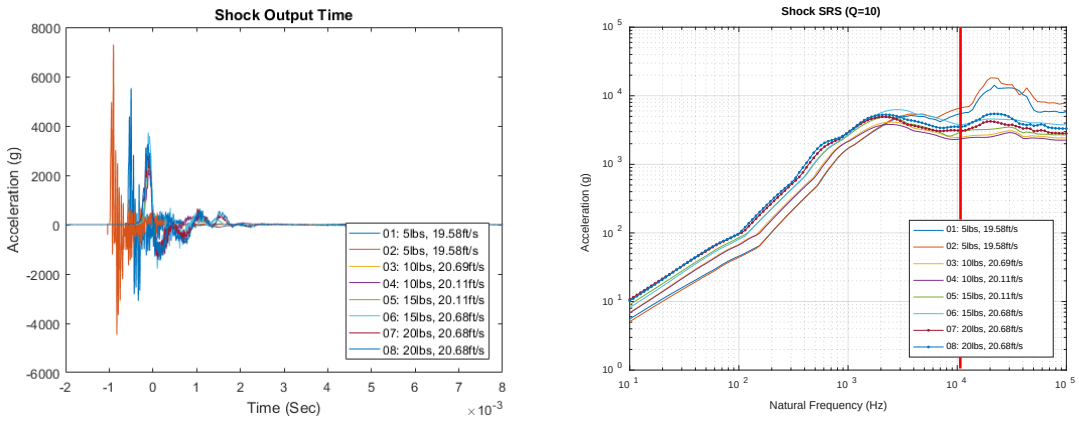

Figure 91. Time (Left) and SRS (Right) of Constant 20 ft/s Velocity, Variable 5, 10, 15, and 20 lbs Projectile

This is the same structure, but the knee frequency appears to follow the dominant input frequency rather than the frequency of the structure.

3.5 Modal Analysis

3.5.1 Damped Plate Full Modal Analysis

To validate the FEA model and understand the modes that participate in the response of the entire system, an experimental modal analysis was performed. A single input sine chirp shaker test was conducted with roving accelerometers. Because the sine chirp was input for only 75% of the acquisition time, the energy in the system had enough time to dissipate and the response was able to drop to the level of the noise floor. This implies that leakage should be minimized as the response should be a totally observed transient.

The accelerometers were 4.5 grams each. This was a total of 0.11 lbs. From an FEA model, the system was found to be 33.3 lbs. This means the total of the accelerometers was 0.33% of the system's weight. Initially, this is considered to rule out mass loading.

Care was taken to ensure there were no unmeasured inputs to the system. It was in a free-free environment. The shaker was rigidly mounted and the stinger uncoupled it from the system under measurement.

It can be assumed that the system is extremely nonlinear. The eigenvalue solution using real and complex residuals result in the same frequencies, but drastically different results. Although this is likely more modes than are present in the system, this emphasizes the point that doing a modal assurance criteria (MAC) of themselves (autoMAC) reveals the following Figure 92.

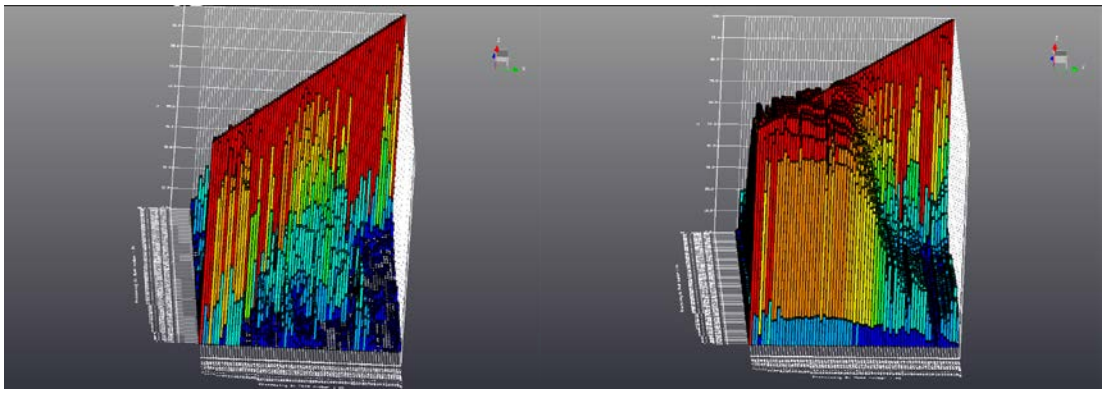

Figure 92. MAC of Real Residuals (Left) and Complex Residuals (Right)

These should be identical, but are not. This is either due to the nonlinearities of the system or an inconsistent data set.

A multi-run modal analysis was conducted in LMS TestLab. For each run, the poles that were found were extremely stable, however between each test run these poles were not consistent. This revealed that the modes themselves shifted in frequency between each run by a substantial amount and some were not consistent from run to run. An example of this is seen in the following Table 11, where the first row were the frequencies curve fit using all of the available data and each of the following rows were the frequencies of each respective mode found from curve fitting each data run.

Table 11. Multirun Modal Analysis of Each Test Run

Target 1 769.543 Hz	Target 2 775.983 Hz	Target 3 996.152 Hz	Target 4 1034.564 Hz	Target 5 1064.126 Hz	Target 6 1120.572 Hz	Target 7 1205.840 Hz	Target 8 1228.596 Hz	Target 9 1263.055 Hz	Target 10 1319.782 Hz	Target 11 1418.586 Hz
	776.341	1026.860	1029.818	1063.685	1108.197		1243.537	1260.837	1324.758	1439.101
	773.354	1000.667		1065.159	1105.219			1259.061	1333.117	1443.834
771.337		1013.697		1053.105	1101.587		1248.506	1249.296	1329.791	1439.094
764.700		952.410		1055.548	1097.151		1226.938	1249.638	1329.391	1443.028
769.504		1018.625	1047.987		1101.475	1216.140		1251.246	1327.749	1441.877
766.672		985.737	1029.867		1092.380		1236.399	1242.863	1314.576	1431.307
771.161			1024.698		1094.275		1233.212	1266.128	1317.560	1426.274
	772.863		1024.367		1093.401		1234.145	1272.547	1317.228	1421.668
	774.762	1007.210	1026.448		1107.207		1236.246	1258.962	1308.527	1430.585
	776.327	985.161	1048.568		1112.191		1246.604	1265.391	1318.344	1436.416
	774.924	992.997	1028.035	1066.865			1249.384	1274.726		1416.878
	772.918	967.185	1027.780		1100.235		1223.832	1283.377	1302.510	1426.379
	773.803		1023.642	1083.670	1156.414		1224.966	1271.016	1301.291	1422.205
767.751		1016.266	1023.917	1063.426	1147.195		1223.098	1261.019	1336.666	1421.601
768.793	773.164		1017.637	1058.692			1227.259	1264.618		1427.911
	784.081	1007.092	1041.004	1057.648			1239.720	1283.816		
	783.724	996.797	1026.324	1055.319			1232.700	1276.885		
768.632		1013.813	1035.991	1058.883		1207.270	1239.174	1262.095		1423.281

This inconsistency proves that the data acquired is not reliable and should be acquired in a way that nonlinearities can be better analyzed. A stepped sine and using multiple inputs to excite more of the modes of the system would make this data much more useful. Investigations in mass loading should also be completed.

3.5.2 Single Plate Modal Analysis

To eliminate the inconsistency from run to run, a modal using only a single test run was completed of three different plate configurations using the newly manufactured single plate. This single plate should minimize the nonlinearities.

These accelerometers were only 1 gram each. This was significantly lighter than the previous test and should entirely eliminate any concern of mass loading.

A full comparison of the natural frequencies of the first nine modes can be seen in Table 12. These are all of the modes found up to 4,000 Hz. The model appears to be too stiff but the trends between each test run are consistent between simulation and experimental. The membrane mode (no nodal diameters) is highlighted in the table.

Table 12. Natural Frequencies (Hz) of Modes from Three Test Configurations

Natural Frequencies (Hz) of Modes											
			Test 1- Only Plate			Test 2- Plate and Fixture			Test 3- Plate, Fixture, Impact Pad		
Mode #	Nodal Diameters	Nodal Circles	Simulation	Experimental	Error (%)	Simulation	Experimental	Error (%)	Simulation	Experimental	Error (%)
1	2	0	789	750.2	5.17	990	883.4	12.07	1001	886.8	12.88
2	2	0	790	753.1	4.90	1075	969.5	10.88	1082	973.6	11.14
3	0	1	1346	1348.1	-0.16	1361	1270.0	7.17	1345	1249.4	7.65
4	3	0	1793	1721.9	4.13	1855	1752.4	5.86	1860	1750.5	6.26
5	3	0	1793	1738.4	3.14	1855	1765.1	5.10	1860	1765.2	5.37
				2638.5							
6	1	1	2938	2913.0	0.86	2260	2063.2	9.54	2213	2017.0	9.71
7	1	1	2938	2921.6	0.56	2260	2128.9	6.16	2213	2080.7	6.36
8	4	0	3065	2966.1	3.33	3090	2972.5	3.95	3095	2972.1	4.13
9	4	0	3066	2969.7	3.24	3090	2973.2	3.93	3095	2975.0	4.04
				3041.2							

An autoMAC of the modes from test 3 is in Figure 93. Modes 1 and 2 appear correlated to modes 8 and 9, but this is due to spatial aliasing. More response locations would resolve this issue.

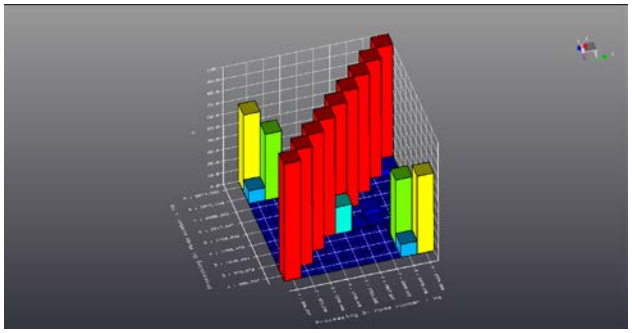

Figure 93. AutoMAC of Test 3

The FEA result of mode 1 is on the left and the experimental result of modes 1 and 2 of the system are seen in Figure 94. These are the first set of repeated roots (bending modes) of the system.

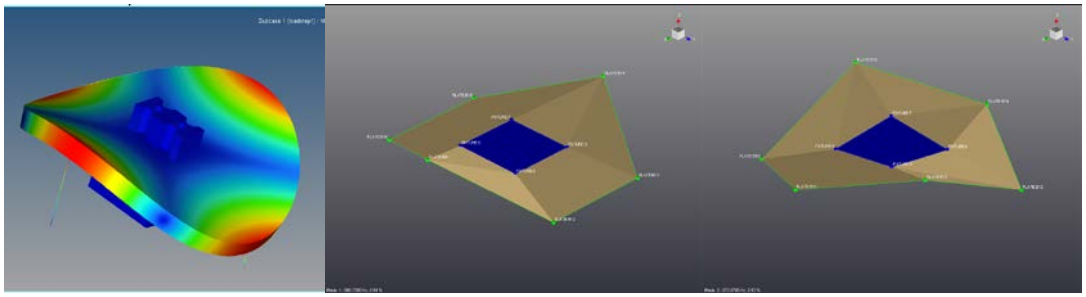

Figure 94. FEA of Mode 1 (Left) and Experimental of Modes 1 and 2 of Test 3 (First Set of Repeated Roots)

The FEA result of mode 3 is on the left and the experimental result of mode 3 of the system is included in Figure 95. This is the membrane mode of the plate, which is the mode that primarily contributes at the center.

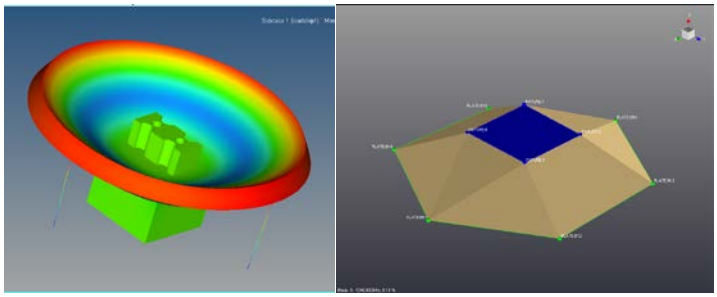

Figure 95. FEA of Mode 3 (Left) and Experimental of Mode 3 of Test 3 (Membrane Mode)

The FEA result of mode 4 is on the left and the experimental result of modes 4 and 5 of the structure are in Figure 96. These are the second set of repeated roots (bending modes) of the system.

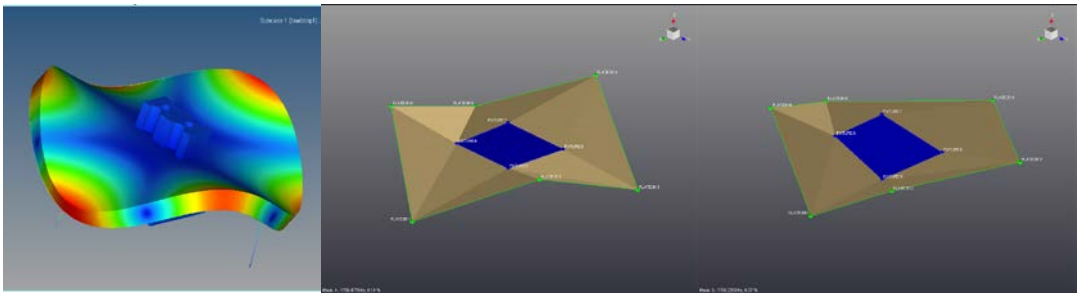

Figure 96. FEA of Mode 4 (Left) and Experimental of Modes 4 and 5 of Test 3 (Second Set of Repeated Roots)

The FEA result of mode 6 is on the left and the experimental result of modes 6 and 7 are in Figure 97. These are the third set of repeated roots (torsional modes) of the system.

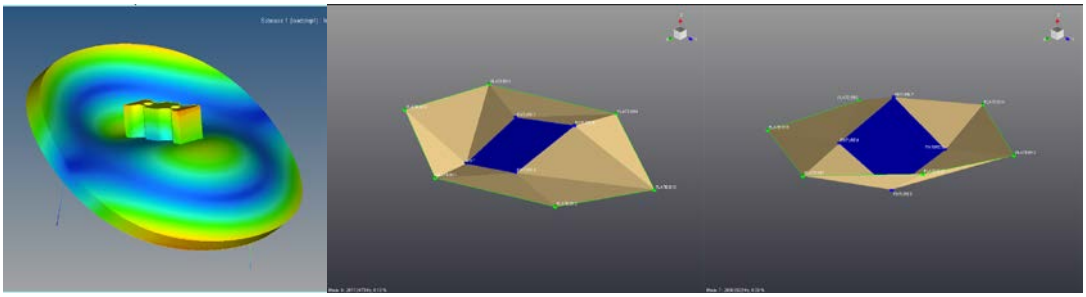

Figure 97. FEA of Mode 6 (Left) and Experimental of Modes 6 and 7 of Test 3 (Third Set of Repeated Roots)

The FEA result of mode 8 is on the left and the experimental result of modes 8 and 9 are in Figure 98. These are the fourth set of repeated roots (bending modes) of the system.

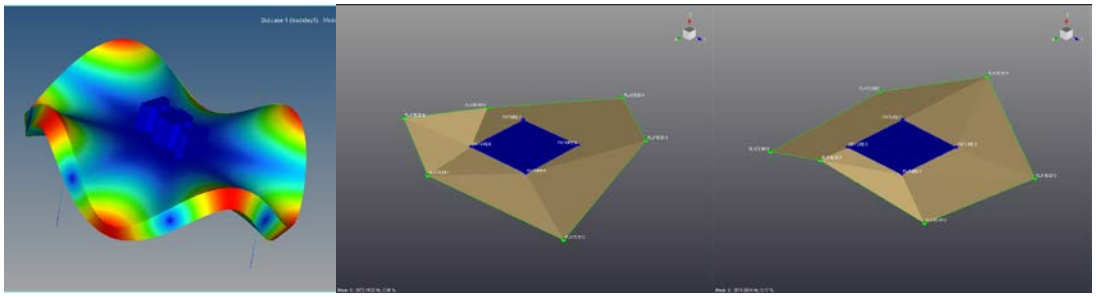

Figure 98. FEA of Mode 8 (Left) and Experimental of Modes 8 and 9 of Test 3 (Fourth Set of Repeated Roots)

Modes 8 and 9 don't visually appear as in the simulation because there aren't enough response locations. This creates spatial aliasing in the mode shape, which is also why there is some correlation in the autoMAC in Figure 93. This could easily be resolved by including more accelerometers at different angles. This consistent dataset can be used for modal decomposition in the future.

The comparison provides confidence in the FEA model and this analysis currently highlights the importance of excitation and response location.

4 Recommendations and Conclusions

To minimize the number of contributing modes in a shock response spectrum (SRS), a finite element model of a circular plate was developed and validated. Two modes were found to contribute to the SRS, but only the lower one was desired. The cross sectional thickness was evaluated for a flat, convex, and concave shape to investigate moving the higher mode out of the frequency band of interest. The convex design separated the bending mode natural frequencies of the system by a greater margin than the concave design, which moved them closer together in frequency. The SRS displays the same trends in frequencies as the FRF. This convex design consideration could be used with more extreme geometry to move the second frequency out of the frequency band of interest.

An analytical solution proved that there is a specific ideal damping of the plate that should be designed and boundary conditions can become critical in meeting specifications. A free-free boundary condition should be used to meet this desired response. Input impulse duration can be directly seen in the SRS in a constrained system.

Two different sets of resonant plates with varying damping mechanisms were experimentally tested to compare types of shock inputs and input force levels. Low amplitude testing indicated high repeatability and increasing force levels produced an increase in the SRS amplitude. The plate with the damping material consistently produced a SRS with a more rounded knee frequency. The amount of bolt torque of the 8 bolts clamping the set of three plates together affected the plate without damping material much more significantly than the plate with the damping material.

A softer hammer tip can provide a SRS without exciting the knee frequency due to input energy rolloff. The knee frequency will appear at the frequency that the input energy rolls off.

A striker plate was included in the system but the asymmetrical geometry appeared to have minimal effect on the resulting SRS. Adding a small amount of mass at the center of the plate to protect the testing plate structure does not appear to dramatically impact the results from an impact at the center and response at the center.

Two boundary conditions were tested at low amplitude. Nonlinearities are apparent for some FRFs, but the SRS of each system appeared mostly consistent. The SRS is sensitive to off axis response and off axis input. There appears to be no significant relative motion between the plate and fixture.

High amplitude shocks were tested and variables of this testing included projectile mass, velocity of the projectile, and programmer at the impact location. Trends were monitored in the SRS. The higher velocity of the projectile consistently had more energy, typically at high frequency. The higher projectile mass had a higher initial amplitude difference obviously dependent on the kinetic energy applied to the system. But as the mass increases, the SRS appeared to roll off at a lower frequency, confirmed by both plate sets. The felt

programmer was too soft to have any impact within the frequency range of interest likely due to the relative mass and velocity of the projectile, but it did effect the SRS above the frequency of interest. Using felt does not appear to assist in meeting specifications below 10,000 Hz.

The positive and negative and primary and residual responses of the SRS indicated valuable shock data. The low frequency velocity shift correction in the SRS proves to be a simple correction that does not require a complex algorithm.

A resonant plate shock test typically has high enough input amplitude that a conventional force sensor would not withstand the test to give a reliable measurement of the input. Using a low amplitude frequency response function and a high amplitude shock output, the high amplitude input can be estimated. This was tested at low amplitudes where the input spectrum was known and can be directly compared. This validation was performed for three different systems and each revealed reasonable recreation of the input force. The IFFT of the estimated input was performed and matches the initial time domain input. The shock input spectrums were estimated for high amplitude hits. Experiments of altering the projectile mass, velocity of the projectile, and programmer at the impact location were conducted. Expected trends were monitored. The higher velocity of the projectile consistently had more energy. The higher projectile mass consistently had more energy for the low testing velocity, but not for the high testing velocity. The felt programmer was too soft to have any impact likely due to the relative mass and velocity of the projectile. The IFFT of this estimated shock input is the expected magnitude. A modal analysis of the damped plate was largely unsuccessful in providing quality data due to nonlinearities or an inconsistent data set. A modal analysis of a single undamped plate set provided a consistent data set and the modes up to 4,000 Hz.

It is recommended that modeling efforts continue to better understand the implications of adding damping material within the plates. Creating a nonlinear model with bolts and a viscoelastic layer to model the damping material would exponentially further the accuracy of the modeling efforts. This linear model was only fit for a proof of concept. Modelling more extreme convex geometries to further separate the modes could discover a geometry that would produce any desired SRS curves. A two degree of freedom analytical model would better replicate the structure that is currently fabricated. Using an Hv estimator of FRF to limit the noise on the input as well as the output when estimating the input spectrum could help eliminate noise on the estimated input spectrums. For modal testing, a stepped sine might accurately characterize the nonlinearities of the system. A multiple input test that utilizes two shakers would help to excite all of the modes. Because the system is symmetrical, this is difficult to accomplish with just one input. Smaller accelerometers may help to limit the potential for mass loading for the damped plate testing.

This project will next look at the triaxial SRS. There is clearly energy along the other axis that a uniaxial accelerometer does not measure, meaning the part is being over tested. The ultimate question is the degree that it is being over tested. Although the SRS appears to be a good initial look at shock severity and has served its purpose well, it would benefit to

develop a new method. This has been attempted and is being considered by bright minds, but can use more focus. [17] [18] It is not responsive to changes in the structure and its peak hold nature likely over tests components. Finding the exact root cause of failure may be more beneficial. Redefining the specifications to use stress and strain as a metric could give a more accurate perspective on the energy present in the system and more specific cause of failure.

5 Future Work

The FEA model should be correlated with the experimental results and expanded to a nonlinear model, resulting in future FEA simulations that hold more merit. A consistent modal data set of the damped plate set would provide a means to correlate the highly damped plate set to an FEA model. Investigating more extreme geometry tests of a convex plate, damping changes, and different impulse input types through simulations would reveal better results and all should be done if the SRS is continued to be utilized.

Modal decomposition from experimental modal data would reveal precisely how each of these modes participate in the SRS response. A more thorough experimental or modelling investigation of how the response changes across the face of the fixture would likely further prove the flaw in monitoring the SRS at one location on the fixture. The part under test undoubtedly experiences more inconsistent excitation than shown here.

Triaxial SRS data should be acquired and analyzed. The SRS of these off axis responses will reveal the validity and quality of the current testing method. This will likely result in further emphasis of the need for overall reconsideration of the SRS as a testing metric.

The focus should be shifted to consider stress and strain measurements as specifications for testing failure in parts. Measuring the acceleration in a typical shock test (even on three axes) while also taking strain measurements would give a reference to compare to quantify the extent the part is being over tested.

6 Reference List

[1] W. Larsen, J. R. Blough, J. DeClerck, C. Van Karsen, D. Soine and R. Jones, "Comparison of Input Levels on the Shapes of SRS Functions," in *Shock and Vibration Symposium*, Jacksonville, 2017. (Presentation Only)

[2] W. Larsen, J. R. Blough, J. DeClerck, C. Van Karsen, D. Soine and R. Jones, "Inverse Force Estimation for Resonant Shock Plate Application," in *International Modal Analysis Conference*, Orlando, 2018.

[3] W. Larsen, J. R. Blough, J. DeClerck, C. Van Karsen, D. Soine and R. Jones, "Effects of Variable Thickness Circular Plates on Frequency Response Functions and Shock Response Spectrum," in *International Modal Analysis Conference*, Orlando, 2018.

[4] T. Irvine, "An Introduction to the Shock Response Spectrum," 2012.

[5] N. Davie, "The Controlled Response of Resonating Fixtures Used to Simulate Pyroshock Enviornments," in *Shock and Vibration Bulletin*, Washington D. C., 1986.

[6] J. Blough, J. DeClerck and V. K. Charles, "Tunable Resonant Plate Testing," Michigan Technological University, Houghton, 2016.

[7] C. Harris, Harris' Shock and Vibration Handbook, New York: McGraww-Hill, 2010.

[8] R. D. Blevins, Formulas for Dynamics, Acoustics and Vibration, John Wiley & Sons, 2016.

[9] K. Itao and S. H. Crandall, "Natural Modes and Natural Frequencies of Uniform Circular Free-Edge Plates," *Journal of Applied Mechanics*, vol. 48, pp. 447-453, 1979.

[10] J. Ahles, J. Ballor, B. Kinder, S. Viehl, J. Vincent and A. White, "Capstone Design Final Report," Michigan Technological University, Hougthon, 2016.

[11] J. Blough, J. DeClerck, C. Van Karsen and D. Soine, "Method to Predict the Shock Response Spectrum from Frequency Response Funtions," in *IMAC proceedings*, 2017.

[12] J. Tuma and P. Koci, "Calculation of the Shock Response Spectrum," in *Colloquium Dynamics of Machines*, Prague, 2009.

[13] J. Alexander, "Shock Response Spectrum - A Primer," *Sound and Vibration*, 2009.

[14] T. Edwards, "The Effects of Boundary Conditions in Component-Level Shock and Vibration Testing," in *Sandia National Laboratories*, Albuquerque.

[15] D. Smallwood, "The Shock Response Spectrum at Low Frequencies," in *Sandia National Laboratories*, Albuquerque.

[16] J. Blough, W. Larsen, J. DeClerck, D. Soine and R. Jones, "Velocity and Other Low Frequency SRS Shape," in *Shock and Vibration Exchange*, Jacksonville, 2017.

[17] J. Cap and D. Smallwood, "A Methodology for Defining Shock Tests Based on Spock Response Spectra and Temporal Moments," Sandia National Laboratories, Albuquerque, NM, 1997.

[18] D. Smallwood, "An Improved Recursive Formula for Calculating Shock Response Spectra," in *Sandia National Laboratories*, Albuquerque.

[19] Morse and R, "Comparison of Response from Different Resonant Plate Simulation Techniques," in *The Shock and Vibration Bulletin*, Washington D. C., 1986.